BEAM PROFILE AND POINTING WORKING GROUP FINAL REPORT

A. Salama[1], D. A. Beintema[2], C. Lloyd[3], R. Lorente[1], K. Okumura[4], A. Pollock[1], B. Schulz[5]

with contributions from:

P. Abraham, H. Feuchtgruber, L. Haser, A.M. Heras, U. Herbstmeier, U. Klaas, F. Lahuis, R. Laureijs, D. Lemke, P. Morris, T. M uller, S. Peschke F. Sibille, E. Valentijn, B. Vandenbussche

SAI/2001-027/Dc, Version 1.0

3 September 2001

[1] ISO Data Centre, Astrophysics Division, Space Science Department of ESA, Villafranca, P.O. Box 50727, E-28080 Madrid, Spain
[4] Institut d'Astrophysique Spatiale, Universite d'Orsay, F-91405 Orsay, France
[2] SRON, P.O. Box 800, NL-9700 AV Groningen, The Netherlands
[3] Rutherford Appleton Laboratory, Chilton, Didcot, Oxon OX11 0QX, UK

Document Information

Document:	Beam Profile and Pointing WG Final Report
Title:	Beam Profile and Pointing WG Final Report
Reference Number:	SAI/2001-027/Dc
Issue:	Version 1.0
Issue Date:	3 September 2001
Authors:	A. Salama, D. A. Beintema, C. Lloyd, R. Lorente, K. Okumura, A. Pollock, B. Schulz

Document Change Record

Date	Revision	Comments
1 August 2001	Version 0.9	First version
3 September 2001	Version 1.0	Completed SWS chapter

Contents

Chapter 1

Introduction

The Beam Profile and Pointing Working Group is one of the eight Calibration Working Groups constituted at the ISO Data Centre to address different calibration topics during the Post-Operational Phase of the ISO Project in the framework of the global ISO (Cross-)Calibration strategy.

The Working Group scheme was ideated as a platform to exchange knowledge and progress between the members of each of these Working Groups, across instrument boundaries and major themes of common interest.

1.1 Purpose of the Beam Profile and Pointing WG

The purpose of the Beam Profile and Pointing WG, as also stated in the ISO (Cross-)Calibration Plan for Post-Operations, is to:

- Characterize the instruments beam profiles
- Address common problems (asymmetries, vignetting, ghosts) and their possible relation with the telescope PSF
- Allow cross-fertilisation of software across the instrument teams
- Support improvements of the ISO pointing.

1.2 Beam Profile and Pointing WG Webpage

The Beam Profile and Pointing WG WWW page is maintained by A. Salama at

`http://isowww.vilspa.esa.es:1909/~asalama`

This page contains information on all meetings held by the Working Group, including in most cases the viewgraphs there presented, as well as a bibliographic database of documents (from internal reports just for internal circulation to papers) related with this calibration topic.

1.3 Beam Profile and Pointing WG composition

The Beam Profile and Pointing WG members were:

Alberto Salama	Chair, SWS Beams, ISO Pointing
Douwe Beintema	SWS Beams
Rosario Lorente	SWS Beams (until December 1999)
Chris Lloyd	LWS Beams
Koryo Okumura	ISO PSF, CAM beams
Bernhard Schulz	PHT Beams
Andy Pollock	ISO Pointing in OLP

Contributions to Beam Profiles and Pointing issues were made in the course of the years by many other persons, as acknowledged in the report cover.

1.4 Executive summary

TBW:

Executive summary (2-pages) of

the WHY (what are the beams profiles for, the main problems to deal with) the HOW (measurements, models, Working groups) the WHAT (is available now: in OLP, in IAs, as CAL-G's and algorithms/tools) the way information is presented in the Final Report

Chapter 2

ISO telescope Point Spread Function

2.1 Introduction

During the commissioning phase of the ISO mission, the ISOCAM point spread function (PSF) was measured in order to validate the performance of the ISO telescope optics. Since its quality affects any data of the instruments on-board ISO, it is obvious that this measurement was of prime importance. The ISO telescope is a 60 cm diameter Ritchy-Chrétien system with an overall focal ratio of f/15 (ISO observer's manual [13]). The main aperture is imposed by the diameter of the secondary mirror and the size of the central obscuration is imposed by that of the secondary mirror baffle. The secondary mirror is supported by a tripod of 20 mm width. Each instrument sees a 8.5' off-axis field corresponding to one surface of the pyramidal mirror located near the focal plane of the telescope (Fig. 2.1).

2.2 Measurements

No ground-based ISOCAM measurement has been performed through the real telescope before the launch. Thus, only the in-orbit calibration data are available for the telescope performance check with the ISOCAM. The best way of measuring the ISO telescope PSF is to use the ISOCAM in one of its configurations which minimizes its instrumental effect. It is suitable to use calibration data obtained for the ISOCAM PSF measurements with a point source at the center of the detector array to avoid a possible field distortion effect of the ISOCAM (§ 3.7). Tab. 3.1 lists all the PSF calibration data made during the mission (see § 3). The most obvious instrumental effect of the ISOCAM arises from the limited pixel size of the detector arrays, which implies a limited sampling rate of the PSF and also a limited resolution of the pixel. In order to obtain a better sampling rate with respect to the pixel size, the PSF observations were made in micro-scanning mode on a bright point source with the minimum allowed raster step size of 2 arcsec (Okumura [19]). However, the micro scan can not improve the resolution of the pixel, which can be minimized only by choosing a large PSF compared to the pixel size. The best configuration is that of 1.5 arcsec pixel field-of-view (pfov) with the LW9 filter at 15 μm. The LW9 filter has the longest reference wavelength of the ISOCAM and its band width is smaller than that of LW3. Thus, this filter gives the largest and less blurred PSF.

2.3 Data reduction

The data have been reduced in the CAM Interactive Analysis (CIA, see CIA user's manual 2000 [12]) using a reduction procedure which includes the following.

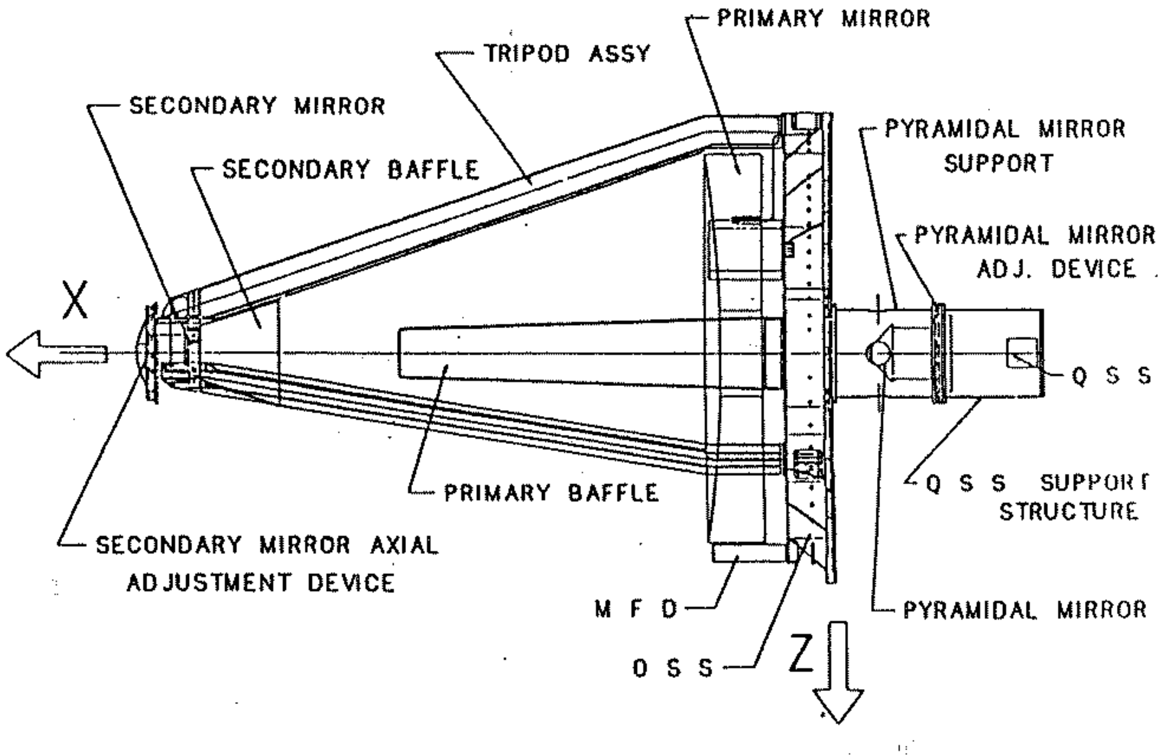

Figure 2.1: ISO telescope optical scheme

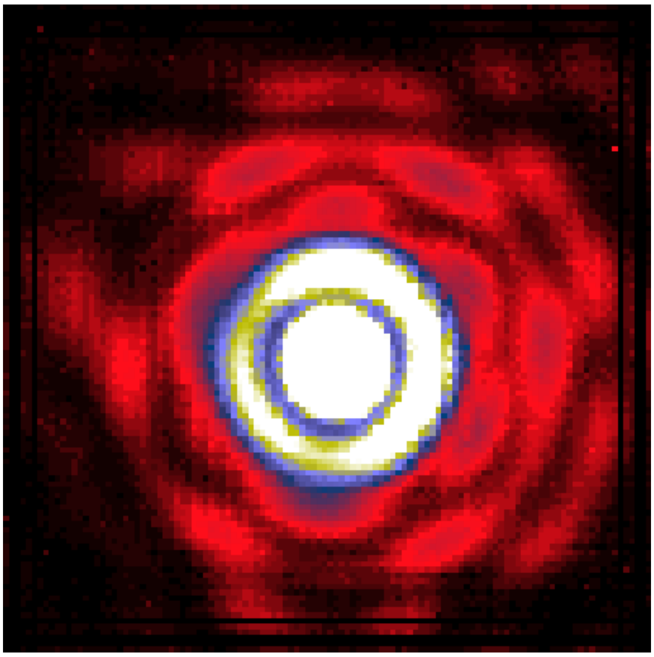

Figure 2.2: ISOCAM PSF in the configuration of the minimum instrumental effect

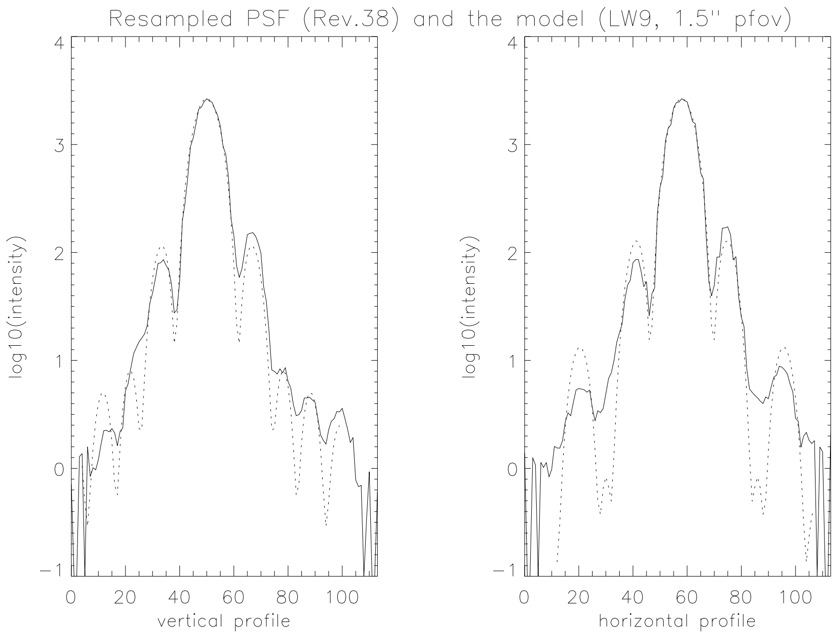

Figure 2.3: ISOCAM PSF in the configuration of the minimum instrumental effect

- deglitch, method='temp'
- stabilize, method='ksig'
- average, /second
- corr_dark, method='calg'
- corr_flat, method='calg'

The temporal deglitching was adopted because of its relatively negligible point source flux loss. No transient correction has been applied, since the existing correction algorithm are all known not to be adapted to point sources. No flat field has been generated using the redundancy from within the raster cube for the sake of a coherent reduction procedure in all the configurations, for it is impossible to obtain a reasonable flat field at short wavelengths due to the faint surface brightness of the zodiacal light.

2.4 Final products

Fig. 2.2 shows the PSF with LW9 filter through 1.5 arcsec lens reconstructed in the sampling rate of 0.5 arcsec which is determined by the pixel size and the microscan step size. The diffraction pattern of the tripod is seen which results in a set of concentric hexagonal pattern instead of circular airy rings. This feature introduces a slight difference between Y-axis (horizontal in Fig. 2.2) and Z-axis (vertical) PSF profiles (see Fig. 2.3). The final product of the PSFs of LW9 filter through 1.5 arcsec pfov lens can be found in the LWPSF Cal-G file, as a part of the ISOCAM PSF library.

Table 2.1: Some optical parameters of the ISO telescope

Object	Value
Primary mirror (M1)	
Total diameter	640 mm
Optically used outer diameter	634 mm
Diameter of central hole	145 mm
Optically not used inner diameter	150 mm
Radius of curvature	2000 mm
Conic constant	-1.00422
Secondary mirror (M2)	
Optically used outer diameter	87.6 mm
Diameter of central hole	15 mm
Optically not used inner diameter	25 mm
Radius of curvature	-328.5 mm
Conic constant	-1.60366658
Telescope	
Focal length	9000 ± 250 mm
Numerical aperture	f/15
Axial mirror separation	854 ± 1.8 mm
Entrance pupil	600 mm at 5849.3 mm behind M1
Exit pupil	87.6 mm at M2
Secondary baffle maximum diameter	173.9 mm at 742.4 mm before M1
Tripod width	20 mm
Linear obscuration (central + tripod)	0.36
Instrument field of view	8.5 arcmin off axis
Unvignetted field of view	3 arcmin diameter
Pyramidal mirror tilt	44.515 °

2.5 PSF model

The measured PSF is compared with two independent models (Okumura 2000 [17]). One of them is based on the Fourier transform of the telescope aperture. The second is based on the ray tracing with gaussian decomposition of the beam to simulate the diffraction.

Model through the Fourier transform

The point spread function (PSF hereafter) of the ISO telescope can be computed using some of its optical parameters listed in Tab. 2.1 (1989 [14]). The optically used diameter of the primary mirror is 634 mm, but the entrance pupil is defined by the secondary mirror which imposes the effective aperture of 600 mm. The central obscuration is imposed by the largest element centered on the optical axis, which is the largest part of the secondary baffle diameter. The tripod is mounted at 0°, 120°, 240° from the negative side of Z axis [1].

The computation of the PSF is based on the Fourier transform of the ISO telescope aperture.

$$\mathrm{PSF}_\lambda = ||\mathrm{FFT}[\mathrm{Aperture}\ (\lambda)]||^2 \tag{2.1}$$

[1]The spacecraft's X axis points toward the sky from the telescope and its Z axis toward the ISO's solar panel

This gives a monochromatic PSF of the ISO telescope at a wavelength λ.

Then for a possible instrumental configuration of a wide wavelength range, one can compute an "equivalent" telescope PSF which would be "seen" by the instrument before any modification of the beam inside this instrument. For a given wavelength range and a given spectrum of the point source, this "equivalent" PSF is computed by integrating over the wavelength range the product of PSF_λ, the spectral response profile of the instrument $R(\lambda)$ and the point source spectrum $S(\lambda)$.

$$\mathrm{PSF} = \int_{\lambda_{inf}}^{\lambda_{sup}} R(\lambda) S(\lambda) \mathrm{PSF}_\lambda \, d\lambda$$

The sum of the electro-magnetic field powers of different frequencies is same as the power of the sum of the electro-magnetic fields because of the orthogonality of the wavelength as a base of the function space. This is why one can sum PSF_λ over the wavelength range. However, this part of the modeling should be adapted for each case of each instrumental and sub-instrumental configuration. The modeling depends then largely on the instrumental effects on the beam. The monochromatic ISO telescope PSF can be used as input into an instrumental beam profile model. Therefore, in the following, we will focus only on the monochromatic PSF.

In principle, the mathematical solution is as simple as the equation (2.1). However, in the computation using a computer, one has to transform this formula into a discrete computation. This leads us to consider the size of the aperture with respect to that of the image array and also the sampling rate and the size of the image array.

Aperture size within an array

In the monochromatic PSF computation, the pupil image is created in the Fourier space. The sampling rate (we will call it pixel size hereafter) P_{Fourier} in this space is given by:

$$P_{\mathrm{Fourier}} = \frac{\lambda}{I P_{\mathrm{rad}}}$$

where λ is a considered wavelength , I is the size of the image array expressed in number of pixels (the image is supposed to be square) and P_{rad} is the pixel size in radian of the PSF image in the direct space. The diameter Δ of the circular aperture in the Fourier space in pixel units is then given by dividing the telescope diameter D by the pixel size P_{Fourier}:

$$\Delta = \frac{D}{P_{\mathrm{Fourier}}} = \frac{D}{\lambda} I P_{\mathrm{rad}}$$

If λ is expressed in μm, its radius r is given by:

$$r = \frac{\Delta}{2} = \frac{0.6 \cdot 10^6}{2 P_{\mathrm{Fourier}}} = \frac{0.3 \cdot 10^6 I P_{\mathrm{rad}}}{\lambda}$$

One can see that for a given wavelength λ and a given sampling rate P_{rad} of the PSF, the ratio r/I remains constant ρ.

$$\rho = \frac{r}{I} = \frac{0.3 \cdot 10^6 \; P_{\mathrm{rad}}}{\lambda} \tag{2.2}$$

This means that, to create a PSF, there is an infinite choice of the value of r as long as the array size is chosen accordingly. The bigger is the array size, the further from the brightest pixel is computed in the PSF. The simplest idea is to choose the array size just like that of the PSF

Table 2.2: Offset coordinates (in arcmin) of the instrument apertures

Instrument	Y coordinates	Z coordinates
QSS ref.	0.000000	0.000000
CAM	8.544170	0.124167
LWS	0.225000	-8.425000
PHOT1	-0.158333	8.435000
PHOT2	-0.158333	8.435000
PHOT3	-0.113333	8.415000
SWS1	-8.475000	1.173330
SWS2	-8.421670	-0.370000
SWS3	-8.345000	-1.908330

image one wants to obtain. This may result good enough in some cases, but in general, the array size should be chosen according to the aperture radius.

First of all, the aperture should be large enough to be able to sample the smallest structure in the pupil. Secondly, the image size I should be at least 2 times larger than the aperture diameter D to sample correctly the PSF, but this limits the value of the ratio I/r to be larger than 4, which, in some cases, does not correspond to the required value of $P_{\rm rad}$ and λ. The choice of I requires further considerations about the sampling rate which is developed in the next section.

But once the image size is chosen, the central obscuration and the tripod structure can be added to the main aperture by respecting their size proportion.

Sampling rate and array dimension

In order to achieve a sufficient sampling rate, one has to provide at least 2 sampling points for the smallest length of the considered structure.

In the ISO telescope pupil, the smallest length is given by the tripod width as long as we ignore the effect of the off-axis field-of-view for each instrument aboard of the ISO telescope. If we take 2 sampling points for this structure, we need 60 pixels for the entire telescope aperture.

Now, if we want to include the offset of the central obscuration due to the effect of the off-axis field-of-view, the offsets of the obscuring elements relative to the main aperture can be computed considering the geometrical relations between these elements and the entrance pupil. The offset of the largest edge of the secondary baffle is computed to be 16.3 mm. The offset of the fictive summit of the tripod is approximately 3.6% larger whereas that of the tripod feet is 11.3% smaller. In order to sample correctly the pupil structure, it is preferable to take at least 2 sampling points in the 14.5 mm offset of the tripod feet which is the smallest offset of the obscuring elements. In this case, we need at least 83 pixels for the aperture diameter. The direction of the offsets depends on the aperture position of the considered ISO instrument. In Tab 2.2 are listed the pointing offsets of the instruments measured during the spacecraft commissioning phase. The opposite sign should be taken for the offsets of the obscuring elements. If we want to include also the small offset of Tab 2.2, the aperture diameter can easily exceed 4000 pixels. This may cause a memory capacity problem of the computer. However, this small offset can be considered to be negligible for what we can expect from a PSF model and it hence allows us to work with a reasonable array size.

In the PSF space, the PSF width must also lie over at least 2 pixels for a correct sampling. This is equivalent to say that the telescope aperture must be embedded in an array of at least 2 times

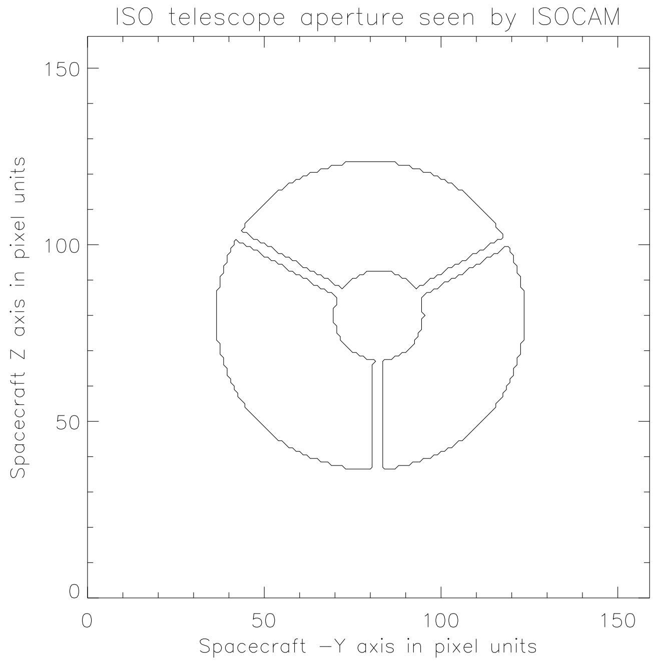

Figure 2.4: The diameter of the telescope aperture must be larger than 60 pixels to sample well the tripod structure

larger than this aperture, *i.e.* more than 120 pixels or 148 pixels if we include the off-axis effect (see Fig. 2.4).

If an instrument is undersampling in the real world, the ratio I/r is less than 4. But the instrument is not sampling with a Dirac's comb. It is sampling with a detector or a pixel which has a finite physical dimensions of the photo-sensitive volume. Therefore, one must compute a well sampled data by taking an image size of at least twice as big as the aperture diameter, and then compute an undersampled data by convolving with the instrumental detector or pixel response pattern. In this case, the size of the array is imposed to be a multiple of I given by the equation (2.2) and at least 2 time larger than D.

However, one may want to include the convolution effect of the finite physical size of the detector (or pixel) even for the case of $I/r > 4$. In this case, the array size should also be enlarged by the same multiplicative integer value than the sampling rate of the detector. If a very fine sampling is required, even by keeping the smallest value of $r = 30$, the array size can reach very quickly 2048×2048. This requirement can easily lead the computation out of the memory capacity of the computer, the practical solution being a compromise between the good sampling rate and the capacity of the computer we use.

The overall strategy of the PSF computation can be summarized as follows.

1) Compute the ratio $\rho = r/I$ for a given λ and a given sampling rate or pixel size P_{rad} according to the formula (2.2)
2) Set r large enough to well sample all the details of the pupil image
3) Set I to the nearest integer or nearest power of 2 larger than r/ρ
4) Reset r to ρI
5) If $I < 4r$, find a smallest integer n such that $nI > 4$ and reset I to nI
6) Add the other elements of the pupil structure respecting their size proportion
7) Fourier transform
8) Resample the PSF by the factor n taking into account the photo-sensitive response of the instrument
9) Consider an area of the PSF corresponding to the field-of-view of the instrument

The model based on the Fourier transform is available in CIA with a function called "calc_psf". A set of PSFs have been computed and stored in an IDL structure for all the configurations. The results are stored in a psf_*as.save file for each configuration and are distributed together with CIA.

Ray tracing model

The Fourier transform PSF model was well confirmed by another independent PSF model which is based on the ray tracing and on the Gaussian beam decomposition using BRO's ASAP ray tracing package. The telescope is modeled with a limited set of optical elements including the following elements.

- Primary mirror
- Secondary mirror
- Primary baffle
- Secondary baffle
- Tripod
- Pyramidal mirror

ASAP allows to compute the diffraction by means of the Gaussian beam decomposition, which gives a PSF well comparable to the Fourier model. Compared to the Fourier transform model, the ray tracing model provides an easy way to test optical anomalies due to the misalignment of some optical elements.

2.6 Deviations from the model

It is easily noticed that the data show an asymmetry in the diagonal direction. This is well seen in the brightness distribution of the first ring of the PSF. This asymmetry is observed at any wavelength and its amplitude is larger at short wavelengths (Okumura 1998 [19], 2001 [16]). The laboratory calibration data obtained in the telescope simulator before the satellite launch seem to show a small amount of detectable asymmetry over the noise, which suggests that at least a part of asymmetry may arise from the ISOCAM. However, any model parameters setting of the camera could reproduce the observed asymmetry. On the contrary, such a asymmetry can be reproduced with a slight offset of the secondary mirror of the telescope (M2). Nevertheless, it was found that no offset could reproduce the wavelength dependency of the amplitude of the asymmetry over the whole range of ISOCAM. This result however should be taken with some caution, because all the model parameter space may not been explored.

The other ISO instruments report also an asymmetry in their beam profiles, but it is not easy to identify the same asymmetry because of their other additional instrumental effects.

Another deviation found between the model and the data is the PSF width at short wavelengths (see § 3.3). However, SWS instrument does not observe such a large deviation, which suggests that it arises rather from within the ISOCAM.

2.7 Lessons learned

During the ISO mission the only available model of ISO PSF was an IDL procedure which computed the Fourier transform of the telescope aperture. This model provides reasonable results. However it is not very convenient for testing a possible optical anomaly. More than one ray tracing optical model of the ISO telescope had been developed before the launch, particularly to assess the stray light in the instruments. However these models were developed as a part of temporary contracts with outside company, making any follow-up of the models almost impossible.

The ray tracing model used here to simulate the M2 offset was developed from the scratch after the ISO in-flight operation. The obtained result does not allow us to understand all the observed deviations, but it is obvious that a ray tracing model is needed for the follow-up of the telescope performance.

It is certainly recommended to use a reliable optical model from the beginning of a space project and ensure its follow-up during the in-orbit operation up to the end of all the calibration tasks in the post-mission phase.

2.8 Conclusion

The two major deviations from the model are observed in the PSF measured by the ISOCAM : its asymmetry and its larger width at short wavelengths. The optical simulation by introducing a small M2 offset could not explain in a consistent way all the deviations observed as a function of wavelength. However some contribution of this effect is not ruled out in explaining the PSF asymmetry.

Chapter 3

CAM

3.1 Introduction

The optical design of the camera is based on an imaging lens which focuses on the detector the image of the sky provided by the ISO telescope (ISOCAM Observer's Manual 1994 [9]). The beam encounters a field mirror (Fabry mirror) at the focal plane of the telescope. This mirror has a spherical curvature and forms the telescope's exit pupil image on the plane where a set of filter plates is located. This allows the beam to pass across a limited area of filter regardless the incident angle of the beam into the telescope. After the filter, the diverging beam is converged by a convex lense on to the detector array.

Since the ISOCAM records the image on the focal plane just like any camera, the Point Spread Function (PSF) of the telescope is, in principle, modified little in the instrument. For this reason, the word "PSF" is used hereafter to indicate the beam profile of the ISOCAM. Note that the telescope PSF is nevertheless modified to some extent by some optical effects and especially by the pixel sampling effect.

The PSFs of different instrumental configurations were measured as a part of the calibration observations during in-orbit operation. These data were compared with the theoretical PSFs computed through Fourier transform of the telescope exit pupil image. The first order analysis has shown that the measured ISOCAM PSF is in a good agreement with the nominal PSF computed by this model. However further study revealed some systematic deviation from the model. Two major deviations are : (1) the systematic asymmetry mostly seen on the first Airy ring and (2) the larger PSF width observed at short wavelengths. These points are addressed in § 3.3 and further details can be found in Okumura 1998 [19].

During the laboratory test of the ISOCAM at IAS in the early 1990s, the detector surface was found to reflect a significant fraction of the incident infrared light. This causes multiple reflections between the detector and the filter surface creating ghost images with non negligible flux level. Tilting the filter plates was the adopted solution to reject a large fraction of this undesirable flux. However tilting the entire filter wheel needs too much modifications in the original design. Thus, the broad band filters were tilted 5° inside the filter mount without modifying anything but the filter wheel and filter mounts. However tilting a Circular Variable Filter (CVF) was impossible without tilting the filter wheel itself. Tilting the CVFs inside the mounts would have been difficult because of their large physical dimensions. Doing so, the CVF mounts would not have been able to keep the same order of mass as the original design, and it would have been necessary to revisit all the mass distribution inside the ISOCAM. Moreover, the 5° tilt of the CVFs would have displaced significantly parts of them from the telescope exit pupil image plane imposed by the field mirror, causing a poorer spectral resolution of the CVFs. Due to these technical difficulties, it was decided to keep the CVF mount as the original design.

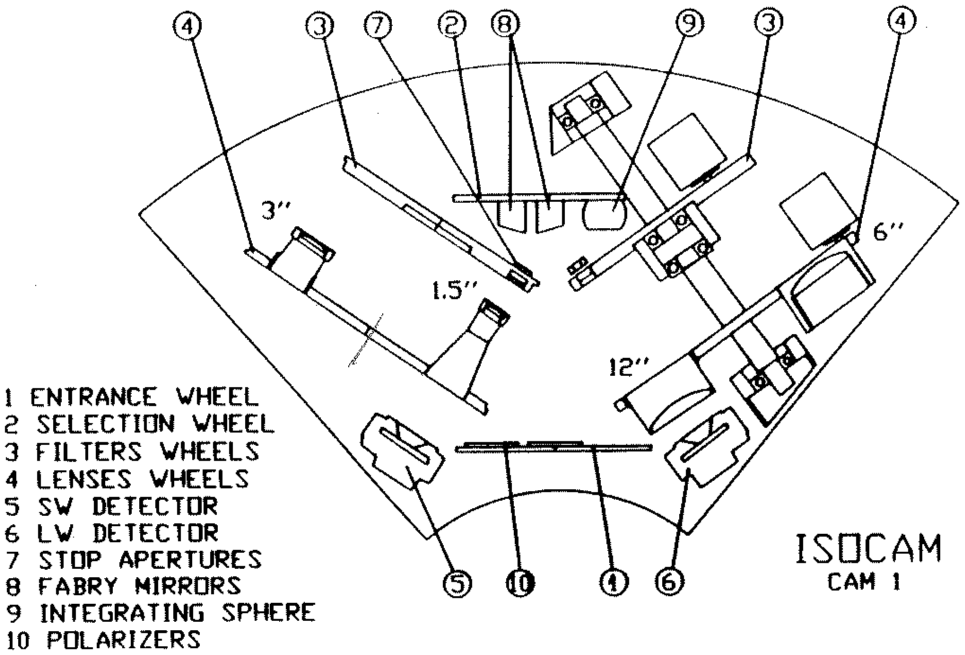

Figure 3.1: ISOCAM optical scheme

Therefore, it was known that the observations through the CVFs suffered from ghosts fluxes. This point is discussed in § 3.5 and further details can be found in Okumura 1998 [20].

It was also known that the ISOCAM image suffered from an optical field distortion. Its effect was already estimated with the laboratory test data before the integration of the instrument into the satellite. However, the first reliable model of the field distortion was developed from in-orbit data during the mission. The field distortion depends mainly on the lens, but it was suspected since the period of the first model that it may depend also on the filter. This wavelength dependency, however, was clearly measured for the first time only after the in-orbit operation. This point is addressed in § 3.7 and further details can be found in Okumura 2000 [18].

In the case of ISOCAM the extended source is directly calibrated from the point source calibration by means of a unit conversion (§ 3.4), which is not the case for the other instruments on-board ISO for which the instrumental beam profile plays a crucial role to calibrate the extended source. However, apart from its prime role of checking the ISOCAM's imaging quality, the ISOCAM PSFs are used for various goals, in similar ways as with any digital astronomical images. The ISOCAM standard product through the pipeline contains a point source catalog CPSL*.FITS produced using a PSF fitting procedure. This procedure provides the point source positions and their fluxes. It is also necessary to apply a PSF correction to produce any valid colour map. The deconvolution is another possibility of the use of the PSFs. However this use is limited by the fact that a large fraction of the ISOCAM observations are undersampled, and that the PSF shape may change according to the different degree of stabilization. The PSF library of the Cam Interactive Analysis (CIA) includes, for each instrumental configuration, when available, several PSFs of different positions with respect to the pixel centre. This improves the spatial sampling rate allowing to consider possible deconvolution methods. On the contrary, the stabilization issue for point sources is still a part of on-going works (Coulais [11]).

3.2 Instrument beam profiles

Measurements

The ISOCAM PSFs are measured in a micro-scan mode (raster with small step size) in order to improve the sampling rate imposed by the pixel size on the detectors. The target sources of the PSF measurements have been selected on the basis of their high visibility during the whole mission from the calibration source list established by the ground based preparatory program (Blommaert 1998 [7]). Tab. 3.1 lists all the observation available for the PSF measurements performed originally according to the In-Orbit Calibration Requirements Document (IOCRD) 3-4-1-1.

Data reduction

The data have been reduced in CIA using the following procedure:

- deglitch, method='temp'
- stabilize, method='ksig'
- average, /second
- corr_dark, method='calg'
- corr_flat, method='calg'

The point source images are then averaged by taking a subset of point sources which fall in the equivalent position with respect to a pixel centre in order to create a set of representative PSFs in the region of the detector covered by the micro scan.

Final products

In general, each configuration has a set of 9 PSFs corresponding to 9 different positions with respect to a pixel centre, except for PSFs through 12 arcsec pixel field of view (PFOV) lens which are sampled in 4×4 grid in a pixel. As listed in Tab. 3.1, the PSFs have been measured for all broad band LW filters through 1.5, 3 and 6 arcsec PFOV lens, whereas only LW1 and LW3 have been measured through 12 arcsec PFOV lens. For the SW channel, only SW5 has a complete PSFs. SW1 PSFs have been measured only through 12 arcsec PFOV lens. The PSFs of LW CVFs measured through 3 and 6 arcsec PFOV lens are strongly affected by the ghosts (see § 3.5) and their use needs a particular caution. For this reason, they are not included in the Cal-G file. The CAM PSFs are provided in 2 Cal-G files corresponding to 2 channels of ISOCAM: ccgswpsf_*.cube, and ccglwpsf_*.cube.

3.3 Deviation from the model

The CAM PSFs are modelled in two independent ways as extensions of the telescope model (§ 2.5). One of them uses the Fourier transform of the telescope aperture convolved by the pixel size. The other is performed by ASAP, the ray tracing program with a gaussian decomposition of the beam to simulate the diffraction of the light (Okumura 2000 [17]). Compared to the telescope PSF model, only pixel convolution effect is added to compute the ISOCAM PSF of a configuration as explained in § 2.5. For the ray tracing model, the following optical elements are added to model the ISOCAM.

Table 3.1: PSF calibration data

Filter	Lens	TDT No.	Positions	Target	Tint	comments
lw1	1.5	038031-32	1	HIC69713	0.28	very faint spider
lw1	3	038018-19	1	HIC89474	0.28	no arc seen
lw1	3	042046-47	1	HIC89474	0.28	no arc seen
lw1	6	038022-23	1	HIC77277	0.28	faint ghost
lw1	12	038026-27	1	HIC69713	0.28	near col.24, double star
lw1	12	038052-61	6	HIC69713	0.28	ghost, double star
lw1	12	244062-71	6	HIC69107	0.28	
lw2	1.5	Rev.100	1	HIC87833	0.28	killed by a saturation
lw2	1.5	140003-04	1	HIC92782	0.28	low level off-centered
lw2	1.5	846025-27	1	OH IR	0.28	cold PSF not included in Cal-g
lw2	3	119040-41	1	HIC77760	0.28	spider
lw2	6	093044-45	1	HIC80331	0.28	saturated with strong ghost
lw2	6	133046-47	1	HIC96441	0.28	ghost
lw2	6	342004-05	1	HIC85317	2.10	3x3 raster
lw3	1.5	100018-19	1	HIC87833	0.28	switched from lw2 saturation
lw3	1.5	119034-35	1	HIC80331	0.28	well seen arcs
lw3	1.5	510005-07	1	OH IR	0.28	cold PSF not included in Cal-g
lw3	3	119036-37	1	HIC80331	0.28	spider and arcs
lw3	3	342008-09	1	HIC98962	2.10	3x3 raster
lw3	3	426024-32	5	HIC98962	2.10	6x3 raster
lw3	6	119038-39	1	HIC74083	0.28	very faint ghost
lw3	6	201005-08	2	HIC78527	0.28	
lw3	6	342006-07	1	HIC96441	2.10	3x3 raster
lw3	12	244036-45	6	HIC77760	0.28	
lw4	1.5	189005-06	1	HIC78542	0.28	
lw4	3	182012-13	1	HIC78542	0.28	
lw4	6	300005-06	1	HIC78542	0.28	
lw5	1.5	175035,37	1	HIC84835	0.28	backgrnd failed
lw5	3	503022-24	1	HIC96441	2.10	
lw5	6	300007-08	1	HIC84835	0.28	
lw6	1.5	244049-50	1	HIC92782	0.28	
lw6	3	272027-28	1	HIC92782	0.28	unretrievable
lw6	3	510010-12	1	HIC101245	2.10	
lw6	6	272029-30	1	HIC92782	0.28	
lw7	1.5	014022-23	1	HIC92782	2.10	Tint=15
lw7	1.5	014027-28	1	HIC92782	0.28	failed
lw7	1.5	038033-34	1	HIC92782	0.28	faint arcs
lw7	3	038037-48	8	HIC70791	0.28	very faint tripod
lw7	6	042030-45	12	HIC74083	0.28	some ghost
lw8	1.5	175029-30	1	HIC87585	0.28	
lw8	3	189013-14	1	HIC87585	0.28	
lw8	6	189015-16	1	HIC87585	0.28	
lw9	1.5	038035-36	1	HIC87833	0.28	beautiful arcs
lw9	1.5	223004-05	1	HIC73005	2.10	
lw9	1.5	307018-19	1	HIC94779	2.10	3x3 raster
lw9	1.5	307020-21	1	HIC87585	2.10	3x3 raster
lw9	1.5	307024-25	1	HIC80331	2.10	3x3 raster
lw9	1.5	307022-23	1	HIC87585	2.10	3x3 raster
lw9	1.5	307016-17	1	HIC94376	2.10	3x3 raster
lw9	1.5	501042-45	2	HIC94376	2.10	6x3 raster
lw9	3	067013-14	1	HIC80331	0.28	spider and arcs
lw9	6	038024-25	1	HIC80331	0.28	ghost at bottom
lw9	6	133055-56	1	HIC80331	0.28	ghost at bottom
lw10	1.5	300003-04	1	HIC78527	0.28	
lw10	3	189007-08	1	HIC78527	0.28	
lw10	6	196005-06	1	HIC78527	0.28	killed by earth seeing accident
lw10	6	272031-32	1	HIC78527	0.28	
lw10	6	363008-10	1	HIC77277	2.10	3x3 raster
CVF	3	433008-10	1	HIC77760	2.10	6.221 μm
CVF	3	433011-13	1	HIC77760	2.10	8.379 μm
CVF	3	433014-16	1	HIC77760	2.10	10.52 μm
CVF	3	433003-05	1	HIC67459	2.10	15.0 μm
CVF	6	440015-17	1	HIC77760	2.10	6.221 μm
CVF	6	440018-20	1	HIC77760	2.10	8.379 μm
CVF	6	440012-14	1	HIC78276	2.10	10.52 μm
CVF	6	440005-07	1	HIC67459	2.10	15.0 μm
sw1	12	054004-11	6	HIC77760	0.28	faint ghost?
sw5	1.5	014025-26	1	HIC69713	2.10	Tint=15, double star
sw5	1.5	038028-29	1	HIC74083	0.28	double star?
sw5	1.5	066032-33	1	HIC69713	0.28	Tint=2, double star
sw5	3	042018-27	8	HIC69713	0.28	double star (companion at 15 pix)
sw5	3	363002-04	1	HIC73005	2.10	3x3 raster
sw5	6	046049-62	12	HIC69713	0.28	double star (companion at 8 pix)
sw5	6	363005-07	1	HIC73005	2.10	3x3 raster
sw5	6	524034-35	1	HIC85317	2.10	6x3 raster
sw5	12	475032-33	1	HIC85317	2.10	6x3 raster

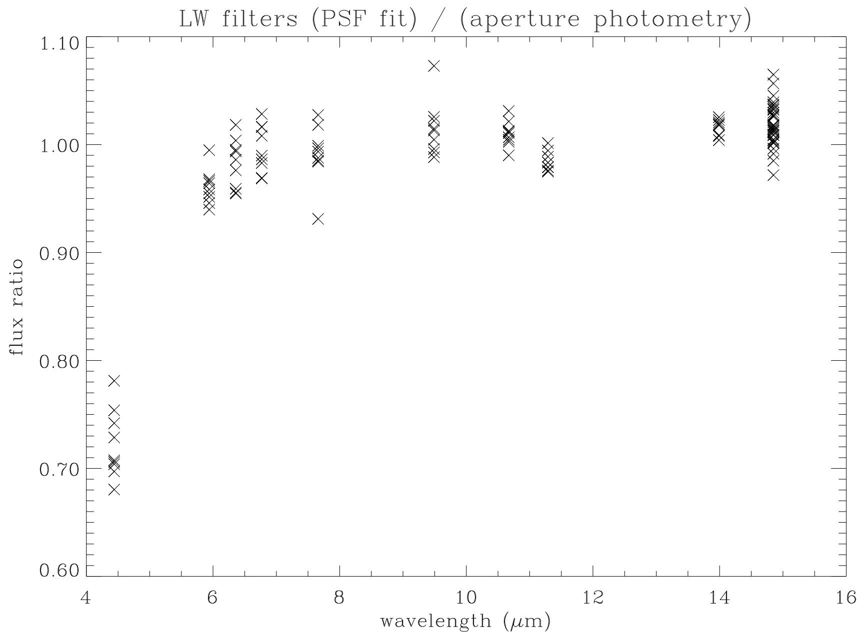

Figure 3.2: Ratio of the flux measured by the PSF fitting to the flux measured by the aperture photometry for the broad band filters through 1.5 arcsec PFOV lens. The PSF fit photometry underestimate the flux due to the narrowness of the computed PSFs.

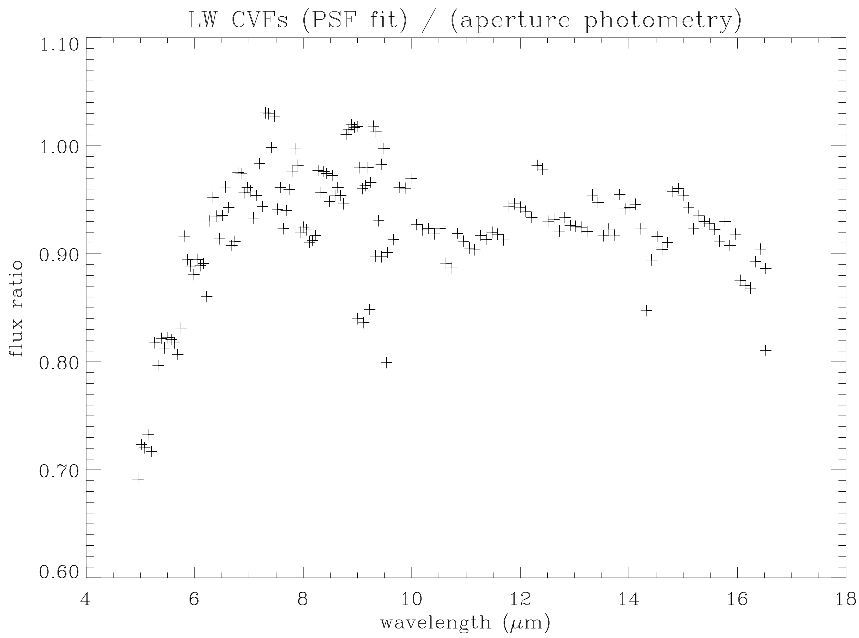

Figure 3.3: Ratio of the flux measured by the PSF fitting to the flux measured by the aperture photometry for the CVFs through 1.5 arcsec PFOV lens. The PSF fit photometry underestimate the flux because of the narrowness of the computed PSFs.

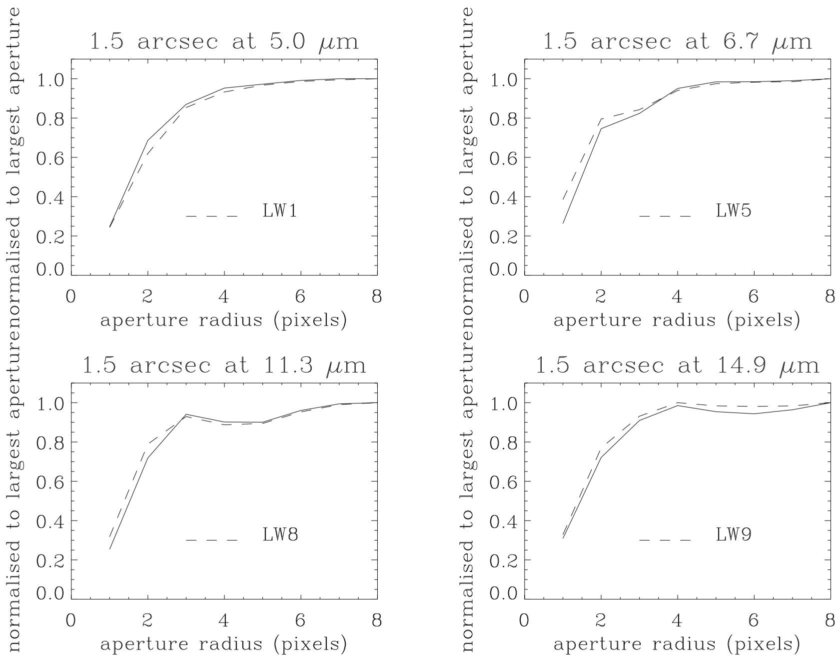

Figure 3.4: Aperture photometry of a point source with aperture correction using a computed PSF. The aperture correction stabilizes for aperture larger than 4 pixels corresponding to 6 arcsec.

- Field mirror
- Field stop
- Filter plates
- Filter mount
- Lens
- Lens mount
- Detector planes

Both models agrees well and reproduce in general the measured PSFs quite well. However, two predominant deviations are to be mentioned.

PSF asymmetry

Most striking one is the asymmetry especially seen on the first ring of the PSFs. Fig. 2.2 and 2.3 show an example of a typical asymmetry seen with LW9 filter. The amplitude of the asymmetry observed on the first ring of the PSF depends on the wavelength (Okumura 2000 [17]). It is suggested by the optical model of ISO telescope that a slight offset of the secondary mirror of the telescope can reproduce a similar asymmetry of the PSF. However, at this stage, no optical model parameter combination has been found which might reproduce the asymmetry amplitude variation over the whole wavelength range of the ISOCAM.

PSF width

Less obvious deviation is seen in the PSF width : the modelled PSFs are narrower than the observed one especially at short wavelength range. This effect is mainly seen with LW1 filter (Okumura 2000 [17]). However, the difference is also seen in other filters at short wavelength. This deviation of the PSF width results in a low value of the flux measured by the PSF fit compared to that of the aperture photometry. Fig. 3.2 shows that the ratio of these 2 flux measurements is small for LW1 at 4.5 μm, but LW4, LW2 and LW5 around 6 to 7 μm go gradually to the unity. This wavelength dependency is confirmed by the photometry through CVFs (Fig. 3.3). This effect is smeared out by the pixel convolution effect for the larger PFOVs. The PSF fit and the aperture photometry give a consistent flux through 6 arcsec PFOV. This deviation of PSF width may be due to the cross-talk in the detector for a sharp point source with low background corresponding to the shorter wavelength range (Coulais 2000 [11]) or it may also be due to an strong PSF asymmetry in the short wavelength range.

This difference of width between the model and the data implies that the flux of the point source should be measured by the aperture photometry and not by the PSF fit with computed PSFs. This is especially true for a configuration in the short wavelength range through a large PFOV lens. However, a computed PSF is also used in the aperture photometry for the aperture correction which aims to retrieve the flux outside the aperture. The flux measured by the aperture photometry is then also affected by the difference of the PSF width. Nevertheless this effect decreases rather quickly with the aperture. Fig. 3.4 shows the error on the flux measured by the aperture photometry as a function of the aperture. The lower flux value obtained for the aperture radius smaller than 6 arcsec is systematic and this can be corrected accordingly. The growth curve is also seen to be stabilized for an aperture radius larger than 4 pixels. This is consistent with the fact that the difference of fluxes between the aperture photometry and PSF fit is almost smeared out at 6 arcsec PFOV.

3.4 Extended source calibration

As ISOCAM has a detector matrices of 32 by 32, large enough to collect a large fraction of point source, and as the filling factor of the photo-sensitive surface is quite large (100% for LW and 89% for SW channel), the point source photometric calibration is directly applicable to any extended source. The conversion factors derived from point source observations (Blommaert 1998 [7]) which provide the physical flux in Jy per pixel from the ADU (Analog Digital convertor Unit) per gain per second are then directly applicable to the extended source. The surface brightness should then be expressed per a usual solid angle unit rather than per pixel area (Okumura 2000 [17], Salama 2000 [22]) using the following formula.

$$B = k\frac{F}{p^2}$$

where p is the pixel field of view in arcseconds, k is the conversion factor and F is the surface brightness in Jy/pix directly derived with the conversion factor in Cal-G files ccgswspec* and ccglwspec* The value of k depends on the adopted final unit. If B is expressed in MJy/sr, k is given by :

$$k = 10^{-6}\left(\frac{180 \times 3600}{\pi}\right)^2$$

However, some complications appear due to the ghosts produced by multiple reflections in the instrument. The ghosts appear with relatively strong fluxes especially in the images through the

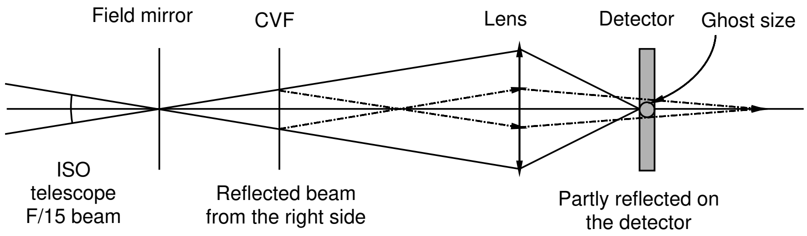

Figure 3.5: Optical scheme of the multiple reflections causing ghosts in the ISOCAM.

CVFs. Thus, an extended source surface brightness through a CVF suffers from a flux excess due to the ghosts. The conversion factors provided in the Cal-G files are based on the point source fluxes measured excluding the ghost contribution. This was because the flux contribution of the ghosts depends strongly on the position of the point source. Since the calibration observations could not cover all the possible point source positions on the detector, it was not convenient to consider the ghosts as a part of the PSF.

3.5 Ghosts in CAM-CVF

In the ISOCAM, the multi-reflection occurs between the filter plane and the detector plane and this generates ghosts in the image. Before the launch of the ISO, the large bandpass filters have were tilted 5° to reject the reflected beam from the nominal optical path. The CVFs were left without any tilt because of their large physical size (Pérault 1994 [21]). Further details about the ghosts in the ISOCAM can be found in Okumura 1998 [20].

Measurements

At an early stage of the calibration, it was seen that the ghosts of a point source through a CVF changed its shape and/or position as a function of the position of the source with 6 arcsec PFOV lens. The measurement tactics for this instrumental effect is then the contrary to the PSF measurements: raster observations with a relatively large step size in order to cover uniformly the detector surface in a limited observing time (Okumura 1998 [20]).

Tab. 3.2 lists the calibration observations aimed to measure the ghost effects.

Data reduction

A simple reduction procedure is applied to the data.

- deglitch, method='temp'
- stabilize, method='ksig'
- average, /second
- corr_dark, method='calg'

Table 3.2: Data for ghost measurements

Filter	Lens	TDT No.	Target	Gain	Tint	Mirror	Raster	Steps	Comments
LW1	3.0"	73000804	HIC98962	1	0.28	l	9×9	10",10"	
LW1	6.0"	73001003	HIC96441	1	0.28	l	9×9	21",21"	another star
LW1	6.0"	82501502	HIC94890	1	0.28	l	9×9	21",21"	
LW2	1.5"	80102303	HIC99663	1	0.28	s	5×5	9",9"	
LW2	3.0"	65500601	HIC77760	1	0.28	l	9×9	10",10"	
LW2	6.0"	62600201	HIC77760	1	0.28	l	9×9	21",21"	
LW3	1.5"	80102201	HIC98073	1	2.10	s	5×5	9",9"	
LW3	3.0"	62600502	HIC80331	1	0.28	l	9×9	21",21"	out of detector
LW3	6.0"	57600701	HIC87585	1	0.28	l	9×9	21",21"	
LW3	6.0"	65500201	HIC80331	1	0.28	l	0	0	lens jitter influence
LW3	6.0"	74004802	HIC87585	1	0.28	l	7×10	6",6"	discontinuity
LW7	3.0"	74101706	HIC102422	1	0.28	l	9×9	10",10"	
LW7	6.0"	73000905	HIC92782	1	0.28	l	9×9	21",21"	
LW8	3.0"	65500204	HIC80331	1	0.28	l	0	0	field mirror influence
LW8	6.0"	65500203	HIC80331	1	0.28	l	0	0	lens jitter influence
LW10	3.0"	73000902	HIC92782	1	0.28	l	9×9	10",10"	
LW10	6.0"	73000801	HIC98962	1	0.28	l	9×9	21",21"	
CVF1 5μm	1.5"	62600101	Gamma Dra	1	0.28	s	5×5	9",9"	pointing pb
CVF1 5μm	3.0"	57600801	Delta Dra	1	2.10	l	6×4	15",25"	
CVF1 5μm	3.0"	73000701	Delta Dra	2	2.10	s	6×4	15",25"	
CVF1 5μm	3.0"	84602202	Delta Dra	1	2.10	s	0	0	lens jitter again
CVF1 5μm	6.0"	53101501	Delta Dra	2	0.28	l	9×5	20",36"	
CVF1 5μm	6.0"	74005002	Delta Dra	1	0.28	l	8×16	6",12"	discontinuity
CVF1 5μm	6.0"	84602303	Delta Dra	1	2.10	s	0	0	lens jitter again
CVF1 7μm	1.5"	62600101	Gamma Dra	1	0.28	s	5×5	9",9"	pointing pb
CVF1 7μm	3.0"	73000701	Delta Dra	2	2.10	s	6×4	15",25"	
CVF1 7μm	3.0"	57600802	Delta Dra	1	2.10	l	6×4	15",25"	
CVF1 7μm	6.0"	53101602	Delta Dra	2	0.28	l	9×5	20",36"	
CVF1 9μm	1.5"	62600101	Gamma Dra	1	0.28	s	5×5	9",9"	pointing pb
CVF1 9μm	3.0"	57600803	Delta Dra	1	2.10	l	6×4	15",25"	
CVF1 9μm	3.0"	73000701	Delta Dra	2	2.10	s	6×4	15",25"	
CVF1 9μm	6.0"	53800403	Delta Dra	2	0.28	l	9×5	20",36"	
CVF1 9μm	6.0"	74005003	Delta Dra	1	0.28	l	8×16	6",12"	discontinuity
CVF2 9μm	1.5"	62600101	Gamma Dra	1	0.28	s	5×5	9",9"	pointing pb
CVF2 9μm	1.5"	77001002	Gamma Dra	1	0.28	s	5×5	9",9"	
CVF2 9μm	3.0"	57600804	Delta Dra	1	2.10	l	6×4	15",25"	
CVF2 9μm	3.0"	77001205	Delta Dra	2	0.28	s	6×4	15",25"	not enough S/N
CVF2 9μm	3.0"	85300202	Delta Dra	1	2.10	s	6×4	15",25"	better S/N
CVF2 9μm	6.0"	53800504	Delta Dra	2	0.28	l	9×5	20",36"	
CVF2 12μm	1.5"	62600101	Gamma Dra	1	0.28	s	5×5	9",9"	pointing pb
CVF2 12μm	1.5"	77001002	Gamma Dra	1	0.28	s	5×5	9",9"	
CVF2 12μm	3.0"	57600805	Delta Dra	1	2.10	l	6×4	15",25"	
CVF2 12μm	3.0"	77001205	Delta Dra	2	0.28	s	6×4	15",25"	not enough S/N
CVF2 12μm	3.0"	85300202	Delta Dra	1	2.10	s	6×4	15",25"	better S/N
CVF2 12μm	6.0"	53201005	Delta Dra	2	0.28	l	9×5	20",36"	
CVF2 15μm	1.5"	62600101	Gamma Dra	1	0.28	s	5×5	9",9"	pointing pb
CVF2 15μm	1.5"	77001002	Gamma Dra	1	0.28	s	5×5	9",9"	
CVF2 15μm	3.0"	57600806	Delta Dra	1	2.10	l	6×4	15",25"	
CVF2 15μm	3.0"	77001205	Delta Dra	2	0.28	s	6×4	15",25"	not enough S/N
CVF2 15μm	3.0"	85300202	Delta Dra	1	2.10	s	6×4	15",25"	better S/N
CVF2 15μm	6.0"	57600420	Delta Dra	2	0.28	l	9×5	20",36"	

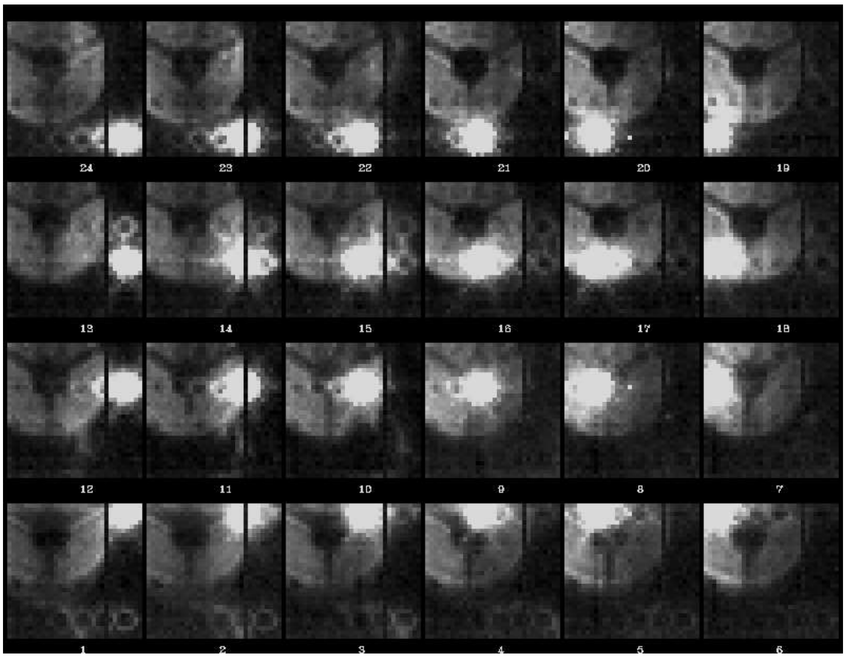

Figure 3.6: An example of ghost through 3 arcsec PFOV lens with a CVF at 7 μm

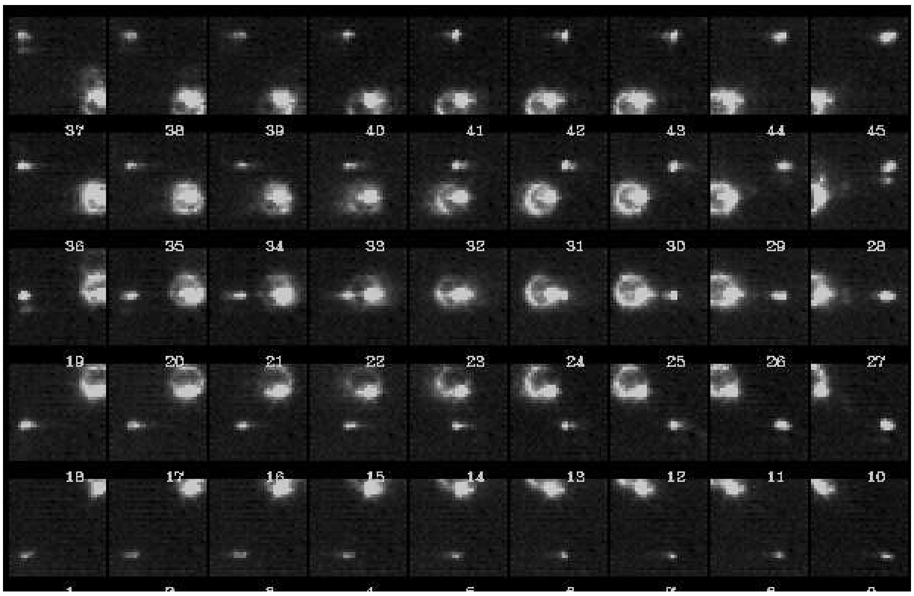

Figure 3.7: An example of ghost through 6 arcsec PFOV lens with a CVF at 7 μm

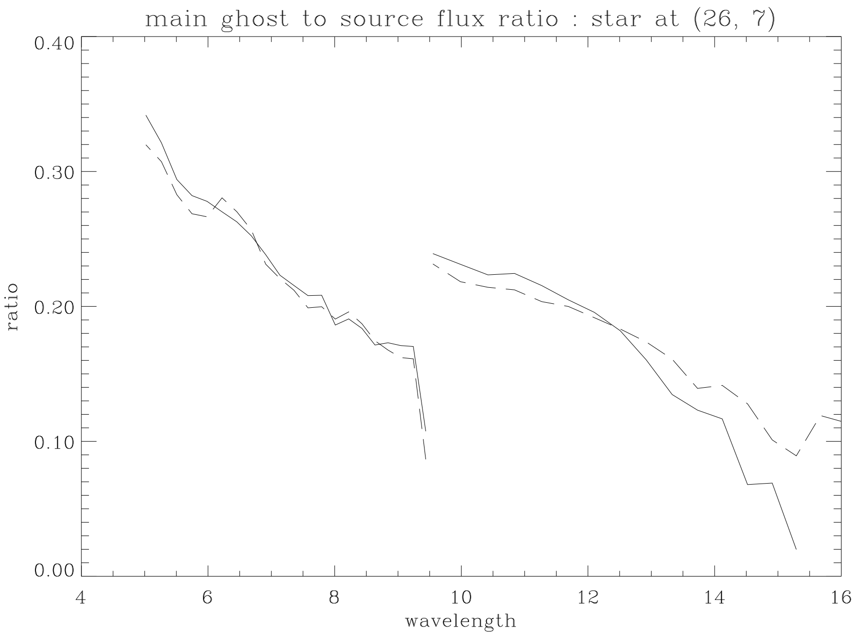

Figure 3.8: Ghost intensity as a function of the wavelength

- corr_flat, method='calg'

Figs. 3.6 and 3.7 shows a typical example of ghosts with a CVF at 7 μm through 3 and 6 arcsec PFOV lens. The ghost intensity depends not only on the position of the source but also on the wavelength as shown in Fig. 3.8, which makes all tentative correction difficult. An uniformly extended source such as the zodiacal light presents a surface brightness excess over the detector which varies as in Fig. 3.8. This flux excess is confirmed by the comparison between the mean surface brightness of the zodiacal light observed by ISOCAM through the CVFs and that of DIRBE on COBE (Blommaert et al. [8]).

Final products

At the present time, no ghost correction is available. Some routines concerning the ghosts behaviour are available in CIA.

3.6 Pointing accuracy between 2 LW CVF segments

There is in general a pointing offset between two LW CVF segments, even when these are used in a same AOT. This pointing offset arises from an optical reason. In general, if there is no intervention of manual commanding during an AOT observation, the lens wheel does not move. However, if the lens wheel moves between two observations of different CVF segments, the pointing offset may be larger than that expected by the optics. The lens wheel position has a noticeable tolerance and this introduces a well known random pointing error. There is no systematical way of correcting for the pointing when this occurs. However, it may be possible to offset the cube of images of one CVF segment relative to the cube of the other, if there is a structure sharp enough in the images of the overlapping wavelengths. It can be a star or the field mirror edge seen on the extended background emission. If there is no sharp structure in the images, it is impossible to determine the pointing difference between two CVF segments.

Table 3.3: List of calibration data for CVF SRF measurements

CVF	Wavelengths	Step	Lens	TDT No.	Target	Gain	Tint	Comments
LW1	9.583-5.446	4	1.5"	05804802	HIC94890	2	2.10	
LW1	9.583-4.956	1	3.0"	05804903	HIC94890	2	2.10	
LW1	9.583-5.446	4	6.0"	05805004	HIC94890	2	2.10	
LW2	16.70-9.003	4	1.5"	05805408	HIC94890	2	2.10	
LW2	16.70-8.782	1	3.0"	05805509	HIC94890	2	2.10	
LW2	16.70-9.003	4	6.0"	05805610	HIC94890	2	2.10	
LW1	9.583-4.956	1	3.0"	06200204	HIC96441	2	2.10	
LW1	4.956-9.583	1	3.0"	06200305	HIC96441	2	2.10	
LW2	17.34-8.782	1	3.0"	06200713	HIC96441	2	2.10	
LW2	8.782-17.34	1	3.0"	06200814	HIC96441	2	2.10	
SW	2.273-5.122	1	3.0"	06201222	HIC96441	2	2.10	
SW	5.122-2.273	1	3.0"	06201323	HIC96441	2	2.10	
LW1-	9.583-4.956	4	1.5"	06201502	δ Draconis	1	1.12	X-cal
-LW2-	17.34-8.893	4	1.5"	06201502	δ Draconis	1	1.12	X-cal
-SW	2.273-5.097	4	1.5"	06201502	δ Draconis	1	1.12	X-cal
LW1-	9.487-5.079	1	6.0"	06600401	Zodiacal	1	2.10	Extended
-LW2-	16.60-9.03	1	6.0"	06600401	Zodiacal	1	2.10	continued
-LW1-	5.070-9.438	1	6.0"	06600401	Zodiacal	1	2.10	continued
-LW2	9.03-16.60	1	6.0"	06600401	Zodiacal	1	2.10	continued
LW2	11.27-9.551-11.27	1	3.0"	06602001	NGC6543	2	2.10	
SW	2.273-4.996	4	6.0"	06602814	HIC94890	2	2.10	
SW	2.273-5.122	1	3.0"	06602915	HIC94890	2	2.10	
SW	2.273-4.996	4	1.5"	06603016	HIC94890	2	2.10	
LW1-	9.487-4.956	4	1.5"	07807002	δ Draconis	1	1.12	X-cal
-LW2-	17.34-8.893	4	1.5"	07807002	δ Draconis	1	1.12	X-cal
-SW	2.273-5.097	4	1.5"	07807002	δ Draconis	2	1.12	X-cal
LW1	4.956-9.583	1	3.0"	20305503	δ Draconis	1	1.40	
LW2	9.003-16.52	1	3.0"	20305604	δ Draconis	1	2.10	
LW2	9.003-16.52	1	1.5"	32800403	δ Draconis	1	2.10	
LW1	4.956-9.583	1	1.5"	32800504	δ Draconis	1	1.12	
LW2	8.782-16.52	1	6.0"	32800302	δ Draconis	1	1.12	
LW1	4.956-9.583	1	6.0"	32800605	δ Draconis	1	1.12	
LW2	8.782-16.52	1	3.0"	37000702	δ Draconis	1	2.10	
LW1	4.956-9.583	1	3.0"	37000803	δ Draconis	1	1.12	
LW1	6.511	0	6.0"	40600602	δ Draconis	1	1.12	no scan
LW1	6.511	0	3.0"	40600703	δ Draconis	1	1.12	no scan
LW1	6.511	0	1.5"	40600804	δ Draconis	1	1.12	no scan
SW	2.273-5.122	1	6.0"	40601802	HIC96441	1	2.10	
SW	5.122-2.273	1	1.5"	40601903	HIC96441	2	2.10	
LW2	9.003-16.52-9.003	2	1.5"	48206902	γ Draconis	1	1.12	
LW1-	5.018-9.438	4	6.0"	49600802	δ Draconis	1	1.12	bottom left
-LW2-	9.551-16.42	4	6.0"	49600802	δ Draconis	1	1.12	continued
-LW2-	16.42-9.551	4	6.0"	49600802	δ Draconis	1	1.12	continued
-LW1	9.487-5.079	4	6.0"	49600802	δ Draconis	1	1.12	continued
LW1-	5.018-9.438	4	6.0"	49600803	δ Draconis	1	1.12	bottom right
-LW2-	9.551-16.42	4	6.0"	49600803	δ Draconis	1	1.12	continued
-LW2-	16.42-9.551	4	6.0"	49600803	δ Draconis	1	1.12	continued
-LW1	9.438-5.018	4	6.0"	49600803	δ Draconis	1	1.12	continued
LW2	14.520-17.34-14.52	1	1.5"	80100702	γ Draconis	1	1.12	
LW2-	17.34-8.782	1	1.5"	83901902	Sirius	1	1.12	One block
-LW1-	8.993-6.684-8.993	1	1.5"	83901902	Sirius	1	1.12	continued
-LW2	8.782-17.34	1	1.5"	83901902	Sirius	1	1.12	continued

Measurements

The calibration data for the CVF spectral response function have been performed in the CUS (Calibration Uplink System) mode. Some of them are programmed in such a way to avoid the movement of the lens wheel between 2 CVF segments. In the normal observing mode (AOT) the movement of the lens wheel can provoke a pointing gap in the Y axis (horizontal in the CIA).

Data reduction

The calibration data for the CVF spectral response function measurement (Blommaert et al. [8]) are used to determine the eventual position gap when no lens wheel movement occurs. Tab. 3.3 lists the available data.

Final products

In the case where the lens wheel does not move between 2 CVF segments, an offset of ≈ -0.9 pixel is observed with 1.5 arcsec PFOV from CVF1 (5 to 9μm) to CVF2 (9 to 15μm). When the lens wheel moves between them, the pointing offset can reach up to ≈ 5, ≈ 3.5 and ≈ 2.8 pixels

Table 3.4: Data used for the field distortion measurements

6" data	observations	positions	mean S/N	simulated Δ_{max}	measured Δ_{max}
LW1 ghost	1	70	421	0.40	0.21
LW2 ghost	1	81	787	0.35	0.17
LW7 ghost	1	76	393	0.25	0.13
LW10 ghost	1	72	397	0.40	0.12
LW3 ghost	1	63	468	0.30	0.18
CVF1 at 5 μm ghost	1	40	312	0.70	0.29
CVF1 at 7 μm ghost	1	40	212	1.00	0.34
CVF1 at 9 μm ghost	1	40	231	0.40	0.26
CVF2 at 9 μm ghost	1	40	287	0.40	0.22
CVF2 at 12 μm ghost	1	40	170	0.35	0.25
CVF2 at 15 μm ghost	1	35	232	0.45	0.64
New LW1 data	5	266	4	0.65	0.60
New LW2 data	45	4768	14	0.10	0.24
New LW10 data	3	67	11	1.40	0.99
New LW3 data	17	1294	26	0.15	0.15

through 1.5, 3 and 6 arcsec PFOV lens respectively. No automatic correction is performed in the OLP.

3.7 Field distortion

The image on the focal plane of ISOCAM is distorted by several factors. This distortion of the field of view arises from the field mirror tilt, the total width of the filter materials and the surface curvature of the lens. The field mirror tilt introduces a trapezoidal deformation. The lens surface introduces a pin cushion distortion and the physical width of the filter plates changes the magnification. Further details about the field distortion can be found in Okumura 2000 [17] [18].

Measurements

Some raster observations around crowded field and around a bright star are used to measure the correspondence between the expected and the observed positions. Later new data sets have been added by selecting different observations of crowded regions in the ISO archive database and comparing them with 2MASS data for the astrometry (Ali et al. 2001 [1]). Tab. 3.4 lists the used data along with the simulated and measured final error.

Data reduction

For the first generation data, the reduction was performed with following step.

- deglitch, method='temp'
- stabilize, method='ksig'
- corr_dark, method='calg'
- corr_flat, method='calg'

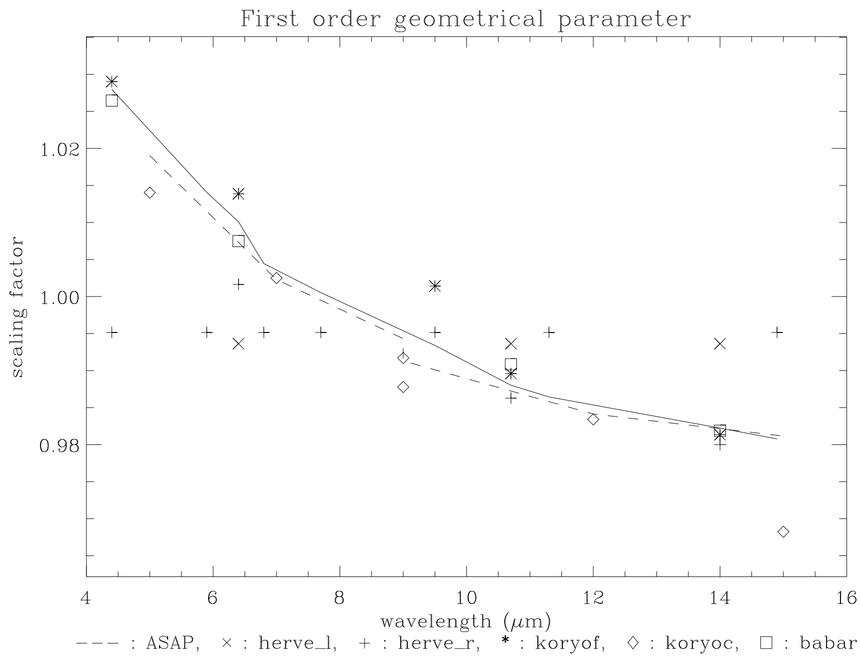

Figure 3.9: Scaling factor of the distortion correction computed from the first order coefficients. The wavelength dependency is clearly seen contrary to the correction of the first version represented by + and ×

The second generation data have been reduced with the transient correction by Fouks-Schubert method.

- corr_dark, method='vilspa'
- deglitch, method='mm'
- corr_transient, method='fs'
- corr_flat, method='auto' except for LW1 where method='calg'

The position of point sources is determined by the PSF fit procedure. The accuracy of the measured position depend on the signal to noise ratio of the source. Moreover, a systematic bias is introduced by the difference of width between the model and the observed PSFs (see § 3.3). Fig. 3.10 shows this bias which tends to give the point source position toward the pixel corner. In order to reduce this effect, a set of PSFs computed at 9μm was used for the LW2 new generation data instead of its effective wavelength of 6.36μm. The bias does not vanish completely but it is weaker as seen in Fig. 3.10.

The distortion is corrected by a polynomial pair for a given configuration. The polynomial coefficients are computed by a polynomial fit between the measured and expected star positions on the calibration data. The accuracy of the determined polynomials depends strongly on the signal to noise of the sources and their distribution on the detector.

The maximum distortion correction error on the detector area is estimated by the statistics on simulated data, taking into account the signal to noise ratio, the distribution of the star positions and the PSF bias. The fifth column in Tab. 3.4 lists the obtained values.

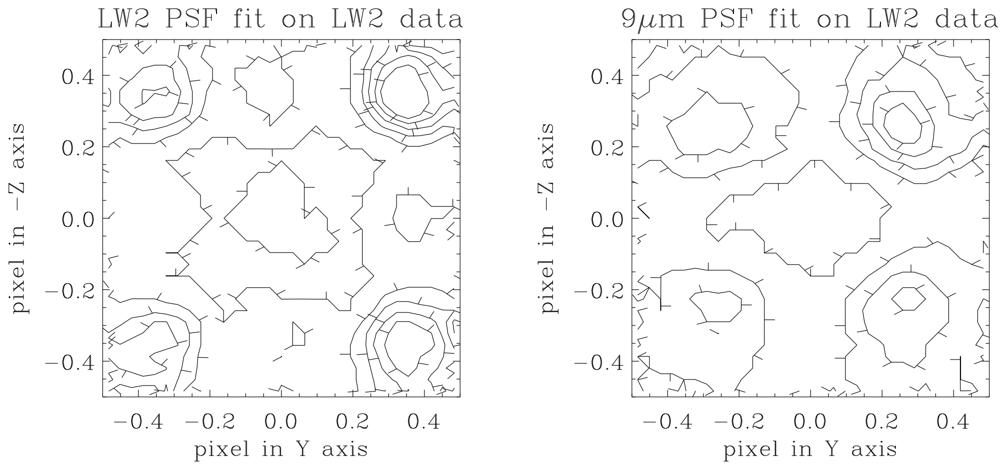

Figure 3.10: Due to the deviation of the width of PSFs, the point source position determined by the PSF fitting routine is biased toward the 4 corners of the pixel.

Optical model

The data available for the computation of the distortion correction polynomials do not cover all the possible configurations of ISOCAM. The use of an optical model appeared to be necessary to compute the correction coefficients for the missing configurations. The refractive indices of the materials of the ISOCAM optical elements has been adjusted as a function of the wavelength to reproduce the observed wavelength dependency of the field distortion.

The last column of Tab. 3.4 lists the maximum on the detector surface of the difference between the polynomials derived from the data and from the model. The random contribution of the lens wheel jitter is minimized by the criteria based on the curl of the distortion vector field (Okumura 2000 [18]). The fine tuning of the model parameters is performed in such a way that the maximum difference between the data and the model becomes lower than the simulated maximum error for all the available observations.

Final products

Fig. 3.9 shows the scaling factor derived from the first order coefficients of the distortion correction polynomials as a function of the wavelength. For the first version correction the values are mostly aligned on the middle value, because they are just copied from the result of LW10 measurements (Aussel 1998 [2], 1999 [3]). The other more recent measurements all show a clear dependency on the wavelength. The modelled distortions are shown in lines. The polynomial coefficients of the distortion correction of the first generation were provided in a set of ascii files. Those of the second generation (since version March 2001) are stored in a FITS ascii file. It contains the polynomial coefficients of all available configurations derived from the calibration data and also those of all the CVF wavelengths derived from the model. These files are used in the CIA to correct for the field distortion. The field distortion correction is not applied in the OLP.

3.8 Lessons learned

From the point of view of the optical design, it would have been better to tilt the filter wheel itself to avoid the ghost images with the CVFs. The optical models play an important role for the PSF calibration. For any optical modeling, the knowledge of the correct optical parameters is indispensable. It is obvious after our optical modeling exercise that a good information flow is crucial. Various optical models were developed in different places before the launch of the spacecraft. However, the ray tracing optical modeling activities stopped completely after the launch during the in-orbit operation. It was not a trivial task to find out the updated values of the optical parameters after the mission. It would have been useful to make a data base of all the optical parameters of the instrument and to update it each time a change occurred in the instrument design.

3.9 Conclusion

The observed ISOCAM PSFs are well reproduced by the optical model to the first order. However apart from the known optical artifact, further analysis revealed some deviations from the model : (1) the asymmetry especially seen on the first Airy ring and (2) the wider PSFs at the short wavelength range. The optical models can not reproduce the observed PSFs to reduce these deviations in a consistent way. However, all the parameter space of the model is not fully explored. The known optical artifacts of the ISOCAM are the ghost images and the field distortion. Refractive indices of the filters materials were adjusted to reproduce the observed field distortion with the ray tracing model. However other parameters such as misalignment of some optical elements may still improve the model. The field distortion correction polynomials for all the CVF wavelengths have been produced from the optical model. Further fine tuning of the model parameters are needed to reproduce the ghost images in a quantitatively correct way.

Bibliography

[1] B. Ali, S. Ott, T. D. Võ, R. Gastaud and K.Okumura The ISOCAM field-of-view distortion correction. *Proceedings The calibration legacy of the ISO mission*, ESA SP-481, 2001

[2] H. Aussel, ISOCAM LW channel field of view distortion. Technical report, 1998

[3] H. Aussel, ISOCAM LW channel field of view distortion measurements and correction. ISOCAM Calibration Workshop, 1999

[4] A. Biviano, B. Altieri., J. Blommaert, F. Boulanger, D. Cesarsky, K. Okumura, W. Reach, Topics in ISOCAM Spectroscopy Calibration. *Proceedings first ISO workshop on analytical spectroscopy*, 1997

[5] A. Biviano, B. Altieri., J. Blommaert, F. Boulanger, D. Cesarsky, L. Metcalfe, K. Okumura, W. Reach, The ISOCAM cvf calibration report. Technical report, 1998

[6] A. Biviano, The ISOCAM calibration error budget report. Technical report, 1998

[7] J. Blommaert, ISOCAM photometry report. Technical report, 1998

[8] J. Blommaert and K. Okumura, CVF photometry report. Technical report, 2001

[9] ISOCAM Observer's Manual. ESA, 1994

[10] A. Coulais and B. Fouks, Current status of modeling of point sources transient response for LW-ISOCAM. *Proceedings The calibration legacy of the ISO mission*, ESA SP-481, 2001

[11] A. Coulais and A. Abergel, Transient correction of the LW-ISOCAM data for low contrasted illumination. *Astron. Astrophys. Suppl. Ser.* 141, 533-544, 2000

[12] ISOCAM Interactive Analysis User's Manual. *Edited by Delaney M. Stockholm University*, 2000

[13] ISO Observer's Manual. ESA, 1994

[14] ISO document ISO AS 1100 RE 0438 European Space Agency 1989.

[15] K. Okumura, A. Babar, R. Gastaud and S. Ott, ISOCAM field distortion. in preparation, 2001

[16] K. Okumura, Optical properties of ISOCAM and/or ISO telescope. *Proceedings The calibration legacy of the ISO mission*, ESA SP-481, 2001

[17] K. Okumura, The ISO point spread function and CAM beam profiles. *Proceedings ISO beyond point sources: study of extended infrared emission*, 47–52, ESA SP-455, April 2000

[18] K. Okumura, ISOCAM field distortion report. Technical report, 2000

[19] K. Okumura, ISOCAM PSF report. Technical report, 1998

[20] K. Okumura, M. Pérault, Y. Longval and F. Sibille, Ghosts in ISOCAM images. Technical report, 1998

[21] M. Pérault et al. Infrared Space Observatory camera calibration facility and preflight characterization. *Optical Engineering* 33, 762, 1994, Provided by the NASA Astrophysics Data System

[22] A. Salama, ISO beam profiles and extended source flux calibration. *Proceedings ISO beyond point sources: study of extended infrared emission*, 7–10, ESA SP-455, April 2000

Chapter 4

The LWS Beam Profile

4.1 Executive summary

The effective aperture of the LWS is required in the calibration of extended sources and the beam profile itself is necessary for the calibration of point sources observed off axis. The LWS calibration is based on point sources, which are vignetted increasingly towards longer wavelengths, and the aperture of the LWS detectors is needed to calculate the point to extended flux ratio.

The mean beam profile has been determined for each of the ten LWS detectors from a series of observations of Mars at 57 positions in the LWS field. The positions lie on axis, and in a number of concentric squares, out to a radius of approximately $145''$. The alignment of the squares is coincident with the spacecraft Y and Z axes, and one of the primary optical elements of the LWS, the complex mirror, M2. The system of offset positions includes two pairs of orthogonal radial alignments which are used to investigate asymmetries in the beam profile.

There are two problems with off-axis observations that severely complicate the determination of the mean beam profile. The first is visible as a break down in the continuity of the fluxes between adjacent detectors in one part of the LWS field, which is referred to as spectrum fracturing. As well as introducing steep gradients into the spectra the mean flux levels are also changed, which produces an asymmetry into the beam profile. The effect is largest and has most impact in the core of the profile, and decreases at larger radii. The origin of the spectrum fracturing is unknown but the region of the LWS field affected is where the beam passes through a cut-out section of the field contour mirror. One possible explanation is that the outer part of the beam suffers specular reflection off the inside of the cut-out and then recombines with the direct beam. In this way the flux is increased and interference effects may produce the observed gradients in the spectra. It has so far not been possible to test this idea.

The second problem is fringing which appears as a sinusoidal modulation of the spectrum. The amplitude of the fringing increases with both wavelength and radius, up to $\sim 60''$ off axis. Fringing is seen in all of the outer part of the field except where the spectrum fracturing occurs. Fringing has a smaller effect on the beam profile as it is relatively simple to remove, however, this process is not perfect, so it will certainly increase noise and may introduce small systematic errors in the spectra. At the positions where the fringing is poorly defined, or non-existent, de-fringing the data will almost certainly remove features from the spectrum. There is also the implicit assumption that the fringing produces only a modulation of the spectrum and does not introduce a gradient.

In contrast to spectrum fracturing the fringing has a well established origin. It is caused by the interference between the direct beam from the complex mirror M2 and the reflection from its supporting substrate. In the regions where the fringing is well defined the change in fringe amplitude with radius is consistent with what is expected as the beam passes from M2 onto the substrate. Fringing is a complex phenomenon and the fringe phasing is found to be slightly variable across the field.

The effective aperture of the beam has been determined by convolving different apertures with the telescope point spread function (PSF) and minimising the residuals from the observed mean fluxes at each of the offset positions in each detector. Circular and elliptical apertures are unable to account for the asymmetry caused by the spectrum fracturing, so a composite semi-elliptical semi-circular aperture has been used, and although this is better, it still does not provide a good description of the subtleties the beam profile.

Apart from the asymmetry caused by the spectrum fracturing the evolution of the beam profile with wavelength is much as expected. At short wavelengths the telescope PSF is much smaller than the aperture and the beam profile is flat topped. At longer wavelengths the telescope PSF is larger than the aperture and the beam profile becomes more Gaussian. The shape of the profile due to the first Airy ring is well modelled. The general level of flux in the outer field is also consistent with the model although the observed fluxes do not precisely follow the asymmetries of the telescope PSF.

The aperture is found to be smaller than expected, $r \sim 40''$ as opposed to $\sim 50''$. The reason for this is unknown but it may be an effect of the Winston cones immediately in front of the detectors.

To correct extended source fluxes to the point source scale requires the effective aperture and a normalisation factor, usually called the extended source correction. The extended source correction is found by multiplying the aperture by the telescope PSF.

Extended source fluxes in the Trumpler 14 and 16 regions have been converted using the derived calibration and compared with IRAS 100μm fluxes of the same fields. In general the comparison is good, LWS/IRAS $= 0.9 \pm 0.2$ which lends confidence to the calibration.

4.2 Introduction

The mean beam profile and with it the effective solid angle of the detectors is required as part of the calibration of extended source fluxes. The effective solid angle is also required in the determination of the point/extended source flux correction. Both of these are necessary for the conversion of observed flux to flux.sr^{-1} for extended sources and for the calibration of sources observed in parallel and serendipity mode.

The mean beam profile is derived from a series of standard bias, grating scan observations of Mars. One observation was made on axis and the others were distributed around the field as shown in Figure 4.2. The mean flux in each detector at each of the offset positions is used to describe the radial sensitivity of the instrument and a parameterisation defines the mean beam profile. In addition subsets of the data along the four radial alignments, which are labelled PA30, PA75, PA120 and PA165 on Figure 4.2, have been analyzed to investigate possible asymmetries in the beam profile.

The spectra used to determine the mean beam profile are from a special processing of the raw data. The spectra are flux calibrated in the standard way and then de-fringed (see Section 4.6. The profiles are determined for each detector and are normalised to the flux observed on axis.

4.2.1 Optics

The optical train of the LWS consists of the contour field mirror (CFM) that allows a beam of $\sim 120''$ to fall on the complex field mirror M2, which is inclined at ~ 22 degrees to the incoming beam. M2 then presents an elliptical beam of $\sim 105 \times 97''$ (nominal FWHM) to the collimator, the LWS entrance pupil, the re-imaging mirror and detectors. Immediately in front of each detector is a rectangular aperture with rounded ends, which when projected onto the sky are approximately elliptical with dimensions of $104 \times 157''$ at SW1 and $138 \times 131''$ at LW5 in the along and across dispersion directions respectively. The long and short axes of M2 projected onto the sky are PA30 and PA120 (Y and Z axes) respectively.

As the detector apertures are nominally larger than the incoming beam from M2 it is, in fact, M2 that defines the aperture of the detectors, and the character of the optics determines the instrumental profile. For M2 this was simply assumed to be a rectangular profile. The size of the aperture was initially assumed to be $100''$ (the size of M2) but it has become clear that the beam is significantly smaller than this, for reasons that are not known. Perversely, the substrate that supports M2 is also reflective, particularly at longer wavelengths, and is responsible for the fringing that is seen off axis. However, a second consequence of this is that the supposed aperture will have weak wings out to $\sim 120''$ diameter (the size of the CFM).

The details of the arrangement of the CFM and M2 are shown in Figure 4.1. The CFM has a complex shape with a cut-out to allow the return beam from M2 to pass into the instrument. Unlike the central hole in the CFM, which is tapered opposite to the incoming beam, the edge of the cut-out is parallel to the optical axis.

4.2.2 Known problems

Some of the difficulties in describing the beam profile are apparent in Figure 4.3 which shows the spectra at each of the offset positions out to $\sim 30''$. The mean fluxes which are used to describe the mean beam profile conceal a wide range of variation with wavelength. In general the agreement between detectors (stitching) is good, and for the positions closest to the axis the relative flux is fairly constant. With increasing radius the relative flux becomes less constant and the fringing becomes more visible. However, in one sector, the negative RA offset (Figure 4.2), the spectra take on a fractured appearance.

Beam size

From the earliest estimates of the beam size it has been recognised that the beam is narrower than expected. The reason for this is unknown.

Fringing

Fringing is seen in observations of extended sources and point sources observed off axis. Interference between the beam from M2 and its substrate are responsible. See Section 4.6.

Spectrum fracturing

Observations of point sources in a particular part of the field and part of the flux from extended sources show a break down in the usually good stitching between adjacent detectors. A detailed description is given in Section 4.7.

Asymmetry

The mean beam profile is asymmetric mainly due to the effects of spectrum fracturing described above, but there are smaller effects that naturally introduce an asymmetry. These are the mirror M2 which is seen at an angle, and the tripod support of the secondary mirror which causes a small asymmetry in the telescope PSF. For further discussion see Section 4.5.

Non linearity

For some of the detectors, particularly LW3 Mars is a relatively strong source and the observations on, and close to, the axis suffer from saturation problems. At present these are not corrected.

Transients

None of the observations have been corrected for the transient response of the detectors, and this is general for the LWS.

4.3 The mean beam profile

The observed beam profile is the result of the convolution of the telescope PSF and the instrumental profile of each detector. As discussed above the detectors are assumed to have a simple aperture so the instrumental profile will be rectangular (top hat) by definition. Ideally the telescope PSF would be an Airy profile but the central obscuration and secondary supports, and any optical imperfections will conspire to redistribute power from the core of the profile to the Airy rings. Although a point source is being used to probe the structure of the beam, the PSF of the telescope, which is essentially an Airy profile, increases from ~ 25 to $100''$ (FWHM) between 46μm and 178μm, and at the longer wavelengths becomes comparable with the size of the aperture.

4.3.1 The convolution method

To determine the effective beam size the de-fringed observed mean fluxes have been compared with fluxes derived from a convolution of the telescope PSF with apertures of various sizes. The latest models of the telescope PSF includes the effects of the central obscuration and its supporting structure, and indicate that the power in the Airy rings is increased and that the wings of the profile contain 2-D structure. The asymmetry introduced into the profile is due to the three-legged secondary support.

Early in this exercise it became clear that the nominal value of the aperture of $100''$ was too large. The best value for most of the detectors lies close to $80''$, and for LW3, LW4 and LW5 is somewhat smaller than this. At the longest wavelengths the width of the telescope PSF is larger than the aperture itself which makes these determinations more difficult. An uncertainty of one arc second in the radius corresponds to about 5% in the effective area of the aperture. Figure 4.4 show the telescope PSF and orthogonal profiles through the convolution of the telescope PSF with an aperture of $40''$ radius.

It also became clear that a simple circular aperture could not adequately describe the asymmetry in the beam which is described in more detail in Sections 4.5 and 4.7. These effects are due to some complex (and unknown) behaviour of the beam and not due to a relatively simple non-circular aperture. However, in order to model the beam in a simple way it has been necessary to introduce a non-circular aperture. Of the infinite choice available a composite semi-circular and semi-elliptical aperture has been used.

4.3.2 Mars

Although Mars is treated as a point source it has a diameter of $6''$ which is small compared to the FWHM of telescope PSF of about $25''$ at 46μm and $100''$ at 178μm. However, the finite size of Mars does have a small effect on the profile of the telescope PSF entering the LWS which can be seen in Figure4.5. The effect is to fill in the sharp cuts (in log flux space) between the Airy rings while leaving the rest of the profile largely untouched. Although it is strongest at the shortest wavelengths the effect is still visible into the LW detectors.

4.3.3 Low-bias data

Mars is a relatively bright source and it is believed that some of the detectors, particularly LW3, suffer from saturation problems when Mars is observed on axis. Two low-bias observations of Mars on axis were obtained with the intention of quantifying the level of saturation. When the detectors saturate the flux is underestimated, so the slope of the ratio of the low to standard-bias spectra should give some measure of the flux lost. Initial results show a range of variation from close to zero for SW2, to 5–10% for some detectors. LW3 shows a modest difference of $\sim 2\%$. Until these results are better understood no attempt has been made to correct for any saturation effects.

4.3.4 Results

The convolution was performed over a range of radii r and semi-major/minor axes b of the components of the aperture. The aperture was always continuous so that one axis of the semi-elliptical part was always equal to the radius of the semi-circular part. Numerous experiments were performed to determine the best orientation of the aperture. The results were not particularly sensitive to the value chosen so ultimately this was fixed for all detectors.

For each convolution the observed, de-fringed fluxes were compared on a point by point basis with the calculated flux at each position in its correct location in the Y-Z plane of the telescope PSF, and the residuals calculated. To estimate the goodness-of-fit four different measures were used. These were (i) the sum of the absolute residuals, (ii) the sum of the squares of the residuals, both in linear flux, and (iii) and (iv) the same quantities in ln flux. There are several reasons for considering different measures. Firstly, the errors in fitting the observed fluxes are not Gaussian but dominated by systematic effects, such as the asymmetry in the beam, and under these circumstances the sum of the absolute residuals might give a less biased result. Also the weaker fluxes at the edge of the field are given disproportionately low weight in linear flux space. Ideally all four measures should point to the same set of aperture parameters but if they do not then they will give some indication of where the inconsistency lies.

The plots of the goodness-of-fit measures on the $r - b$ grids are given for all the detectors in Figures 4.6 to 4.10. Although there is some variation between detectors for SW1 to LW2 there is usually a good measure of agreement between the different measures of the goodness-of-fit. For LW3 to LW5, and SW5 there is a more systematic difference between the linear and ln flux measures, which indicates a systematic difference in the best-fit profile between the inner and outer part of the beam. The changing density of contours also indicates a considerable variation in the quality of the fit, both across the detectors and for the different measures of the goodness-of-fit. Under these circumstances any values of the best-fit parameters are a compromise, so the adopted values of r and b were taken to be where the volume of the figure described by the residuals passes through zero, in the region of the minima in the goodness-of-fit measures. Along this line various combinations of r and b are possible but over a sensible range the numerical uncertainty in the area of the aperture is $\sim 2\%$.

The relative mean flux at each of the observed offset positions (see Figure 4.2) is shown for each detector in Figure 4.11 with the convolution of the telescope PSF and the best fit composite aperture superimposed. At shorter wavelengths the telescope PSF is narrow enough to probe the structure of the rectangular (top-hat) instrumental profile and some indication its shape can be seen. As the telescope PSF broadens towards longer wavelengths the details of the instrumental profile become washed out and the observed profile becomes more Gaussian.

4.3.5 Flux correction for extended sources

The LWS flux scale is based on a point source calibration, although beyond the diffraction limit at about 110μm a substantial fraction of the flux from an on-axis point source if diffracted out of the aperture. In fact there are significant diffraction losses for all LWS detectors but provided the calibration is applied to point sources observed on axis these losses are irrelevant. However, for (ideal) extended sources similar diffraction losses do not occur, and so a correction has to be applied to correctly place the derived fluxes on the point source calibration scale. To do this requires the effective aperture of each detector and the PSF of the telescope.

The extended source correction is the measure of the fraction of flux in the telescope PSF that lies within the detector aperture. For this the best-fit apertures are used which have a top-hat instrumental profile by definition. The correction factors are given in Table 4.2.

4.4 Extended source flux per unit area

To convert the observed fluxes of extended sources to flux.sr^{-1} requires both the extended source correction factor and the effective aperture explicitly.

The corrected extended source flux for an observed flux F (Jy),

$$S = F.f/(\omega * 10^6) \text{ MJy/sr}$$

where f is the extended source correction and ω is effective solid angle of the beam (sr).

However, these corrections are derived under the assumption of a smooth and very extended flux distribution. In the real world, structure or embedded sources could produce significant discrepancies from the ideal situation, and with it differences in flux.

Table 4.1: Effective Aperture Radius

Detector	Radius ($''$)	Detector	Radius ($''$)
SW1	39	LW1	38
SW2	42	LW2	39
SW3	43	LW3	35
SW4	41	LW4	34
SW5	40	LW5	33

4.4.1 Comparison with IRAS

LWS observations have been made at a number of positions in the Trumpler 14 and 16 fields and these have been compared with the IRAS 100μm fluxes at the same positions. Both fields contain a large area of extended emission, which although relatively smooth, does change by a factor of 2 – 3 within each region. Figure 4.12 shows the comparison of the converted LWS and IRAS 100μm fluxes using the current LWS calibration and these measurements give a mean ratio, LWS/IRAS $\sim 0.9\pm0.2$. Ideally for this comparison the extended flux should be distributed as evenly as possible, and part of the uncertainty is probably due to unresolved structure within the beam.

For fields containing multiple sources the observed flux will depend critically on the precise positions of the sources relative to the optical axis. To recover or model the observed flux will require positional information on the sources and a deconvolution with the telescope PSF and instrumental profile. Indeed, for single point sources observed off axis a similar procedure will be required to recover the correct flux.

4.5 Asymmetry

It is already clear from Figure 4.11 there is some asymmetry in the beam profile, with groups of points lying systematically off the lines. It will be seen later that the question of symmetry is not straight forward, and a simple analysis of the relative mean fluxes for the four radial alignments begins to show this.

The radial alignments are a subset of the data which define the global mean profiles. The four alignments are separated by approximately 45 degrees to create two orthogonal pairs, with the PA30 set aligned along the Y axis, and the PA120 set aligned along the Z axis of M2. These positions were originally chosen to test for any asymmetry introduced into the beam by M2.

Each of these alignments contains nine points but the radial distribution of the alternate pairs is rather different. A Gaussian profile constrained to the optical axis was fitted to each set with the on-axis point and those with $r > 65''$ excluded. The main concern with this process is the poor statistics. Although each alignment contains nine points, only six points are used in the PA30 and PA120 solutions and only four points in the PA75 and PA165 solutions.

Of the parameters derived from these solutions the FWHM are probably the most reliable, and these are shown in Figure 4.13. Although there is considerable scatter the behaviour is fairly consistent. Each alignment shows an increase in FWHM through the SW detectors and then a subsequent decline, which reflects the behaviour of a Gaussian fit to all the data, and the run of effective aperture sizes in the table above. In more detail it can be seen that the alignments fall naturally into two pairs with very similar behaviour. PA75 and PA120 show much more variation than PA30 and PA165, and peak at SW3 as opposed to SW5. All four alignments show

Table 4.2: Extended source corrections and effective beam sizes.

Detector	f	$\omega * 10^6$	Detector	f	$\omega * 10^6$
SW1	0.88	0.114	LW1	0.69	0.107
SW2	0.88	0.130	LW2	0.69	0.111
SW3	0.84	0.135	LW3	0.62	0.092
SW4	0.73	0.117	LW4	0.55	0.088
SW5	0.70	0.114	LW5	0.48	0.083

the little feature at LW2 and an increase in FWHM from LW3 to LW5. It might be expected that the variation is in some way symmetrical with respect to the axis of M2. The alignments PA30 and PA120 are the orthogonal axes of M2 and might be expected to show the extreme values. PA120 certainly has the narrowest widths, and is systematically smaller than PA30 but the intermediate alignments PA75 and PA165 show a similar level of disagreement. The mean ratio of the Y and Z axis FWHM is 0.93 which is remarkably, if not reassuringly, similar to the expected ratio of the ellipticity of the beam from M2, ie. 0.93. The level of agreement with the predicted value must be a little fortuitous given the scatter in the measurements.

4.6 Fringing

The fringing that appears at positions off axis is due to interference between the direct beam from M2 and the reflection from its supporting substrate. Optical modelling suggests that the phasing of the fringing should remain constant across the field of view. The relative fringe amplitude should increase with radius until the amount of the beam reflected from M2 and the substrate, is approximately equal, which should occur as the core of the profile slips off M2 and onto the substrate, at $r \sim 50''$. As the beam moves off the substrate the fringing should decrease and then possibly show a secondary maximum where the first Airy ring illuminates the substrate.

Figure 4.14a shows the relative flux in the LW detectors at three positions on PA30 and PA120, all at a radius of $61''$. Two of the positions, 16 and 36, are opposite and 23 is orthogonal. For positions 16 and 23 it is immediately clear that the fringe phasing is not constant and between positions 16 and 36 the phasing seems to change with wavelength. The fringe amplitude is clearly a function of wavelength. There is also some difference in the fringe amplitude at the same radius and this is seen more clearly in Figure 4.14b, which shows the fluxes at another trio of positions at a radius of $55''$ from PA75 and PA165.

An illustration of the radial distribution of the fringe amplitude is given in Figure 4.15a which shows the relative fluxes in LW4 at positions on and between PA75 and PA120 (positive RA offset). The amplitude increases steadily to $r \sim 60''$ but practically vanishes by $r \sim 90''$ only to show a slight increase again by the edge of the field, as predicted by the model. Figure 4.15b shows the fluxes at eight positions around the edge of the field which show considerable variation in the fringe visibility.

The fringe amplitude is clearly a function of wavelength and also shows a variation with radius. To quantify the fringe behaviour the amplitude and phase, assuming a fixed fringe period, have been taken from the de-fringing routine. Figure 4.16a shows a map of the relative fringe amplitude in LW4 and LW5 where the fringing is at its largest. The fringe amplitude shows an approximately circularly symmetric structure which increases sharply up to a radius of $\sim 50''$ and then falls away. For LW5 the pattern is very clear but it can also be seen that the fringing is not as strong in left hand part of the field, which is where the spectrum fracturing occurs. At shorter wavelengths the contrast between the left and right parts of the field is particularly striking and the reduction in fringing in the fractured region is clear. Although it is not particularly clear from Figure 4.16a the amplitude of the fringing at the very edge of the field varies considerably with position.

From simple arguments the phasing of the fringe pattern is expected to remain constant across the field but in fact this is not the case. For LW4 and LW5, where it is best defined (see Figure 4.16b), the fringe phasing is more constant on the right side of the field but in the fractured region the phasing becomes irregular and poorly defined, in much the same way as the fringe amplitude. However, even where the fringing is well defined, for example at offset positions 16 and 23, it has been seen previously that the phasing of the fringes is significantly different.

The fringing that is seen in extended sources and point sources observed off axis is broadly consistent with it being produced by the interference between light reflected from M2 and its supporting substrate. The relative fringe amplitude is approximately circularly symmetric and its radial behaviour is consistent with the movement of the beam from M2 on to the substrate. However, the fringing is complex; in the fractured region it is reduced or eliminated, and the phasing of the fringe pattern is not constant even where the fringes are well defined.

In order to parameterise the fringe phase and amplitude behaviour across the instrument it is necessary to fit and determine the fringe pattern. Figure 4.17 is simply to illustrate some of the difficulties of this process. The spectrum contains features that will confuse the fit and the model does not always appear to adequately fit the fringing. The relative fringe amplitude and the relative flux can change significantly across one detector which undermines a simple parameterisation.

4.7 Spectrum fracturing

The mean fluxes conceal a wide range of variation with wavelength at each of the offset positions as is clearly seen in Figure 4.3. The flux relative to the on-axis value at each wavelength across all detectors at the inner four raster positions on each alignment. In general the agreement between detectors (stitching) is good and for the positions closest to the axis the relative flux is fairly constant. With increasing radius the relative flux becomes less constant and the fringing becomes more visible. However, in one sector, the negative RA offset (Figure 4.2) between PA75 and PA120, the relative fluxes show a very different, fractured pattern (positions 27, 28, 30 and 35). The same effect may also be weakly visible on PA165 (positions 19 and 20) but does not appear to affect PA30 (positions 31 and 34). The origin of this fractured pattern in the fluxes is presently unknown but the part of the beam affected is the edge that passes close to the cut out in the contour field mirror, between M2 and the collimator. At shorter wavelengths the flux levels are generally higher in this region compared to similar radii in other parts of the beam, and at longer wavelengths the effect of fringing is suppressed. The spectrum takes on a broken or fractured appearance with large discontinuities between detectors. The effect is worse at shorter wavelengths and for the SW detectors it introduces a strong gradient in the flux with wavelength. The variation of the mean flux in the fractured region is the main cause of the asymmetry in the beam, and the difficulty in modelling it.

The relative fluxes at various positions are shown in more detail in Figure 4.18. By a radius of $90''$ the behaviour of the fluxes in the LW detectors are relatively similar across the whole field but in the affected sector the SW detectors still show the fractured pattern.

4.8 Lessons for the future

4.8.1 Looking back

Of the three main problems with LWS data, beam size, fringing and fracturing, only the fringing has a clear origin. All the evidence points to this being due to interference between the light reflected from M2 and its substrate. For future missions there is a clear lesson.

In the other two problems these is no clear cause although there are indications. The fractured region lies in the part of the beam that passes through the cut-out on the CFM and it is possible to speculate on two possible effects. The first is a simple vignetting of the beam, but it is difficult to see how this could produce an increase in flux over similar radii in other parts of the field, and produce a strong wavelength dependence. The second possibility is that the beam is partially reflected off the cut-out (grazing incidence) which could conceivably return more flux to the beam and through interference effects produce the anomalous wavelength dependence.

The origin of the reduction in beam size is unknown and there is nothing to indicate where the problem lies. However, there are two possible origins of this problem that have been considered. The first is in the Winston cones that lies immediately above the detectors. These were tested only for the on axis beam and modelling suggests that in a converging beam seen off axis the field is vignetted.

The second possibility is a small misalignment in M2. The complex mirror M2 is a critical element in the optical chain and a small misalignment would throw the outer part of the beam into a field stop. However, this would probably just displace the beam and vignette one part field rather than produce an over all reduction in beam size.

4.8.2 Looking forward...

Although it is not possible to clearly identify the origin of all the problems in LWS grating spectra there are lessons for the designers of similar instruments in the future. The single loudest message from this study is the need to seriously consider the off axis characteristics of the instrument, to include them in the design, and to test them.

Financial, weight and size constraints will always affect instrument design but if it is intended to work off axis then the components necessarily have to be an appropriate size.

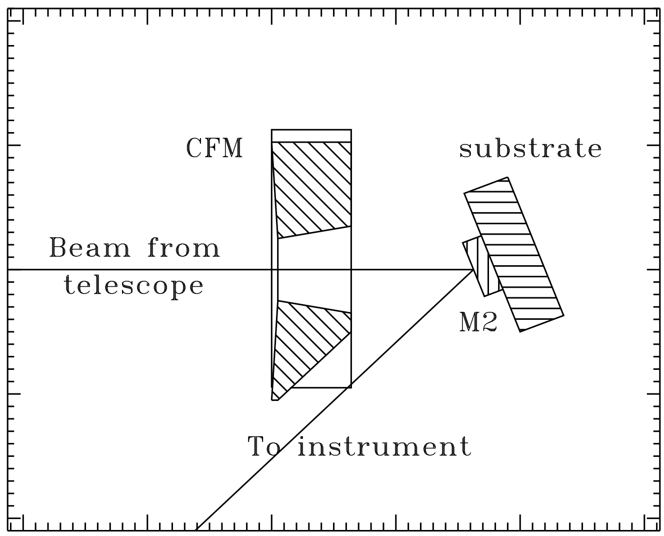

Figure 4.1: *A section through the optical components between the telescope and the main LWS instrument. The beam passes through the contour field mirror (CFM) and then on to the complex field mirror, M2, and then into the instrument. There is a cut-out section in the back of the CFM to allow the beam to pass.*

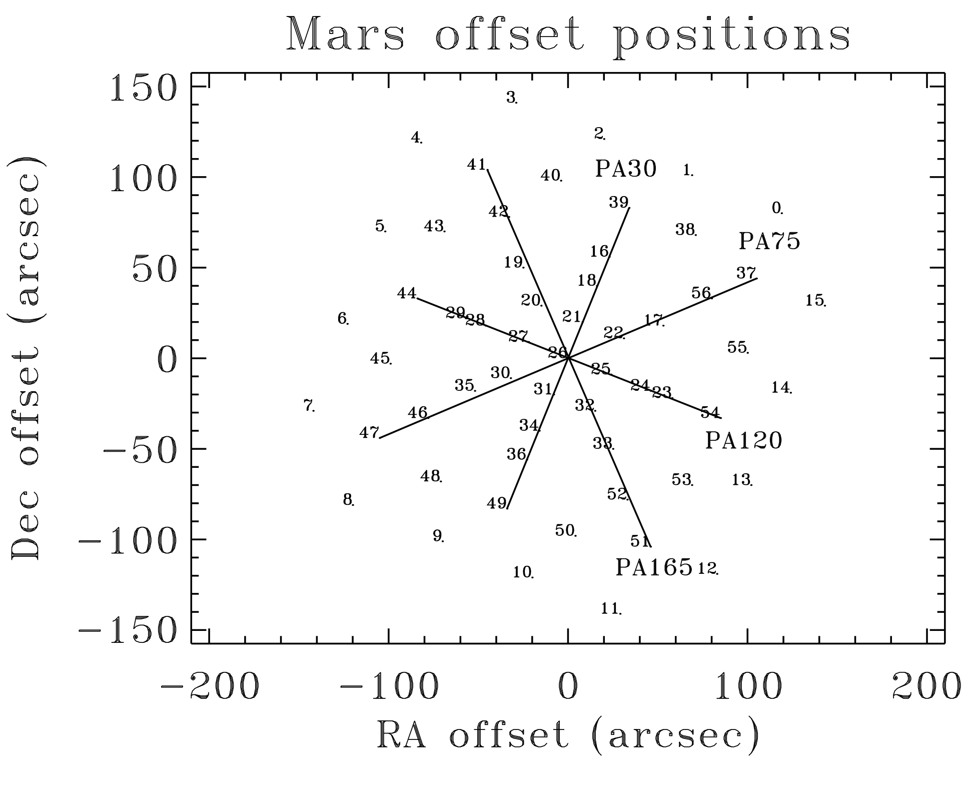

Figure 4.2: *Offset positions of the Mars beam profile observations.*

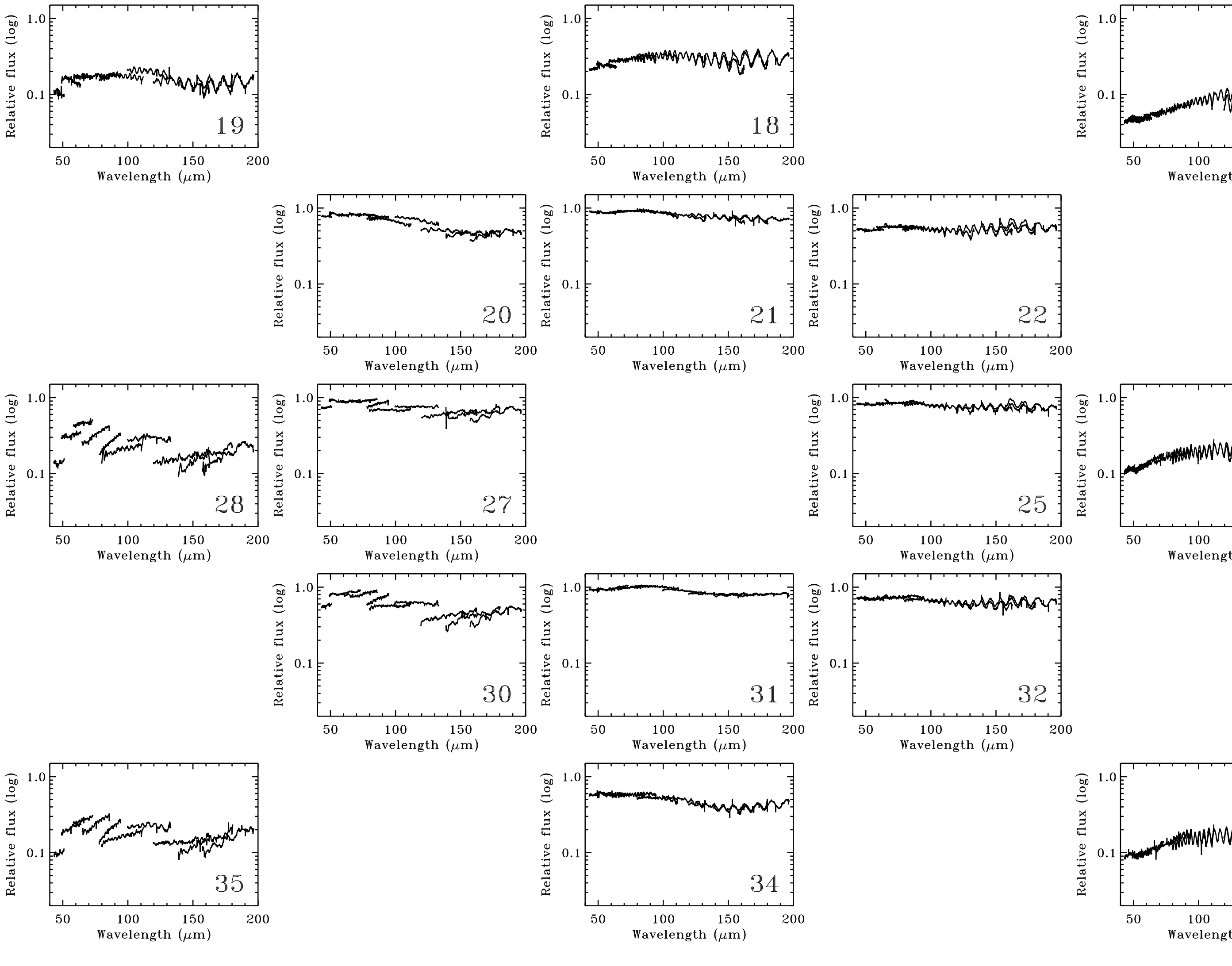

Figure 4.3: *Relative fluxes for the inner region. In this plot PA30 is vertical.*

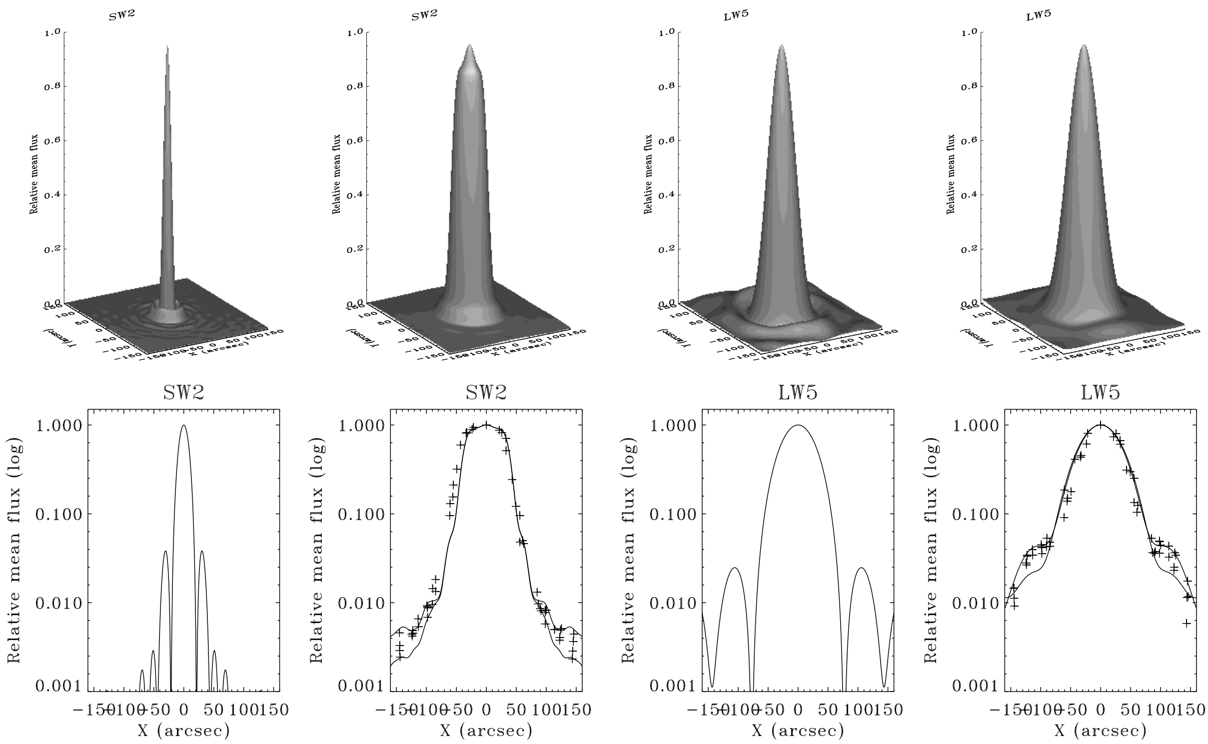

Figure 4.4: *Linear and log flux plots for SW2 and LW5 showing the telescope PSF (left) and its convolution with a $40''$ radius aperture (right). The two lines lines are orthogonal plots through the profile.*

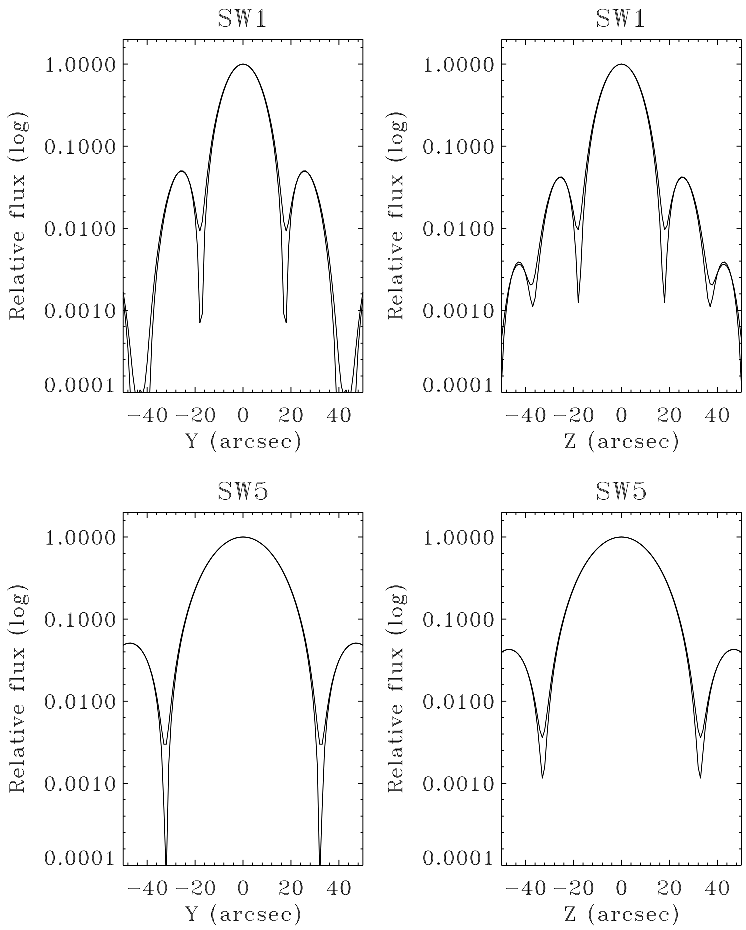

Figure 4.5: *The effect of a finite size for Mars on the telescope PSF shown for the telescope co-ordinates Y and Z.*

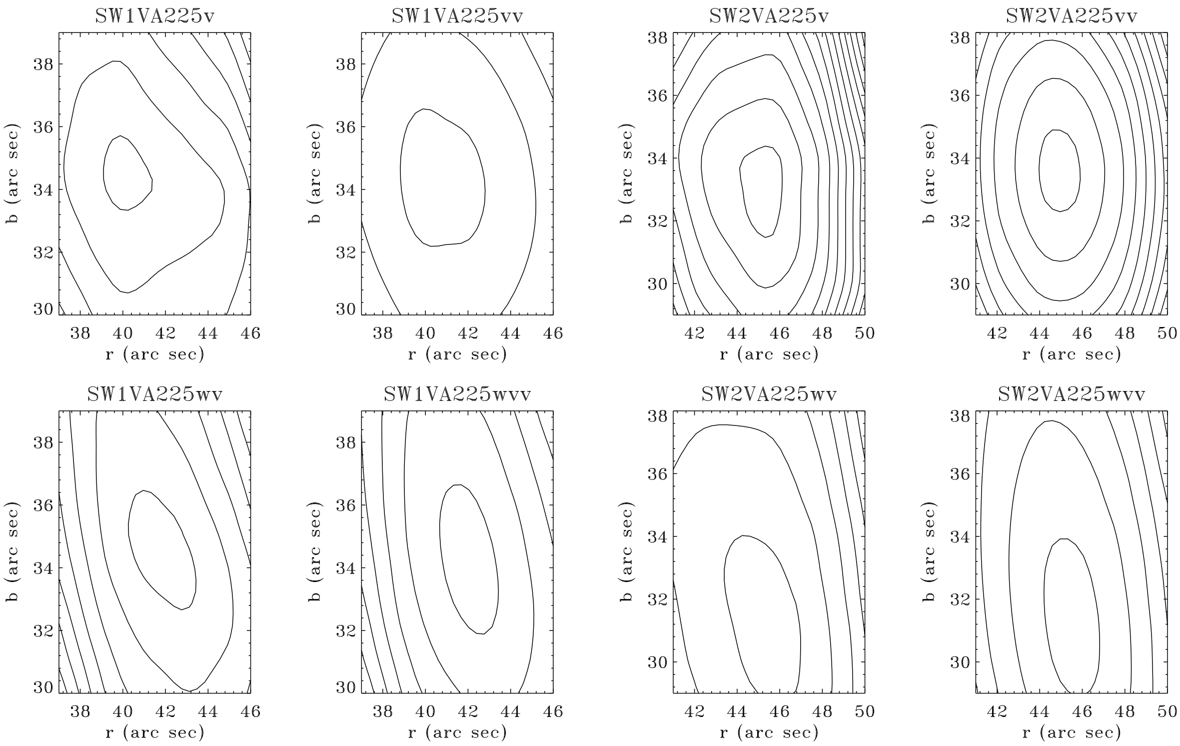

Figure 4.6: *Contours of the goodness-of-fit measures for SW1 and SW2. The top pair in each case is in linear flux space and the lower pair in ln flux space. The left hand pair are the sums of absolute residuals and the right hand pair are the sums of the residuals squared. The contour levels are in units of $\sigma/2$, relative to the minimum and are the same in each plot.*

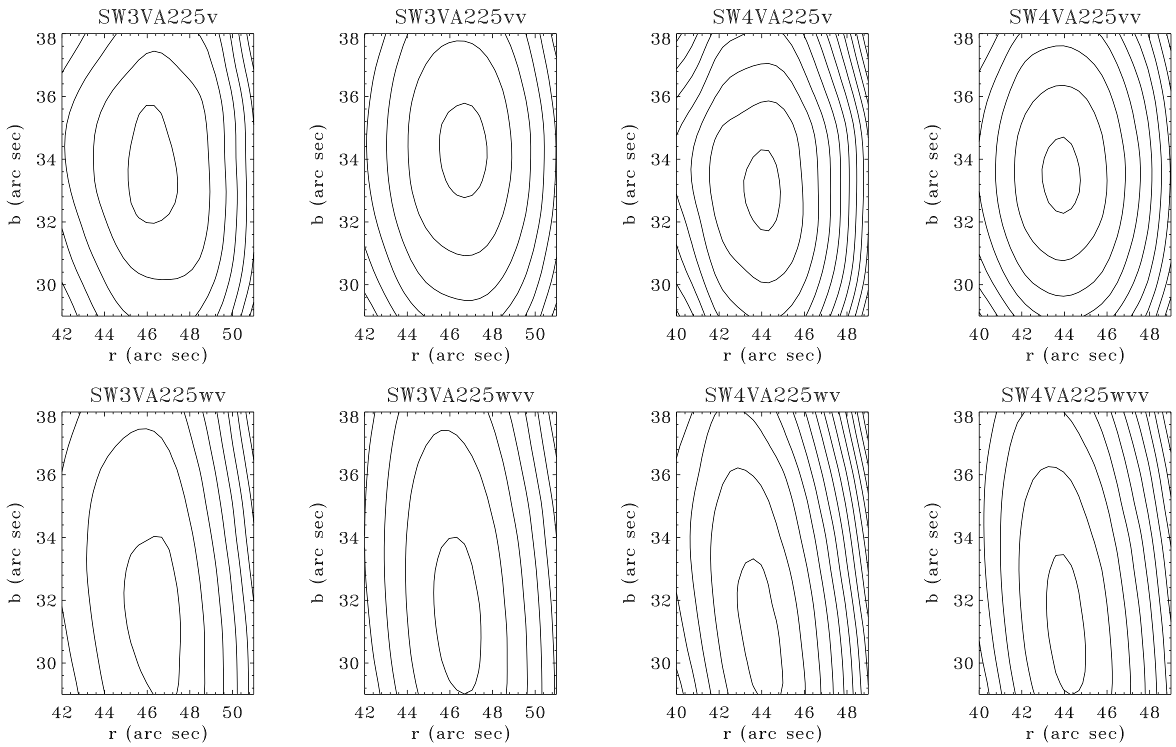

Figure 4.7: *Contours of the goodness-of-fit measures for SW3 and SW4.*

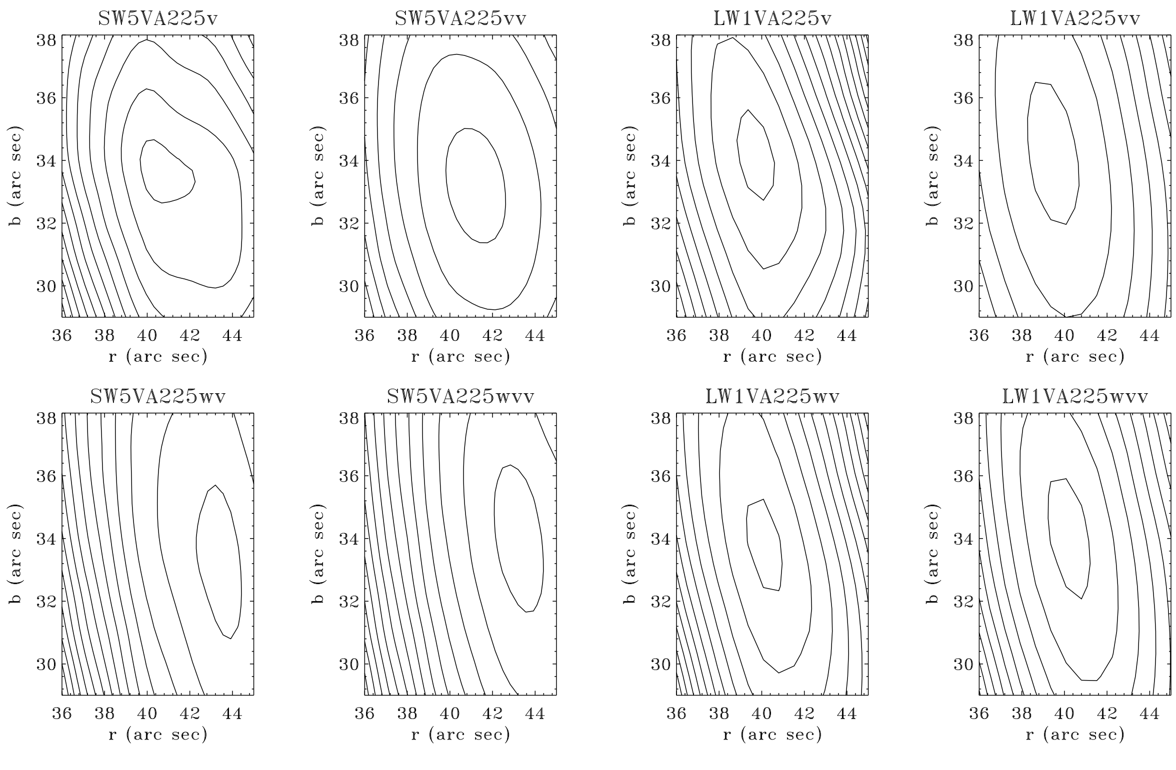

Figure 4.8: *Contours of the goodness-of-fit measures for SW5 and LW1.*

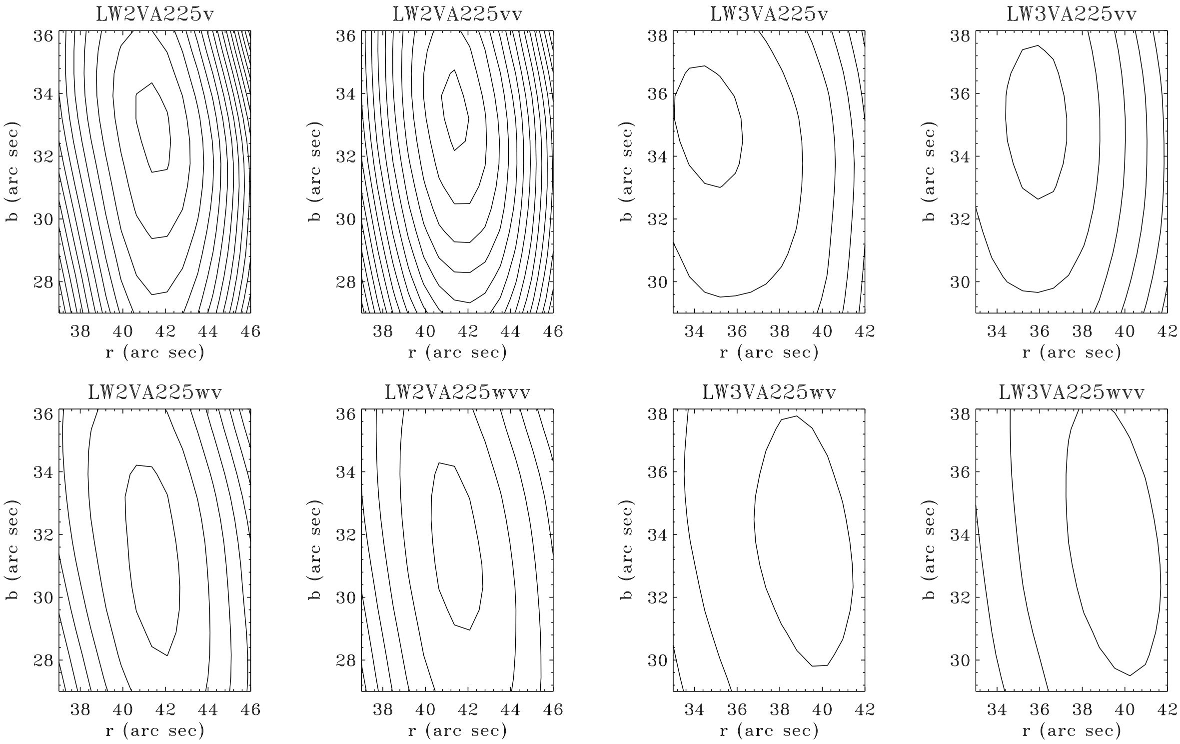

Figure 4.9: *Contours of the goodness-of-fit measures for LW2 and LW3.*

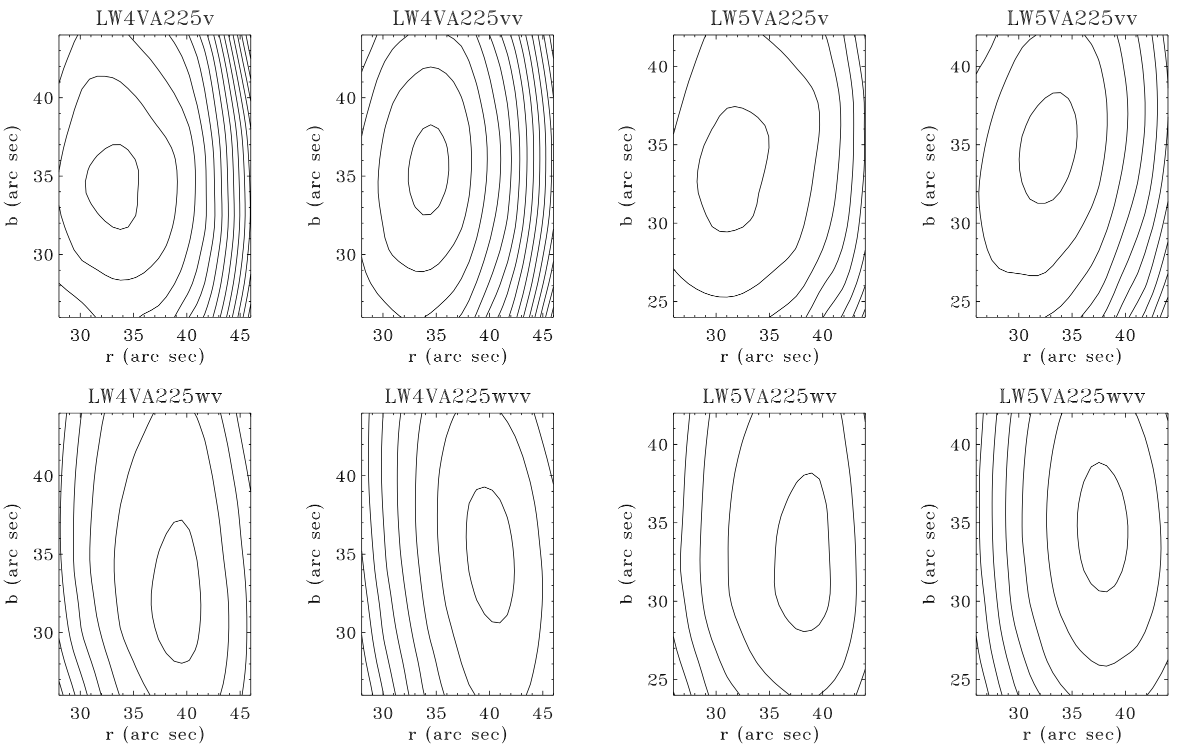

Figure 4.10: *Contours of the goodness-of-fit measures for LW4 and LW5.*

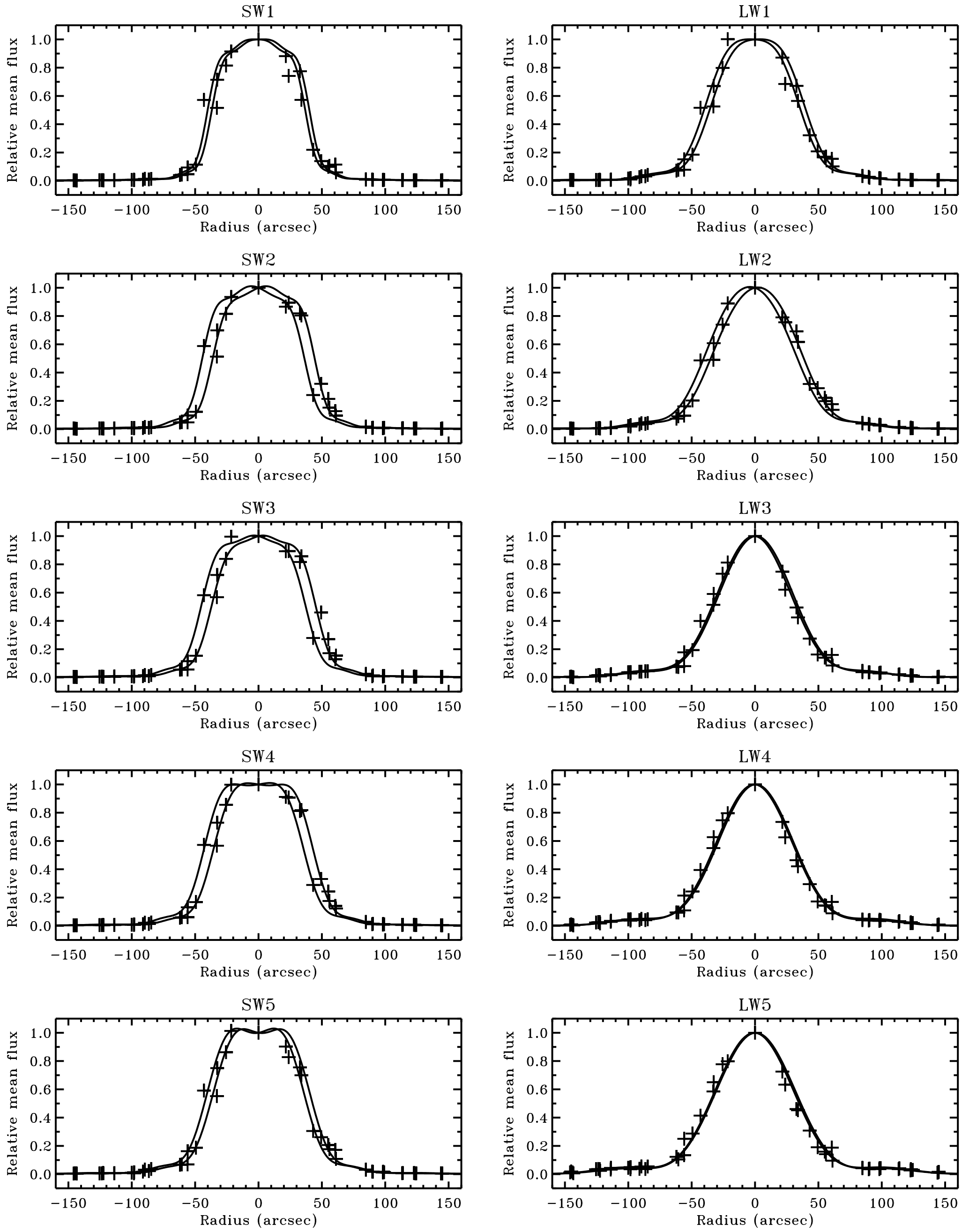

Figure 4.11: *The mean beam profiles for each detector. The observed relative mean flux at each offset position is plotted against radius, with the sign taken from the RA offset in Figure 4.2. The lines on each plot show the calculated profile in the spacecraft Y and Z co-ordinates.*

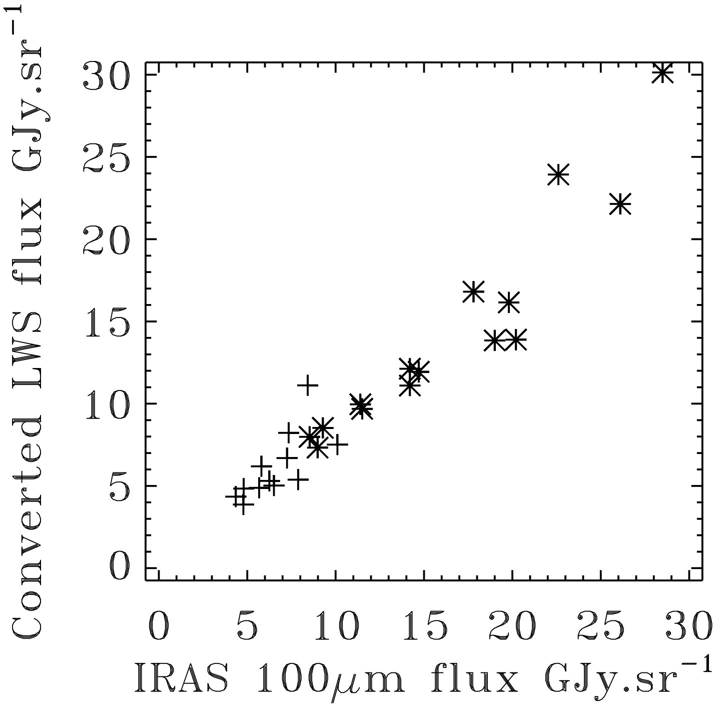

Figure 4.12: *Comparison of converted LWS and IRAS 100 mum extended source fluxes in the Trumpler 14 (+) and 16 (*) fields.*

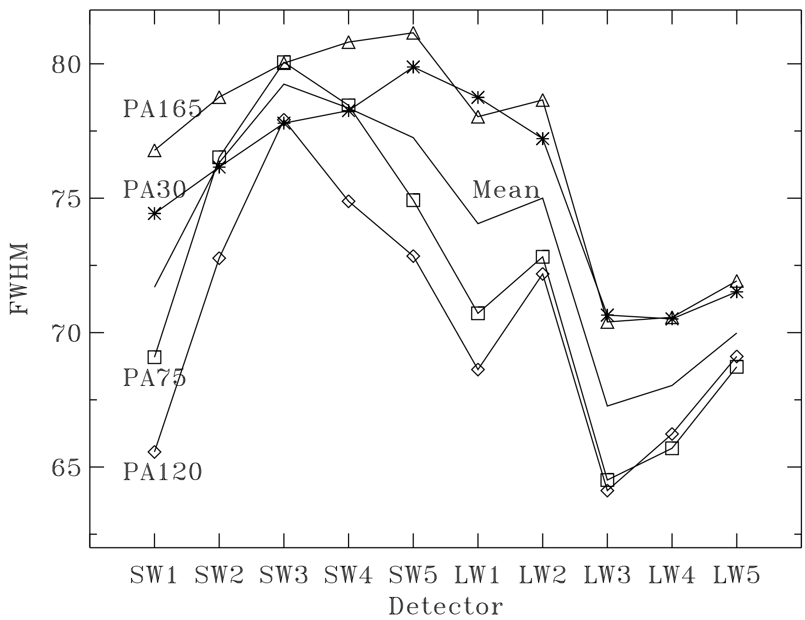

Figure 4.13: *FWHM vs. detector for the four alignments.*

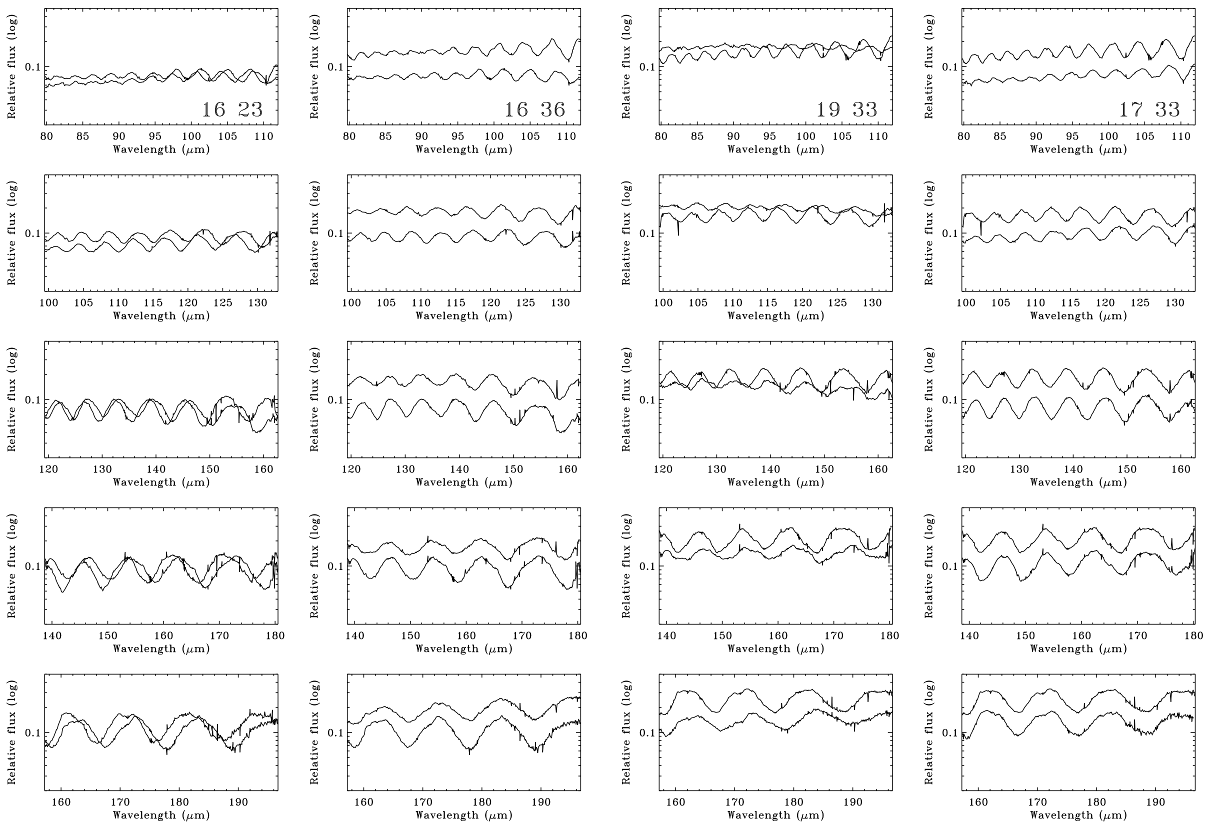

Figure 4.14: *(a) Opposite and orthogonal pairs on PA30 and PA120 at 61″ (left) and (b) opposite and orthogonal pairs on PA30 and PA120 at 61″ (right).*

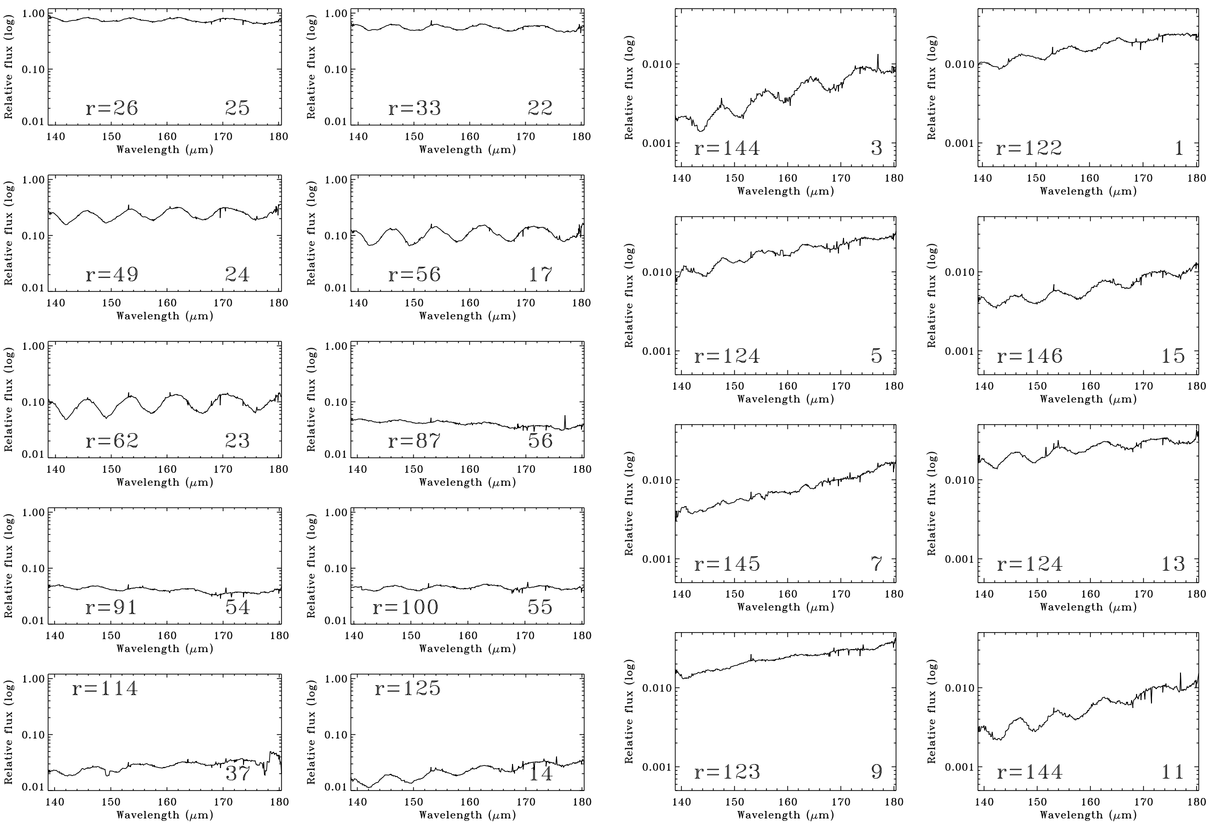

Figure 4.15: *(a) Radial progression of the fringe amplitude in LW4 (left) and (b) the variation in fringe amplitude at alternate positions on outer edge (right).*

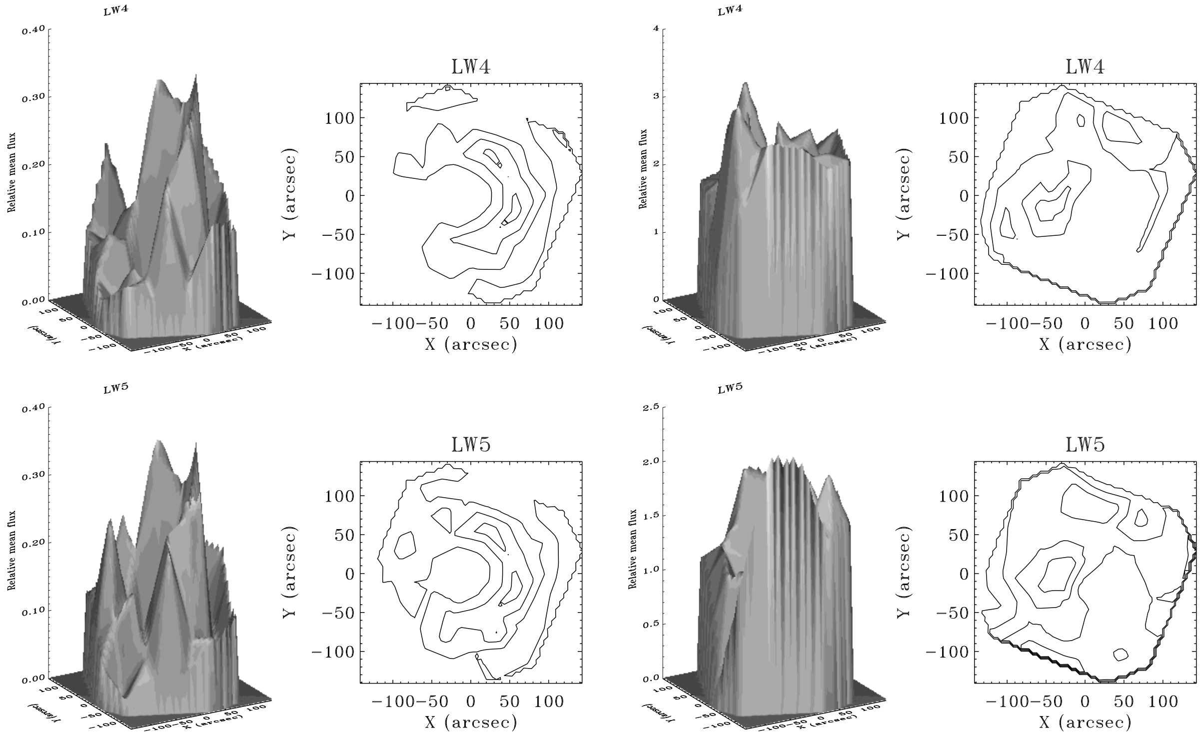

Figure 4.16: *(a) Relative fringe amplitude for LW4 and LW5 which show the largest fringing. The amplitude of the fringes rises to a maximum in a broken ring at a radius of $\sim 50''$ and then falls off towards the edge of the field. The co-ordinates are the same as in Figure 4.2. (b) Fringe phasing for LW4 and LW5 which is relatively constant on the right hand side of the field.*

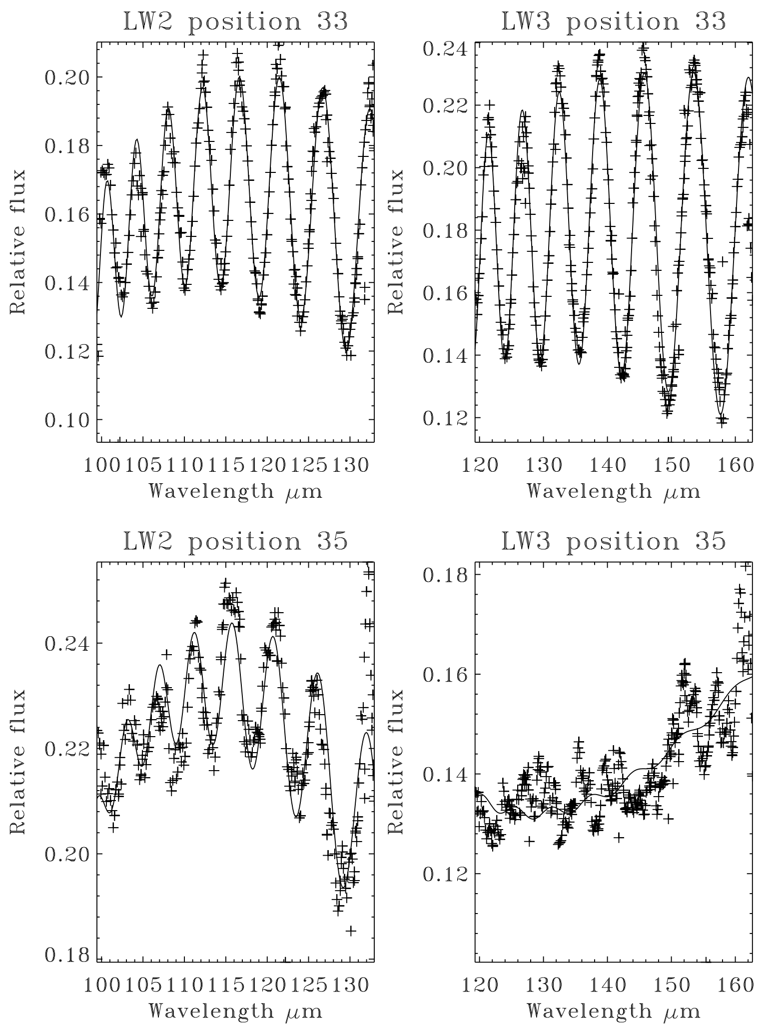

Figure 4.17: *Fringe fitting for LW2 and LW3 at positions 33 and 35.*

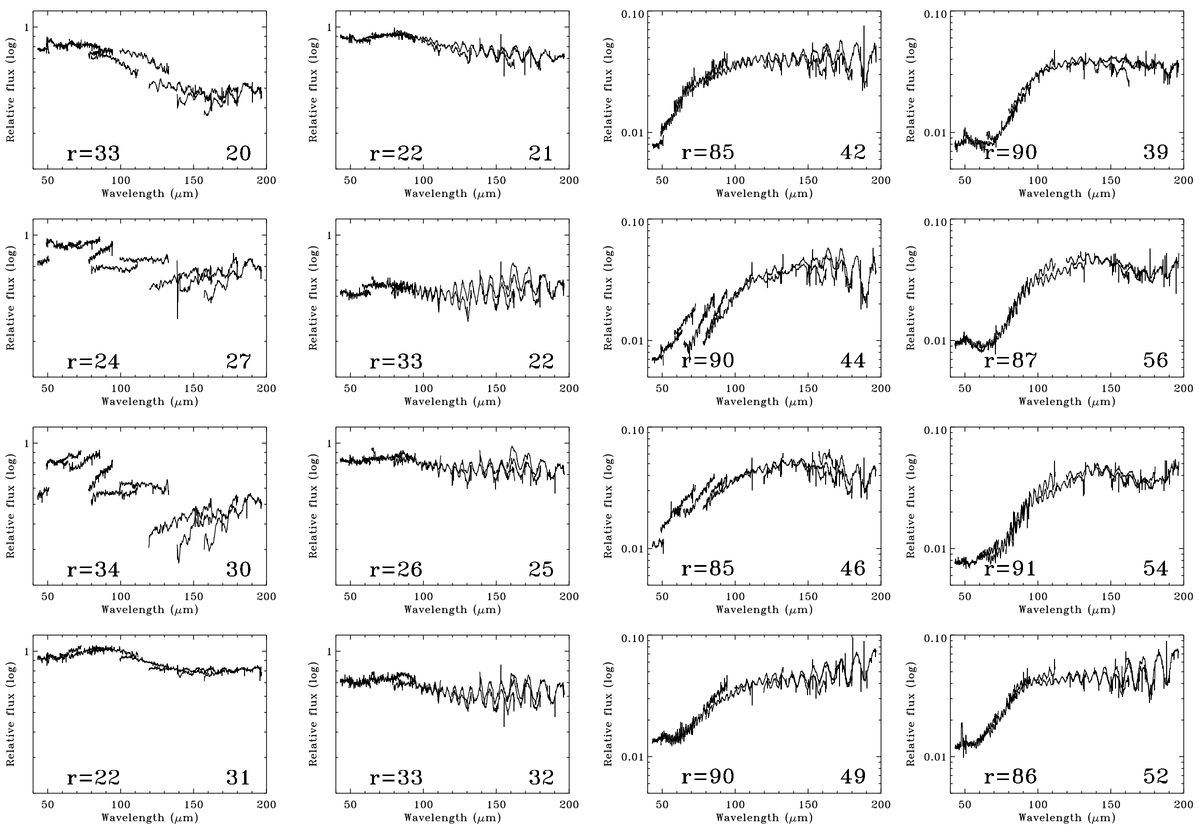

Figure 4.18: *Spectra at radius of ∼ 25″ (left) and 90″ (right) at various offset positions corresponding to those in Figure 4.2. The fracturing of the spectra can be seen on one side of the field, and the effects of fringing at longer wavelengths.*

Chapter 5

ISOPHOT Beam Profiles

The determination of its Beam Profiles is an important cornerstone of the calibration of the ISOPHOT instrument. Considerable effort has been put into the interpretation of the relevant data. Due to the multitude of instrument configurations and the limited calibration time in orbit, useful calibration data is only available for a subset of all configurations, so that additional theoretical modeling was needed. This work reviews our present knowledge about the Beam Profiles of all three subinstruments, P, C and S, resulting in corrections to the photomety of point sources and the calibration of fluxes of extended sources. Further associated topics like straylight, map reconstruction and simulation are covered as well.

5.1 Introduction

For ISOPHOT diffraction plays an important role, given the fact that at the longest wavelengths around 200 μm the Airy Disk fills the entire $3'$ aperture of the instrument. The understanding of how a point source is projected into the focal plane of the instrument is fundamental to the interpretation of photometric measurements and the construction of images. The energy distribution of a single point source produced by the telescope optics in the focus we will call in the following the Point Spread Function (PSF). The diameter of the Airy Disk characterizes its size very well. For the ISO telescope its diameter is given by $d_{Airy} = 0.839 \times \lambda$ in $['']$ projected on the sky, or by $d_{Airy} = 0.0366 \times \lambda$ in units of mm in the focal plane. The wavelength λ is always in units of μm.

Unlike in standard astronomical CCD cameras, the pixelsize of the ISOPHOT detectors is most of the time larger than the Airy Disk. The measured signal obtained from a point source generally depends on its relative position w.r.t. the pixel centre, but even a point source outside the geometric boundaries of the aperture still generates a signal, often called straylight. The convolution of the ISO PSF and the transfer function of the detector aperture yields the beam profile. In contrast to the PSF, the beam profile is directly measured when scanning the detector aperture with a point source on the sky. It incorporates the telescope specific features of the PSF but also the features originating from the optical path within the instrument. If the aperture becomes considerably smaller than the Airy Disk, the shape of beam profile and PSF become equal. Sometimes the Beam-Profile is also referred to as footprint.

For ISOPHOT there is a range of applications. The main ones are:

1. correction of point source photometry for mispointing

2. extended source calibration

3. reconstruction of maps
4. map simulation
5. superresolution

This document will treat the first four points, while superresolution has not yet been tried in any greater detail and would require a dedicated effort. The second chapter gives an overview of the instrumental configurations, which principally lead to different Beam Profiles. The third chapter gives some theoretical background, defines the terms Point Spread Function and Beam-Profile in the PHT context and describes the modeling with emphasis on the peculiarities of the ISOPHOT subinstruments P, C and S. The third and fourth chapter will then describe the impact of the beam profile on the two extremes of photometry: point sources on one side and extended sources on the other.

5.2 Instrument Configurations

The ISOPHOT instrument allows for a large number of optical configurations. Although it is given elsewhere, we make a brief summary here.

The spectrometer subsection is in terms of configurations still the simplest. It has 128 detector elements, that are contemporaneously illuminated through the same aperture and require no optical reconfiguration.

The C-detectors already offer a choice among 6 filters for C100 and 5 filters for C200. With respect to the calibration of beam profiles, the detector pixels have to be regarded separately, although one can make use of some symmetries to limit the number of configurations. The C200 array comprises 4 individual detector elements and C100 comprises 9, making a total of $54 + 20$ configurations to consider.

Finally the aperture photometer P includes 11 circular and two rectangular apertures, that can be combined with 14 broad band filters. Not all combinations are practically useful, in particular the ones where the aperture is very small and the wavelength is very long, however, even when discarding these 37 combinations, there remains still a total of 145.

There was not enough time during the mission to empirically measure the beam profiles of all of these combinations. Therefore considerable effort was put into the theoretical modelling of the expected flux distribution in the focal plane.

5.3 Theoretical Models

The essential ingredients to a mathematical model of an instrumental beam profile are the point spread function of the telescope and the optical characteristics of the instrument.

5.3.1 The Point Spread Function

For our numerical calculations we initially approximated the PSF by a simple analytical telescope model, which takes into account the primary and the secondary-mirror [2]. We used

$$PSF(v,\lambda) = \frac{\pi A}{\lambda^2 f^2} F_\lambda \frac{(\epsilon J_1(\epsilon v) - J_1(v))^2}{v^2},\ v = \frac{\pi\, r}{\lambda\, f}, \tag{5.1}$$

where A is the unobscured telescope aperture, $f = 15$ stands for the f-ratio of the ISO telescope, r is the radial distance from the centre of the PSF in the focal plane, $\epsilon = 0.3$ describes the obscuration by the secondary mirror and J_1 is the first order Bessel function of the first kind.

Meanwhile a more accurate numerical model has been developed by [19] which is being used since 1998. It incorporates the complete obscuration by the secondary mirror and the tripod, as well as the shift due to the off-axis position of the instrument. First a quasi punctate source of size 1 is transformed into Fourier space. There the result is multiplied by an image of the telescope aperture, including the central obscurations of secondary and supporting tripod. The PSF is found by transforming the product back into the image plane. Finally the integral of the PSF is normalized to one, dividing by its integral over the entire focal plane.

5.3.2 The Beam Profile

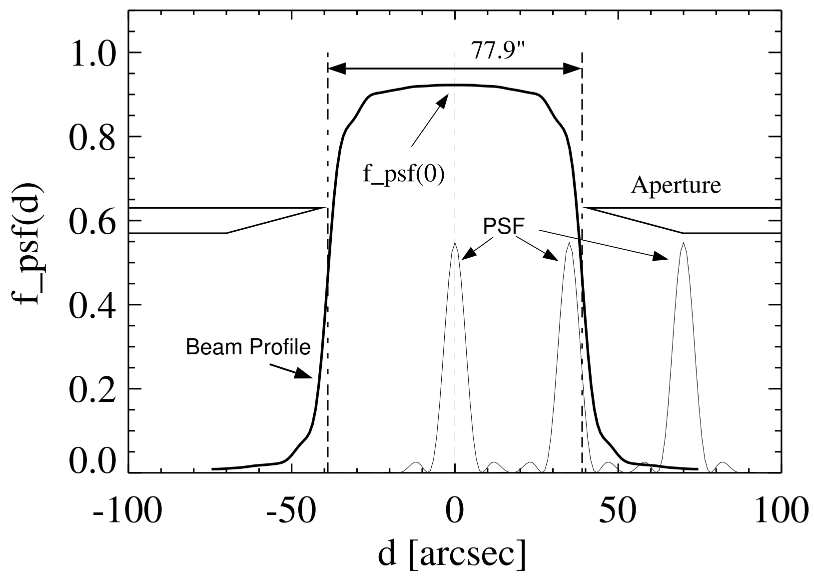

Figure 5.1: *The beam profile is the f_{PSF} factor depending on the distance d from the centre of the 79″ aperture. The relevant Point Spread Function for 20 µm is plotted at three positions (thin solid line). The convolution with the rectangular instrumental transfer function results in the beam profile shown as thick solid line.*

The beam profile is a function defined in the focal plane, that gives, depending on the positon of the illuminating point source relative to the detector aperture centre, the fraction of the total flux, that is still falling into the detector. It is measured by performing a narrowly spaced raster map on a point source, covering also ample space outside the boundaries of the aperture. Theoretically it is calculated as a convolution of the PSF with an instrumental transfer function, that is 1 within the aperture and zero outside. The integration goes over both coordinates of the focal plane. With increasing wavelength the PSF becomes wider and accordingly the beam profile 'leaks' out, i.e. more and more flux is detected originating from point source positions outside the geometrical aperture boundaries.

For the calculations standard design parameters were used. The field lenses of 1.9×1.9 mm (43.548″) for C100 and 3.9×3.9 mm (89.388″) for C200 are adopted as detector entrance apertures. Inbetween the pixels there are gaps of 0.1 mm (2.3″). Given the dimensions of the Airy disk at the nominal wavelengths of 42″ to 88″ for C100 and 101″ to 168″ for C200, the PSF is just matching the pixel size, so it is not expected to see a flat plateau on top of a beam profile, as it would be the case for shorter wavelengths.

The dimensions of the circular apertures of PHT-P are given in Table 5.1. They were measured optically before launch. Note that at this occasion also slight off centre positions from the optical axis were detected, however not exceeding 0.117 mm ≡ 2.7″.

apert. name	actual diameter		actual area	
[″]	[mm]	[″]	[mm^2]	[″^{2}]
5	0.200	4.6	0.0314	16.62
7.6	0.357	8.2	0.1001	52.81
10	0.470	10.8	0.1735	91.61
13.8	0.600	13.8	0.2827	149.6
18	0.820	18.8	0.5281	277.6
23	1.000	22.9	0.7854	411.9
52	2.300	52.7	4.155	2181
79	3.40	77.9	9.079	4766
99	4.30	98.6	14.52	7636
120	5.20	119.2	21.24	11159
180	7.85	179.9	48.40	25419

Table 5.1: *Actual dimensions of the circular apertures of ISOPHOT-P.*

For PHT-S the nominal 24″ × 24″ rectangular aperture is used for the calculations.

For the theoretical calculation of beam profiles, the broad-band filters of ISOPHOT in principle require also an integration over wavelength, including the spectral profiles of filters and source. Although test calculations showed that there are only small deviations for typical configurations and sources (e.g. 2 % for P_11.5 and 52″ aperture), it was found that the results for PSF factors depended more on the choice of the reference wavelength in the monochromatic calculation, than if the entire bandpass was integrated.

Therefore theoretical calculations of the PSF-factors at the centres of apertures (Sect. 5.4.1) were performed including the integration over the bandpass of the filters and assuming a $\nu F\nu =$ *const.* spectum, while calculations of entire Beam-Profiles were done monochromatic at the filter reference wavelength λ_{ref} due to the otherwise excessive computation times.

5.4 Point source photometry

The photometric calibration of ISOPHOT is based on known celestial point sources, that were used to calibrate the internal Fine Calibration Sources (FCS) [25]. For observations of unknown sources, the FCS is used as reference to determine the variable responsivity of the detector at the time of a measurement.

To calculate the power that is inducing the photo current within the detector, we use

$$\Phi_{src} = A\, f_{PSF_{f,a}}\, T_{refl.} \int [T_f(\lambda)\; R_p(\lambda)\; F_\lambda(\lambda)]\, d\lambda. \tag{5.2}$$

The SED of the source is given by F_λ, $T_f(\lambda)$ denotes the product of all spectral transmissions of filters and field lenses in the beam and $R_p(\lambda)$ is the spectral detector response, normalized to its peak. The integration is performed over all wavelengths. A is the area of the telescope aperture, while wavelength independent losses due to mirrors are accounted for by the factor $T_{refl.}$. The indices p and f indicate dependence on pixel or filter respectively.

5.4.1 PSF factors

Since we measure point sources, the PSF correction factor $f_{PSF_{f,a}}$ is needed to describe – for a given combination of filter f and aperture a – the fraction of the PSF that actually enters the detector aperture. It is calculated as the ratio of the PSF integrated over the area of the detector aperture, and the PSF integrated over an infinite plane. It is effectively the value at the centre $\vec{d} = \vec{0}$ of the beam profile function defined earlier.

5.4.2 Peculiarities of PSF factors

The PSF factors that are published in the Observer's Manual for ISOPHOT were still calculated using the analytical PSF model described above. Although the filter width does not make a tremendous impact, we note that also in this case the PSF was calculated accounting for the spectral shapes of filter and detector response.

The newer PSF model yields slightly different values, due to the now included tripod. Since it is foreseen to use these consistently in the OLP 10 versions of Cal-G files, we give only these new ones in Table 5.2. For the point source calibration this is not a problem, since constants in Eq. 5.2 drop out in the FCS calibration. The result depends only on the ratios of detector signals and fluxes. This holds as long as the same constants are used in the calibration of the FCS against standard stars and the observation of unknown point sources. More attention must be paid to this peculiarity when transferring to extended source calibration, which will be treated later.

PHT-P PSF Correction Factors (broad band)

							PHT-P apertures						
λ	$5''$	$7.6''$	$10''$	$13.8''$	$18''$	$23''$	$20{\times}32''$	$52''$	$79''$	$99''$	$120''$	$127{\times}127''$	$180''$
P1													
3.29	0.85	0.88	0.91	0.92	0.95	**0.96**	0.96	0.99	0.99	0.99	1.00	1.00	1.00
3.6	0.81	0.88	0.91	0.92	0.94	**0.95**	0.96	0.98	0.99	0.99	1.00	1.00	1.00
4.8	0.69	0.86	0.88	0.90	0.92	**0.93**	0.94	0.98	0.99	0.99	0.99	0.99	1.00
7.3	0.64	0.76	0.85	0.87	0.89	**0.91**	0.92	0.96	0.97	0.98	0.99	0.99	0.99
7.7	0.64	0.73	0.85	0.87	0.88	**0.90**	0.91	0.96	0.97	0.98	0.99	0.99	0.99
10	0.54	0.66	0.73	0.84	0.87	0.88	0.89	**0.94**	0.96	0.97	0.98	0.98	0.99
11.3	0.48	0.66	0.68	0.79	0.86	0.87	0.89	**0.93**	0.96	0.97	0.97	0.98	0.99
12	0.48	0.65	0.70	0.78	0.86	0.87	0.88	**0.93**	0.95	0.97	0.97	0.98	0.99
12.8	0.42	0.65	0.66	0.73	0.86	0.87	0.88	**0.92**	0.95	0.96	0.97	0.98	0.98
15	0.33	0.61	0.66	0.67	0.80	0.86	0.85	**0.92**	0.94	0.95	0.96	0.97	0.98
P2													
20	0.22	0.47	0.59	0.65	0.69	0.75	0.79	0.89	**0.92**	0.93	0.95	0.95	0.97
25	0.17	0.41	0.54	0.63	0.66	0.70	0.76	0.88	**0.91**	0.93	0.94	0.95	0.96
P3													
60	0.04	0.09	0.15	0.23	0.36	0.46	0.51	0.68	0.81	0.86	0.87	0.88	**0.90**
100	0.01	0.04	0.05	0.09	0.15	0.22	0.27	0.59	0.66	0.70	0.77	0.83	**0.87**

Table 5.2: *PSF correction factors as calculated with the new numerical PSF model but also integrating over the instrumental spectral response, assuming a $\lambda F_\lambda = const.$ source colour. The factors represent the intensity fraction of a point source entering an aperture of PHT-P. The numbers in bold print indicate the standard aperture/filter combinations. Note that these factors will be only applicable for calibration files since OLP version 10. For earlier versions the ones in the Observer's Manual apply.*

5.4.3 Standard apertures for calibration

To manage the amount of filter/aperture combinations of PHT-P in calibrations, one standard aperture was selected for each filter. The selection was made to be as close as possible to apertures that observers were expected to select for point source photometry. Aperture diameters, that include at least 90 % of the energy in the PSF were adopted as the best compromise between the two requirements: good source signal and low background contribution. The resulting combinations are marked in bold print in Table 5.2 and were used for all measurements performed to calibrate the FCSs against celestial standards.

5.4.4 Asymmetric shapes of PHT-P Beam Profiles

In order to obtain a direct measurement of the beam profiles of the P-apertures, dedicated raster observations were carried out during PV-phase and later in the mission. Unfortunately the strong transient effects rendered many observations strongly disturbed and only of limited use. The data, as far as it could be evaluated by now, shows the theoretically expected diameters of the measured beam profiles. However, strong variations in the center regions are seen, which were supposed to be flat or at least symmetric towards the central axis. Fig. 5.2 shows reconstructed aperture profiles at 12 μm with the $52''$ and the $180''$ apertures and the $180''$ aperture at 7.3 and 16 μm [17].

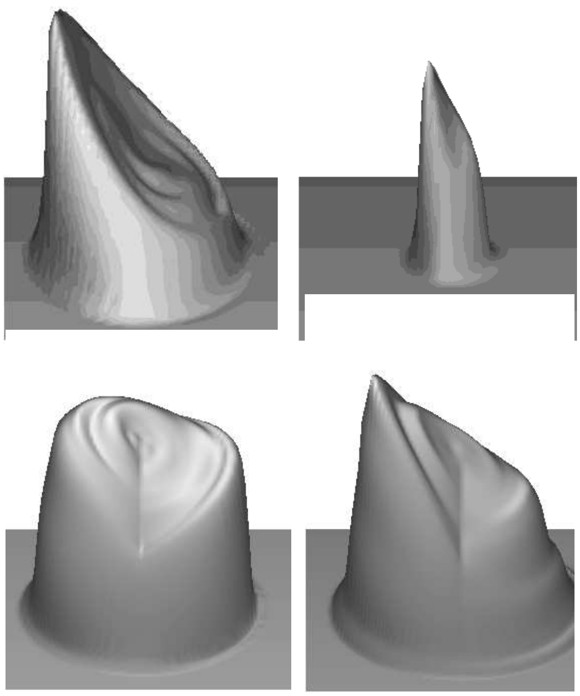

Figure 5.2: *From left to right: reconstructed aperture profiles from cross scans at 12 μm with the $180''$ and the $52''$ apertures and the $180''$ aperture at 7.3 and 16 μm.*

From the quite steep spatial sensitivity gradient that appears sometimes at the centre of the aperture, a strong dependence on pointing accuracy results. In the strongest observed case in the 12 μm filter, a shift by $8''$ produces a change by 30 %. While the ISO pointing, which was good to $\approx 2''$, should not give rise to major systematic errors in the PHT-P photometry, except for the smallest apertures up to about 10″ diameter, a thorough check of observer provided coordinates appears to be an important step in the validation of the photometry of point sources.

5.4.5 Source positioning on arrays

Standard staring AOT measurements with C-detectors place a point source right at the centres of the arrays, i.e. for C100 (3×3 pixels) at the centre of the central pixel #5 and inbetween all four pixels of the C200 (2×2 pixels) array. In the case of C200, the photometry can vary quite strongly with changes in the source position, since the source is placed on the steep shoulders of each of the beam profiles. As a consequence, the photometry for staring AOT measurements is usually done with the sum of the calibrated fluxes of the four C200 pixels, which make up a fairly flat combined beamprofile. The flux calibration was however done for each pixel individually, centring the calibrator point source over each pixel, i.e. never centring on the C200 array. Therefore a number of additional measurements were performed on the same calibrators positioned at the array centre, intended to verify the PSF correction factors of a number of typical positions of a C200 pixel w.r.t. a point source. These help not only transferring the calibration between pixel centred and array centred observations but also allow to accurately determine the background from mini-maps. The analysis of these empirical PSF factors is outlined in [11].

The positions for which the PSF factors have been determined are given in terms of distance in [″] to the centre of a reference pixel. For C100 only the factors $f_{psf}(46)$, $f_{psf}(92)$, and $f_{psf}(46\sqrt{2})$ are relevant, which are for the horizontally or vertically adjacent two pixels and the diagonally adjacent pixel respectively. For C200 the PSF factors $f_{psf}(92)$, $f_{psf}(92\sqrt{2})$ and $f_{psf}(46\sqrt{2})$ apply, which are for the vertical/horizontal neighbouring pixel centres, the diagonally adjacent pixel centre and the array centre, respectively. Fig. 5.3 illustrates the locations of positions. The measured ratios compiled from [11] are given in Tables 5.3 and 5.4. For C200 the ratio $f_{psf}(46\sqrt{2})/f_{psf}(0)$ is calculated as $f_{psf}^{array}/f_{psf}^{pixel}/4$.

filter	λ_{ref} μm	$f_{psf}(46)/f_{psf}(0)$	$f_{psf}(46\sqrt{2})/f_{psf}(0)$	$f_{psf}(92)/f_{psf}(0)$
C_50	65	0.0465 ± 0.0045	0.0077 ± 0.0012	0.0019 ± 0.0008
C_60	60	0.0375 ± 0.0030	0.0057 ± 0.0004	0.0015 ± 0.0006
C_70	80	0.0632 ± 0.0049	0.0171 ± 0.0024	0.0025 ± 0.0011
C_90	90	0.0553 ± 0.0063	0.0187 ± 0.0022	0.0014 ± 0.0010
C_100	100	0.0598 ± 0.0068	0.0292 ± 0.0030	0.0020 ± 0.0013
C_105	105	0.0699 ± 0.0080	0.0336 ± 0.0036	0.0037 ± 0.0014

Table 5.3: *Measured ratios of PSF factors in C100 for typical distances and positions that are needed for correct background determination in staring measurements and small maps.*

filter	λ_{ref} μm	$f_{psf}(92)/f_{psf}(0)$	$f_{psf}(92\sqrt{2})/f_{psf}(0)$	$f_{psf}(46\sqrt{2})/f_{psf}(0)$
C_120	120	0.0589 ± 0.0033	0.0161 ± 0.0015	0.1804 ± 0.0102
C_135	150	0.0763 ± 0.0024	0.0266 ± 0.0023	0.2151 ± 0.0109
C_160	170	0.0656 ± 0.0032	0.0298 ± 0.0027	0.2063 ± 0.0082
C_180	180	0.0946 ± 0.0042	0.0371 ± 0.0020	0.2468 ± 0.0185
C_200	200	0.0989 ± 0.0044	0.0525 ± 0.0017	0.2938 ± 0.0086

Table 5.4: *Measured ratios of PSF factors in C200 for typical distances and positions that are needed for correct background determination in staring measurements and small maps.*

These ratios were then compared to theoretical calculations using design parameters for the relative geometrical pixel positions and dimensions. The theoretical expectations turned out to be quite different from the measured values for the C200 [27] (between 25 to 50 %), while deviations for C100 are small below 5 %. By either increasing the distance between pixels by about 4″ in both arrays, or by decreasing the effective pixel size by 5.5″ or 9.4″ for C100 and C200 respectively, the modeled ratios could be made very consistent with the measured ones. An analysis of raster measurements of the beam profiles in the C_120 filter suggests larger pixel distances as the most likely explanation. However the actual case is even more complicated since in reality these deviations are not symmetric. Increases of distances between pixels have been determined by fitting model beam profiles for C_120 to the measured ones. The distances are between 0 and 12″ larger than the nominal value. This average shift is similar to the symmetric one, necessary to make model and measurement PSF-ratios agree.

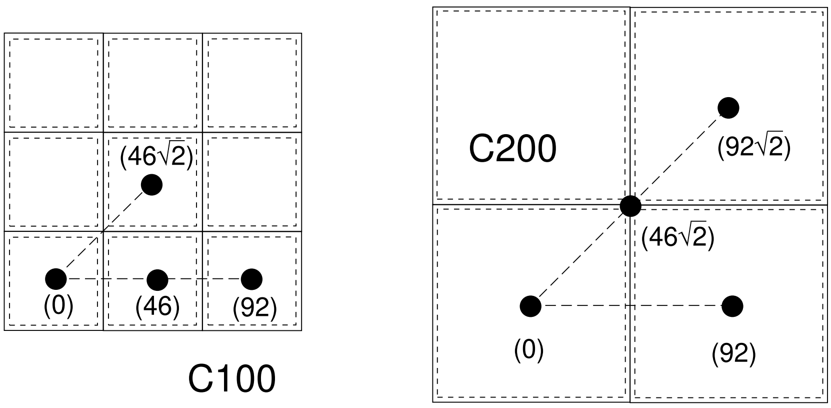

Figure 5.3: *The entrance apertures of the PHT-C arrays and the reference positions, PSF calculations have been made for. The dashed line indicates the light sensitive part of each pixel due to the 0.05 mm support around the field lens.*

The absolute PSF factors for the arrays were finally derived by combination of the PSF factors for single pixels resulting from the broad band integrated model (see Table 5.3 and 5.4) and an appropriate combination of the measured ratios. For C100 the formula $f_{psf}^{array} = f_{psf}^{pixel}(1 + 4\,f_{psf}(46)/f_{psf}(0) + 4\,f_{psf}(46\sqrt{2})/f_{psf}(0))$ was used while for C200 $f_{psf}^{array} = f_{psf}^{pixel} 4\,f_{psf}(46)/f_{psf}(0)$ was applied. Further details can be found in [27]. This way the scheme stays consistent, since it keeps the PSF factors that are used for point source calibration. Only the array centred values are adjusted to match the observations.

5.4.6 Construction of PHT-S Beam Profiles

The beam profiles of the 128 pixels of PHT-S were measured with cross scans along the spacecraft y and z coordinates over a bright point source (γ Dra). The measurement procedure was carefully avoiding to induce transients by allowing enough time for the signal to settle and by avoiding to cross the source when changing from the x to the z leg. Residual transient effects became visible by performing scans in both directions [22][10]. The scan length was $\pm 60''$ with stepsizes of 3″ inside the aperture and 5″, 10″ and 20″ outside. In dispersion direction (z-axis) the beam profile is fairly rectangular as expected, while in cross dispersion direction (y-axis) the profile is very sharp, with the peak generally deviating from the geometrical centre of the aperture.

PSF Correction Factors

filter	pixel centred	array centred
C_50	0.656	0.799
C_60	0.667	0.782
C_70	0.629	0.831
C_90	0.586	0.759
C_100	0.558	0.757
C_105	0.540	0.764
C_120	0.678	0.489
C_135	0.641	0.552
C_160	0.620	0.512
C_180	0.609	0.601
C_200	0.568	0.667

Table 5.5: *Pixel centred and array centred PSF correction factors. The pixel centred factors are calculated from the theoretical model using standard design parameters for detector dimensions. A $\nu F_\nu = const.$ source colour has been assumed. From these the array centred PSF factors were then derived using the measured ratios $f_{psf}^{array}/f_{psf}^{pixel}$.*

The deviation is suspected to come from a misalignment of the dispersion direction and the orientation of the linear detector array within the instrument. The comparison with ground based laboratory measurements shows very similar profiles (see Fig. 5.4). Note that the breaks seen in the middle of each detector array, i.e. between pixels 32-33 and 96-97 are due to the change of order sorting filters at this position, which are mounted in front of the detector arrays.

The data was re-analyzed later by [6] and [1]. Two methods to reconstruct the full 2 dimensional beam profiles from the two cross scans were discussed. The following method was finally adopted: $BP(y,z) = Scan_y(y)Scan_z(z)$, where $Scan_y$ and $Scan_z$ are the fluxes derived from the cross scans along the y and z-axis respectively, normalized to their peak.

5.4.7 Pointing dependent corrections with PHT-S

Due to the relatively sharp beam profiles, especially in cross-dispersion direction (y-axis), for point source observations, small deviations from the nominal centre position result in considerable signal changes. The calibration is made for the central position of the PHT-S aperture, which often isn't where the maximum of the beam profile is located. A mispointing often can be identified by the sharp breaks at the edges of the order sorting filters and between the SS and the SL arrays in an otherwise smooth spectrum.

From the PHT-S cross scans on γ Dra mentioned above and the resulting 2-dimensional beam profile, a 3-dimensional matrix was derived [1]. Depending on the offset w.r.t. the nominal centre position of the PHT-S aperture in spacecraft coordinates y and z and the pixel number (wavelength), the matrix provides a correction factor for point source fluxes. Possible offsets in y and z coordinates run between $\pm 10''$. The matrix contains discrete values in steps of $2''$. The method has been implemented in PIA, however was not incorporated into pipeline processing (OLP). This was for two reasons: i) in a statistical assessment only 5 % of the offsets calculated as the difference between commanded and achieved pointing were above ISO's pointing accuracy of $2''$ and within $\pm 10''$ ([20]). ii) The difference between commanded and achieved pointing, which is the only parameter easily available to an automatic offset correction, is not a very good one, since the intended pointing provided by the observer may contain inaccuracies already at this stage. The correction factors for various offsets spaced in $3''$ steps are illustrated in Fig. 5.5.

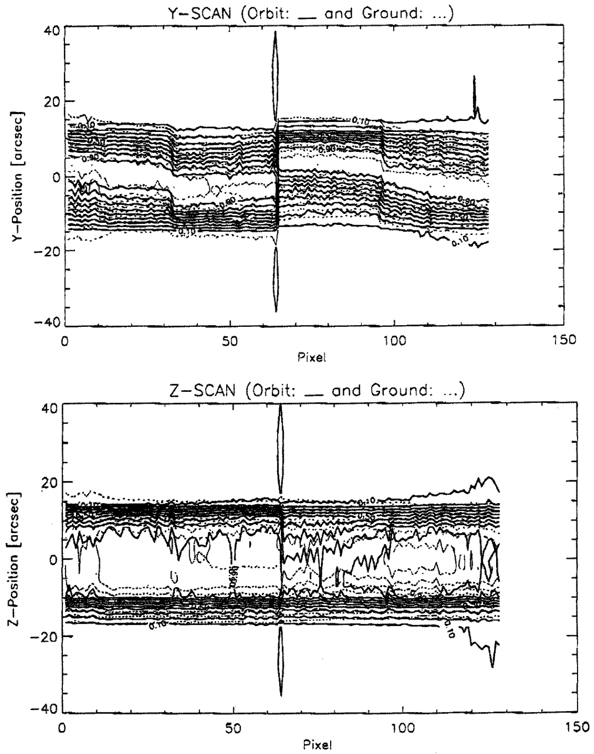

Figure 5.4: *Cross scan profiles in y and z direction for all pixels. Solid line contours were measured in orbit, dotted line contours stem from ground calibrations.*

5.4.8 Straylight verification

For any absolute photometry of the celestial background, straylight contributions from other bright sources should be minimal and must be known. The brightest infrared sources on the ISO sky were the Sun, the Earth, the Moon and Jupiter. Their constellation induced certain pointing restrictions and constraints. Under these limitations, the maximum contribution by these sources in the focal plane according to [16] was to be less than 10 % of the minimum natural sky background brightness for the entire wavelength range from 2.5 to 240 μm. This straylight requirement includes the contributions of all three sources, i) the theoretical beam profile, ii) the "true" straylight reflected off baffles, telescope struts etc. and iii) the thermal radiation of the telescope structure which could become detectable at the longest wavelengths.

For the verification near-field straylight within 1° radius was distinguished from far-field straylight. To determine the near-field contribution, measurements with ISOPHOT in three different channels were made, with PHT-S at 2.5-12 μm, with PHT-P at 25 μm and with PHT-C at 170 mum [9][15].

With PHT-S, measurements performed at a distance of 60″ from the bright souce γ-Dra (1600-100 Jy) resulted only in a signal consistent with dark current. The measurements were made before the above mentioned beam-profile cross scans, to suppress long-term transients. In the P_25 filter double cross scans over Mira (1500 Jy) were performed out to radial distances of 30′. At these distances no additional contribution from the beam profile of the bright source on top of the relatively bright zodiacal light background could be detected. With the C_160 filter, double cross scans were performed around Saturn (32000 Jy). Crossing the source was avoided to prevent memory effects and saturation of the detector. The maximum radial distance was 45′. The radial fall-off of the signals was close to the predictions by a theoretical study of Breault

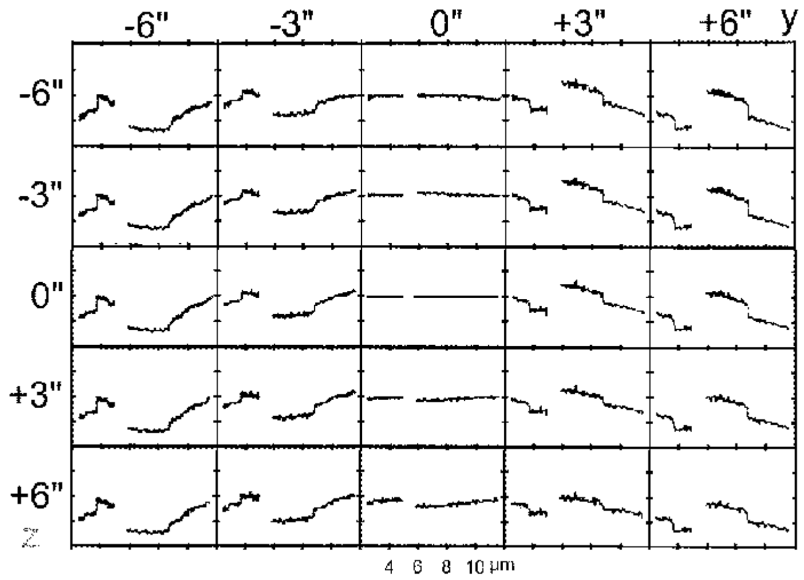

Figure 5.5: *PHT-S offset correction factors. Each diagram shows the correction factors for the 128 pixels at a different offset location in steps of 3″. Each diagram has a vertical range from 0 to 2.*

Research [21], confirming their conservative assumptions about reflectance of the black paint and contaminations. According to the study, most of the straylight level comes from the tripod support of the secondary mirror, the secondary edge and the secondary mirror surface [9].

The far-field straylight from Moon and Sun was measured during the eclipses that occurred due to the extended lifetime of the satellite. Both measurements were executed pointing at a fixed sky position. For the Sun straylight measurement the source was 60° away, i.e. at the minimum avoidance angle. For the expected drop and rise at the entry and exit of the eclipse phase, an upper limit of 70 mJy at 25 μm and 113 mJy at 170 μm was derived [9]. In a refined analysis [15] 0.016 MJy/sr and 0.010 MJy/sr are quoted at 25 μm and 170 μm. Using the standard conversion of PIA 9.1, this translates back into 9 mJy and 19 mJy respectively for a 180″ aperture or the sum of the 4 C200 pixels.

A sequence of 3 successive eclipses were used to assess the Moon straylight. Again ISO was pointing at a fixed position on the sky, while data was taken alternatingly with P2 and C200. At the three occasions the Moon was located at distances of 62°, 49° and 28°. Thus the measurement series was set up to detect relative differences in the background levels, however worked in an "absolute" measurement mode since all systematic uncertainties of the flux calibration and its reproducibility over longer time periods apply. Again the variation was below the detection limit and upper limits of 120 mJy at 25 μm and 50 mJy at 170 μm were determined by [9], while [15] quotes 0.179 MJy/sr and 0.046 MJy/sr, which translate into 100 mJy and 86 mJy.

The measurement of straylight contributions by the Earth required special constellations of Earth and Sun. The Earth was positioned at 3 directions relative to the oblique conical sunshade, keeping the limb at the minimum allowed angle from the ISO sky pointing. The observations were designed to detect differences in the measured background level, depending on the grade of the Earth shining into the sunshade. In [9] no quantitative results could be presented yet, however a significant contribution at 170 μm was already excluded. In [15] 0.26 MJy/sr and 0.18 MJy/sr are given for the 25 μm and 170 μm filters, which translate into 101 mJy and 526 mJy.

An unexpected result came from the Serendipity Survey, which was also carried out at 170 μm. A composition of all slews relative to Saturn was produced after the mission. It shows an elliptical ring emission at a radial distance of 0.7° to 1.0° with Saturn at its centre. The brightness of the ring is given as ≈1 % of the central source [15] and is tentatively assigned to grazing reflections at the oversized secondary mirror cover.

5.5 Extended source photometry

Due to the primary calibrators of PHT being point sources, the calibration of extended sources must be performed indirectly. To express fluxes in terms of surface brightness (MJy/sr), the effective solid angle Ω of the detector pixel must be known. Then the conversion from point source flux F_ν to surface brightness I_ν is done according to:

$$I_\nu = \frac{F_\nu \, f_{psf}}{\Omega}. \tag{5.3}$$

Earlier versions of the ISOPHOT Handbook [13] still include a term $(1-\epsilon^2) = 0.91$ with $\epsilon = 0.3$ in the conversion formula from point source flux to extended source flux. As was shown in [28] and [12], this term should not be there and is most likely a remnant from a different normalization in the analytical PSF model of [2]. OLP 10 still uses this factor, which increases all extended flux results by 9 %.

5.5.1 Theoretical solid angles

Surface brightness can be interpreted as emission from a large number of point sources with very small space among ach other. Strictly it is only defined for homogeneous sources of infinite extent. Thus the effective solid angle $\Omega(\lambda, A)$ can be calculated as the beam profile $f_{psf}(\vec{d}, \lambda)$ integrated over the entire sky, i.e. the integral over the PSF correction factor as a function of the offset position $\vec{d}$ from the aperture centre and wavelength λ:

$$\Omega(\lambda, A) = \int^{\infty} f_{psf}(\vec{d}, \lambda) \, d\vec{d}. \tag{5.4}$$

5.5.2 Solid angles for PHT-P

The beam profiles were integrated as arrays of 61 × 61 elements with field sizes of 50″ for all apertures below 23″ diameter and 240″ for the bigger ones. Some systematic errors may still be there, however given the already considerable qualitative differences found between measured and theoretical beam profiles (see Sect. 5.4.4), a larger effort seemed not to be justified. To keep computation times to a reasonable level, all results are calculated only for the monochromatic case.

The results for PHT-P solid angles as calculated by [27] are given in Table 5.6, which are most similar to the geometrical ones.

An issue that was not resolved in OLP 10, is the correct normalization of the beam profile [27]. The way we defined it in Sect. 5.3, it has at the centre of the aperture the value of the PSF-factor. The values for the solid angles in OLP 10 were calculated by re-normalizing the beam profiles to 1 at the centre [4], [5]. This results in solid angles, that are by $1/f_{psf}$ larger than the ones

PHT-P solid angles [10^{-7} sterad]

							PHT-P apertures						
λ	$5''$	$7.6''$	$10''$	$13.8''$	$18''$	$23''$	$20\times32''$	$52''$	$79''$	$99''$	$120''$	$127\times127''$	$180''$
P1													
3.29	0.0039	0.0124	0.0210	0.0344	0.0641	**0.0958**	0.1373	0.5125	1.1114	1.7933	2.6260	3.7295	5.9692
3.6	0.0039	0.0122	0.0210	0.0346	0.0641	**0.0955**	0.1361	0.5114	1.1119	1.7936	2.6261	3.7292	5.9704
4.8	0.0038	0.0120	0.0211	0.0342	0.0642	**0.0947**	0.1358	0.5132	1.1156	1.7935	2.6279	3.7636	5.9669
7.3	0.0040	0.0121	0.0206	0.0333	0.0626	**0.0927**	0.1322	0.5128	1.1188	1.7961	2.6232	3.7408	5.9557
7.7	0.0036	0.0118	0.0204	0.0335	0.0620	**0.0930**	0.1331	0.5120	1.1213	1.7958	2.6223	3.7063	5.9531
10	0.0035	0.0124	0.0198	0.0338	0.0612	0.0900	0.1287	**0.5124**	1.1216	1.7937	2.6132	3.7394	5.9334
11.3	0.0044	0.0108	0.0201	0.0322	0.0605	0.0908	0.1317	**0.5138**	1.1170	1.7852	2.6101	3.7232	5.9184
12	0.0037	0.0121	0.0205	0.0318	0.0594	0.0908	0.1248	**0.5136**	1.1182	1.7862	2.6071	3.6934	5.9159
12.8	0.0032	0.0119	0.0200	0.0319	0.0592	0.0895	0.1246	**0.5107**	1.1154	1.7851	2.6017	3.7295	5.9111
15	0.0043	0.0114	0.0186	0.0318	0.0632	0.0912	0.1279	**0.5078**	1.1111	1.7662	2.5926	3.7028	5.8846
P2													
20	0.0031	0.0131	0.0199	0.0323	0.0601	0.0848	0.1218	0.5096	**1.0946**	1.7637	2.5621	3.6138	5.8151
25	0.0038	0.0114	0.0199	0.0304	0.0579	0.0842	0.1263	0.5076	**1.0926**	1.7446	2.5439	3.6551	5.7880
P3													
60	0.0043	0.0172	0.0172	0.0215	0.0518	0.0692	0.1029	0.4638	1.0249	1.6943	2.4302	3.3163	**5.4348**
100	0.0105	0.0105	0.0105	0.0404	0.0404	0.0496	0.0757	0.4943	1.0640	1.5572	2.2801	3.4542	**5.2708**

Table 5.6: *The solid angles of the PHT-P subinstrument calculated as the integral over the beam profile of the respective aperture at the filter reference wavelength.*

given above. This has an impact for cases where f_{psf} is significantly smaller than 1, i.e. long wavelengths (PHT-C) and small PHT-P apertures. For ISOPHOT the PHT-C impact is most important, since extended sources were measured with PHT-P generally with large apertures.

The arguments for using the smaller solid angles given here are: i) The smaller solid angles are very similar to the geometrical ones. ii) The larger solid angles from re-normalized beam profiles ([4], [5]) tend to increase with wavelength without a compensation for the corresponding decrease in collected flux.

If the re-normalization of the beam profiles to 1 would be correct, the following formula would have to be used with the solid angles as tabulated here, i.e. to be compatible with the present OLP 10.

$$I_\nu = \frac{F_\nu\, f_{psf}^2}{\Omega}. \tag{5.5}$$

Use of Eq. 5.3 instead increases results for extended source fluxes by f_{psf} w.r.t. present OLP 10.

5.5.3 Measured relative solid angles with PHT-P

As already mentioned above, the beam profiles of PHT-P are qualitatively quite different from the ideal case. To investigate this further, a number of multi aperture measurements on positions with quasi uniform background, i.e. a strong zodiacal light or cirrus region without prominent point sources, were analyzed. The measurements actually used are tabulated in [17]. In the ideal case and for a perfect homogeneous sky background, we would expect the ratio flux/aperture area to remain constant. After application of all corrections, including the signal linearisation [26] the signal should be proportional to the flux, so the actually measured ratio signal/aperture normalized to the 180″ aperture can be considered directly, which is shown in Table 5.7.

The ratio is not 1.0 everywhere as would be expected, but drops by up to 68 % relative to the 180″ aperture, while for P_60 it rises by up to 33 %. Several sequences were measured at different sky positions, to exclude the possibility of contamination by an unknown point source.

The measured ratios could help to calibrate extended source measurements using "default" responsivities, which were mostly performed in the 180″ aperture. At least for the P1 and P2 detectors, which show only moderate responsivity changes along the orbit, this should already give useful results. The potentially more accurate method of using the FCS calibration with

Relative Effective Solid Angle Correction

filter	23″	52″	79″	99″	120″	180″
P_7.3	0.35	0.50	0.68	0.75	0.85	1.00
P_11.5	–	0.56	0.80	0.81	0.83	1.00
P_16.0	–	0.42	0.50	0.56	0.68	1.00
P_20	0.75	0.77	0.80	0.83	0.86	1.00
P_25	0.80	0.90	0.95	0.93	0.96	1.00
P_60	0.72	1.20	1.33	1.19	1.14	1.00

Table 5.7: *Measured signal per aperture area relative to* 180″ *aperture.*

the 180″ aperture remains to be established. The necessary measurements have been performed to establish FCS power curves for the other apertures that were actually used by observers. However, these measurements were performed internally without celestial calibrators, comparing FCS measurements in standard configurations relatively to non-standard ones. With the now available signal linearization a new analysis effort would be necessary.

The main application of these ratios δ however is the calibration of multi aperture AOT P_04 observations . They consist of a sequence of measurements through circular apertures with increasing diameter, followed by an FCS measurement. The AOT was used to search for extended emission or companions around point like sources. The analysis method described by [18] works on a relative basis, dropping the not yet well understood FCS measurement made in the largest aperture of the sequence. Having applied the usual calibration steps to the signal, including dark current subtraction and signal linearization, it is assumed that the observed signal is proportional to the incident flux. The observed signals S_{aper} for the various apertures are modeled as comprising of a point source component and a background component according to:

$$S_{aper} = S_{src}\, F_{psf}(aper) + \frac{S_{bck}}{A_{aper}}\, \delta_{aper}. \tag{5.6}$$

F_{psf} is the PSF correction factor as given in Table 5.2, A is the area of the respective aperture (see Table 5.1) and δ is the relative effective solid angle correction given in Table 5.7. The ratio $\frac{S_{bck}}{A_{aper}}$ is determined from the difference of the two largest apertures:

$$\frac{S_{bck}}{A_{aper}} = \frac{S_{180} - S_{120}\frac{F_{psf}(180)}{F_{psf}(120)}}{A_{180} - A_{120}\frac{F_{psf}(180)}{F_{psf}(120)}}. \tag{5.7}$$

The model has been verified with calibration measurements on point sources[1]. Only for the smaller apertures of the sequences at 3.6 μm and 60 μm deviations were observed, which [18] attributes to misalignments among aperture centres and the simpler PSF model used.

Generally deviations can be interpreted as originating from additional structure in the vicinity of the central source. An example is shown in [18] for the source HD97300, where extended structure detected in the ISOPHOT aperture sequence is verified by ISOCAM to be an organic molecular ring of about 50″ × 36″.

5.5.4 Solid angles for PHT-C

Numerical calculations encounter the difficulty to fix the integration interval such, that the difference between the actual result and the integral to infinity are negligible. The impact

[1]Although the PSF model used for the verification was still the analytical one, the differences of the PSF correction factors are at the per cent level and were generally below the measurement accuracy.

is greater for larger wavelengths. Exemplary calculations with detector C100 for a growing sequence of integrated areas required field sizes above 0.5° ([27]) to achieve convergence of the curve of growth below the 2 % level.

It was tried to maximize the integrated field while keeping the computation times to a reasonable level for the C-detectors. Only the central area of 800″ diameter was densely sampled, while the larger outer field of 200′ diameter was only sparsely sampled with about 27 times the narrow stepsize. The method was validated by doing a calculation with small stepsize over the entire field.

The results for PHT-C solid angles as calculated by [27] are given in Table 5.8. All values are calculated for the monochromatic case and for nominal design dimensions of apertures. It is again reassuring to note that the derived numbers are very close to the geometrical solid angles of 4.45710^{-8} sr and 1.87810^{-7} sr for C100 and C200 respectively. Again all remarks w.r.t. OLP 10 and the use of Eq. inuomega or Eq. inuomega2 apply.

PHT-C Solid Angles of Single Pixels (design parameters)

filter	800″ array	200′ array	total
		[steradian]	
C_50	4.610e-08	4.377e-10	4.654e-08
C_60	4.441e-08	3.708e-10	4.478e-08
C_70	4.580e-08	4.689e-10	4.627e-08
C_90	4.129e-08	4.349e-10	4.172e-08
C_100	4.195e-08	4.791e-10	4.242e-08
C_105	4.613e-08	6.293e-10	4.676e-08
C_120	1.731e-07	2.534e-09	1.756e-07
C_135	1.811e-07	3.637e-09	1.847e-07
C_160	1.696e-07	3.979e-09	1.736e-07
C_180	1.895e-07	4.719e-09	1.942e-07
C_200	1.614e-07	4.557e-09	1.660e-07

Table 5.8: *Solid angles derived from integrated beam profiles of single pixels for different PHT-C filters. The second column shows the integrals of the narrowly spaced central section, while the third column shows the integral over the surrounding sparsely sampled area. The fourth column shows the sum of the previous two.*

5.5.5 Solid Angles for PHT-S

The way the PHT-S beam profiles were constructed was already discussed in Sect. 5.4.6. The measured beam profiles extend to an area of ±60″. Results for PSF factors and solid angles using these data are given in [6].

However, due to the degrading quality of the weaker signals in the wings and the artefacts, introduced by the beam profile reconstruction method, for solid angle calculation the region outside the geometrical aperture of 24″ × 24″ was replaced by the theoretical model according to Eq. 5.1 (priv. comm. P. Abraham 2001). In order to do this, two integrations over the theoretical model were performed. One only out to the borders of the geometrical aperture, and the other out to "infinity" (most likely ±60″). The ratio of these two integrals was used to correct the old solid angles calculated by [23], which were only integrated over the geometrical aperture. In other words, the old solid angles were corrected with the respective PSF factors f_{psf}. In Table 5.9 these factors, as derived by [6] are given.

The solid angles, shown in the same table, were taken from a PIA 9.1 reduced spectrum expressed in point sources fluxes F_ν and extended source fluxes I_ν according to:

$$\Omega = \frac{F_\nu}{I_\nu} \frac{f_{psf}^2}{(1-\epsilon^2)} \tag{5.8}$$

This reverse way was chosen, since the solid angles are not available explicitly in a Cal-G file. Note that also the factor $(1-\epsilon^2)$ is eliminated. For correction of OLP or PIA results again all previous remarks w.r.t. Eq. 5.3, Eq. 5.5 and the $(1-\epsilon^2)$ factor apply.

pix	f_{psf}	Ω $[10^{-7}sr]$	pix	f_{psf}	Ω $[10^{-7}sr]$	pix	f_{psf}	Ω $[10^{-7}sr]$	pix	f_{psf}	Ω $[10^{-7}sr]$
1	0.975	0.0952	33	0.957	0.1024	65	0.933	0.1068	97	0.906	0.0923
2	0.975	0.0960	34	0.956	0.1026	66	0.932	0.1063	98	0.906	0.0929
3	0.974	0.0969	35	0.956	0.1029	67	0.931	0.1063	99	0.906	0.0945
4	0.973	0.0975	36	0.955	0.1028	68	0.930	0.1055	100	0.905	0.0950
5	0.973	0.0982	37	0.955	0.1031	69	0.929	0.1054	101	0.905	0.0966
6	0.972	0.0989	38	0.954	0.1031	70	0.928	0.1054	102	0.904	0.0969
7	0.972	0.0993	39	0.954	0.1033	71	0.927	0.1047	103	0.902	0.0971
8	0.971	0.0998	40	0.954	0.1032	72	0.927	0.1046	104	0.902	0.0986
9	0.970	0.1003	41	0.953	0.1034	73	0.926	0.1046	105	0.900	0.0986
10	0.970	0.1009	42	0.953	0.1035	74	0.926	0.1045	106	0.900	0.1000
11	0.969	0.1013	43	0.953	0.1036	75	0.925	0.1037	107	0.898	0.0999
12	0.968	0.1016	44	0.952	0.1034	76	0.925	0.1036	108	0.898	0.1012
13	0.968	0.1020	45	0.951	0.1033	77	0.924	0.1034	109	0.896	0.1010
14	0.967	0.1022	46	0.951	0.1033	78	0.923	0.1032	110	0.896	0.1022
15	0.966	0.1023	47	0.950	0.1032	79	0.922	0.1030	111	0.894	0.1018
16	0.966	0.1026	48	0.950	0.1032	80	0.921	0.1026	112	0.894	0.1031
17	0.965	0.1027	49	0.950	0.1031	81	0.920	0.1023	113	0.892	0.1027
18	0.965	0.1028	50	0.949	0.1027	82	0.919	0.1019	114	0.892	0.1039
19	0.964	0.1030	51	0.949	0.1026	83	0.918	0.1015	115	0.890	0.1034
20	0.964	0.1031	52	0.948	0.1025	84	0.917	0.1012	116	0.890	0.1045
21	0.964	0.1032	53	0.948	0.1023	85	0.916	0.1008	117	0.888	0.1039
22	0.963	0.1031	54	0.947	0.1021	86	0.915	0.1004	118	0.888	0.1049
23	0.963	0.1032	55	0.947	0.1018	87	0.915	0.1010	119	0.887	0.1043
24	0.962	0.1030	56	0.946	0.1015	88	0.914	0.1005	120	0.887	0.1052
25	0.962	0.1029	57	0.946	0.1012	89	0.913	0.1001	121	0.885	0.1045
26	0.961	0.1026	58	0.945	0.1009	90	0.912	0.0996	122	0.885	0.1053
27	0.961	0.1024	59	0.945	0.1006	91	0.910	0.0991	123	0.885	0.1062
28	0.960	0.1022	60	0.945	0.1006	92	0.910	0.0996	124	0.883	0.1053
29	0.960	0.1019	61	0.945	0.1001	93	0.909	0.0991	125	0.883	0.1061
30	0.959	0.1014	62	0.944	0.0997	94	0.908	0.0985	126	0.883	0.1053
31	0.958	0.1011	63	0.944	0.0993	95	0.907	0.0981	127	0.883	0.1060
32	0.957	0.1006	64	0.944	0.0988	96	0.907	0.0985	128	0.883	0.1066

Table 5.9: *PSF factors and solid angles for PHT-S. The solid angles are corrected for the* $1-\epsilon^2$ *factor and the normalization of the centre position to 1 for consistency.*

5.5.6 Construction of PHT maps

Once flux calibration has been performed on a series of raster positions and pointing information has been added (PIA AAP level), a map of the respective sky region can be constructed. In order to be most efficient, pixel sizes are somewhat matched to the airy disks at the respective wavelengths, not to waste neither resolution by making pixels too big, nor time, by making pixels too small. This however, introduces some difficulties, that makes map construction a non-trivial task in the ISOPHOT case.

As described by [3], four different methods are presently available for ISOPHOT map construction, i) the "full coverage" method, ii) the "distance weighting" method, iii) the "trigrid" method and iv) the "drizzling" method. The fluxes determined at the various positions on the sky are co-added and combined, weighting the flux contributions to a map element either with the shared area of the geometric dimensions of a PHT-C pixel (full coverage) or with the third power distance of the pixel centre to the centre of the map element (distance weighting). The trigrid method averages groups of data points that are spatially much closer together than the airy disc, and then from all remaining averaged data points constructs a mesh of smallest triangles in the sky plane. The fluxes of the map elements are interpolated within the triangles either linearly or using smooth quintic polynomial interpolation, which takes into account derivatives of the neighboring triangles. The drizzling method available in the IRAF analysis package is a more sophisticated relative of the "distance weighting" method with improved angular resolution.

None of these methods however makes use of the actual or modelled beam profiles available.

5.5.7 Map simulator

Due to the lack of a more physical method for map reconstruction and the great level of complexity of the matter, a program to simulate observations was developed [3]. Point sources, described by delta functions are convolved with the beam profiles of the filter used in an array with elements considerably smaller than the point spread function. A background level, if necessary with gradients, can be added.

This simulated sky is then sampled at the positions the specified AOT with its parameters would visit during its execution. The resulting timeline of fluxes as would be seen by the instrument is then transformed back into either calibrated instrument fluxes or instrument signals, including the respective pointing information. The resulting data format is consistent with SRD or AAP level formats of the interactive analysis PIA and can be subjected to the same data reduction and map construction methods as applied to the real data. Thus specific effects and artefacts arising from map construction methods and AOT pointing sequences can be studied in great detail.

5.6 Conclusions

The work by a number of people has brought quite some clarification to PSF and beam profile related issues, however some open questions still remain. After the more accurate numerical PSF model has been introduced, finally also consistency regarding the PSF-factors was achieved. For the C-arrays the discrepancies between pixel and array centred photometry was explained and empirical PSF factors, consistent with the theoretical model, could be established. The measured PHT-S beam profiles became usable to correct photometry for point sources that are not well centred, however since satellite mispointing compared to observer error is less likely, the method was restricted to interactive analysis. Near-field straylight is as expected from pre-mission studies, while no far-field straylight was detected during a series of observations during Earth eclipses. However, the Serendipity mode revealed a straylight ring at $0.7°$ to $1.0°$ from a bright source at 170 μm, that observers should be aware of. The solid angles for the extended source calibration were also re-calculated to be consistent with the numerical PSF model. An inappropriate term $(1 - \epsilon^2) = 0.91$ was discovered in the conversion from point source fluxes to extended source fluxes, which unfortunately could not anymore be removed from the OLP 10 software and increases all extended source fluxes by 9 %. Still there is another uncertainty about the effective size of the solid angles, which needs further clarification. This issue becomes important for all cases, where the PSF-factor is very different from 1. If correct, the matter will decrease all solid angles and thus increase all extended source fluxes by this factor f_{psf}. The present OLP 10 still kept the larger solid angles. The actual beam profiles of PHT-P turn out to be very different from theoretical expectations and FCS calibration is difficult with non-standard apertures. More work would need to be invested here. However, empirical relative solid angles were determined to help there and in particular in multi aperture AOT calibration. The theoretical knowledge about beam profiles is not used in the re-construction of maps, however is included in the data reduction process via the map simulation tool.

Bibliography

[1] Ábrahám, P. 1990, "Correction for Off-Centre Positioning of Point Sources in the ISOPHOT-S Aperture" MPIA internal report

[2] Ackermann, E. 1990, Diploma thesis, MPI für Astronomie, Heidelberg

[3] Gabriel, C., Hur., M. 2000, "Map Coadding and Simulation Techniques with the ISOPHOT Interactive Analysis", proc. conf. "ISO Beyond Point Sources: Studies of Extended Infrared Emission", Madrid, Spain, 14-17 Sep 1999, eds. Laureijs, R., Leech, K., Kessler, M.F., ESA SP-455

[4] Herbstmeier, U. 1998, "ISOPHOT Footprints C100-Comparison between modelled and measured footprints - the derived parameters", internal report

[5] Herbstmeier, U. 1998, "ISOPHOT Footprints C200-Comparison between modelled and measured footprints - the derived parameters", internal report

[6] Herbstmeier, U. 1998, "ISOPHOT Footprints and Near-Field Straylight S-Re-analysis of cross scans to extract measured footprint and associated parameters", internal report

[7] Héraudeau, Ph., Surace, C., Herbstmeier, U. 1997, "Report on beam profiles measurement of the ISOPHOT C100 and C200 detector arrays" MPIA internal report

[8] Kessler, M.F., Steinz, J.A., Anderegg, M.E., et al. 1996, A&A, 315, L27

[9] Klaas, U., Lemke, D., Kranz, T., Laureijs, R.J., Leinert, C., Schubert, J., Stickel, M., Tóth, L.V. 1998, Proc. SPIE 3354-111

[10] Klaas, U., Acosta Pulido, J.A., Abraham, P., et al. 1997, Proc. "First ISO Workshop on Analytical Spectroscopy", 6-8 Oct. 1997 (ESA SP-419, Dec. 1997)

[11] Laureijs, R.J. 1999, "Point spread function fractions related to the ISOPHOT C100 and C200 arrays", IDC document, URL: `http://www.iso.vilspa.esa.es/users/expl_lib/PHT/ c200fpsf02.ps.gz`

[12] Laureijs, R.J., 2000, "Assessment of ISOPHOT solid angle calculations", IDC internal report

[13] Laureijs, R.J., Klaas, U., Richards, P.J., Schulz, B., Ábrahám, P. ISO Handbook, Volume V: PHT–The Imaging Photo-Polarimeter, Version 1.1 (01/Nov/2000)

[14] Lemke, D., Klaas, U., et al. 1996, A&A, 315, L64

[15] Lemke, D., Kranz, Th., Klaas, U., Krause, O., Schubert, J., Stickel, M., Tóth, L.V. Wolf, J., "Straylight in ISOPHOT?", Proc. "The Calibration Legacy of the ISO Mission", VILSPA, Spain, Feb. 2001 (ESA SP-481) in press.

[16] Metcalfe, L., Kessler, M.F. 1991, "Scientific capabilities of ISO payload", ISI-SSD-8805, Issue 1.0, 1991

[17] Müller T.G., 2000, "ISOPHOT Aperture Profiles and Background Measurements", proc. conf. "ISO Beyond Point Sources: Studies of Extended Infrared Emission", Madrid, Spain, 14-17 Sep 1999, eds. Laureijs, R., Leech, K., Kessler, M.F., ESA SP-455

[18] Müller T.G., 2000, "ISOPHOT Aperture Sequences on Point- and Extended Sources" proc. conf. "ISO Beyond Point Sources: Studies of Extended Infrared Emission", Madrid, Spain, 14-17 Sep 1999, eds. Laureijs, R., Leech, K., Kessler, M.F., ESA SP-455

[19] Okumura, K. 2000, "The ISO Point Spread Function and CAM Beam Profiles", proc. conf. "ISO Beyond Point Sources: Studies of Extended Infrared Emission", Madrid, Spain, 14-17 Sep 1999, eds. Laureijs, R., Leech, K., Kessler, M.F., ESA SP-455

[20] Peschke, S.B. 1999, "Analysis of pointing effects on PHTS measurements", IDC internal report

[21] Pfisterer et al. 1993 Report BRO 2270, Breault Research

[22] Schubert, J. 1996, "The Beam Profile and Stray Light of PHT-S", MPIA internal report

[23] Schubert, J. 1996, Ph.D. thesis, Ruprecht Karls Universität, Heidelberg

[24] Schulz, B. 1993, Ph.D. thesis, Ruprecht Karls Universität, Heidelberg

[25] Schulz, B., Huth, S., Kinkel, U., Lemke, D., Acosta-Pulido, J.A., Braun, M., Castañeda, H., Cornwall, L., Gabriel, C., Heinrichsen, I., Herbstmeier, U., Klaas, U., Laureijs, R., Müller, T. 1999, proc. conf. "The Universe as seen by ISO", eds. Cox, P., Kessler, M.F., ESA SP-427

[26] Schulz, B. 1999, "Linearisation of ISOPHOT-P and C detector signals in OLP 8", IDC document, URL: `http://www.iso.vilspa.esa.es/users/expl_lib/PHT/r_nonlin.ps.gz`

[27] Schulz, B. 2000, "Calculation of PSF Factors and Solid Angles for ISOPHOT ", IDC document, URL: `http://www.iso.vilspa.esa.es/users/expl_lib/PHT/fpsf_report.ps.gz`

[28] Schulz, B., 2000, "ISOPHOT Flux Density and Surface Brightness", IDC internal report

Chapter 6

SWS Beam Profiles

6.1 Introduction

In the ISO SWS Observer's Manual (ref [1]), the SWS geometry has a rectangular apertures, with dimensions depending on the selected AOT band. Since the aperture is located in the telescope focal plane, the SWS beam profile was then assumed to be the convolution of this rectangle with the telescope's point spread function.

In reality, the situation is more complex. Within the SWS, the aperture is re-imaged twice. Vignetting and diffraction occur both at the focal-plane aperture and at an internal pupil image. These effects influence the beam profile in the dispersion direction: they make the profile narrower than what should be expected from the slit width. In the other dimension the beam profile is affected by geometrical imaging defects. Both these effects were observed in practice, while the instruments was in-orbit. The profiles were found to be narrower than expected and on top of that misalignments between the six detector arrays shifted the profiles to significantly different cross-dispersion positions. These effects made the SWS very sensitive even more sensitive to small pointing offsets than foreseen in the original design. This triggered an improvement of the ISO pointing to a level far beyond the specifications (as discussed in Chapter 5). However, the ISO pointing still is a limiting factor in the SWS flux and wavelength accuracy.

In this chapter we discuss the SWS optics, the beam profile observations, the development of a beam-profile model that is reasonably consistent with the observations, the derivation of the beam profile calibration files and the application of routines in the SWS Interactive Analysis system which allow to investigate beam related problems and correct some of them.

6.2 The SWS optical design

Full instrument descriptions can be found in de Graauw and al (1996) (ref. [2]) and in the ISO handbook (ref. [3]). This section presents a very simplified instrument layout, which contains all the elements of interest for the beam-profile analysis.

Figure 6.1 shows the simplified layout of the SWS optics, limiting itself to the heart of the instrument: an entrance slit image, a collimator, a diffraction grating with a scanner mirror that sets the angle of incidence on the grating, and finally a detector image.

The slit image is separated from the physical slit by flat folding optics and by a dichroic beam splitter. These components can be assumed not to affect the optical properties of the system. The slit length is oversized and is assumed to play no role in the shape of the beam profile.

The collimator is depicted as a single mirror. This is a simplification, because the actual collimator uses two non-spherical mirors to provide a strongly elliptical pupil image at the grating.

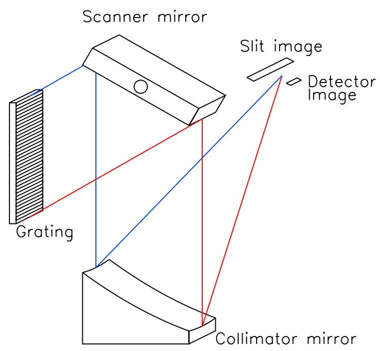

Figure 6.1: *Simplified lay-out of the essential elements of the SWS optics.*

This design allows a high spectral resolution in a small volume. For the purpose of this analysis, the pupil deformation is not important.

The scanner mirror rotation can be half of the rotation that would otherwise have been required of the grating. This smaller rotation was well suited for the flexure pivots that support the mirror.

A dispersed slit image is projected onto the detector image. Finally, the detector image is projected onto the physical detector. Again, this projection distorts the image, to map a square detector onto a rectangular slit image at the collimator exit. And again, the nature of these distortions is not of direct interest for the analysis of the beam profiles.

The slit and detector images in the near the collimator focus are close enough together to ignore their separation in the analysis.

In monochromatic light, the image of the detector in the entrance slit is narrower than the slit and it is much shorter. Of course, with continuum radiation the dispersed detector image fills the width of the slit. So in the dispersion direction (Z) the slit width determines the SWS beam size, in the other direction (Y) the SWS aperture is defined by the detector image in the slit.

The presence of the flat scanner mirror close to the grating was found to be problematic: repeated reflections between scanner mirror and grating caused serious spectral ghosts. These ghosts were successfully removed by increasing the distance between the scanner mirror and the grating and by covering the ends of the collimator mirror and the scanner mirror with absorbing and deflecting material. As an undesirable side effect, these measures caused or increased vignetting in the collimated beam. This reduced the transmission of the optics, but it also affected the beam profile: if the diffraction spot is moved away from the slit centerline, diffraction at the slit edges increases and the illumination of the pupil image near the grating spreads out. The reduced response near the slit edges causes a narrowing of the Z beam profile!

The spectral performance of SWS was designed and verified to be diffraction-limited. In the cross-dispersion (Y) direction, the optical performance was commensurate with the oversized detector dimensions. These reduced optical demands allowed to use the anamorphous imaging of the telescope pupil onto the collimator pupil and of the spectral image at the collimator output onto the actual detectors. This caused the detailed beam shapes in this direction to be influenced by small imaging defects, which vary between the different detector arrays.

For an overview of the optical configuration of the SWS we refer to Table 6.1, adapted from the SWS Handbook.

Table 6.1: Detector definition for the SWS AOT bands

	AOT band	order	aperture		filter	area[5] ($'' \times ''$)	detector type	detector number	wavelength (μm)
SW	1A	4	1	t	Al_2O_3	14-20	InSb	1 - 12	2.38 - 2.60
SW	1B	3	1	t	Al_2O_3	14-20	InSb	1 - 12	2.60 - 3.02
SW	1D	3	2	t	LiF	14-20	InSb	1 - 12	3.02 - 3.52
SW	1E	2	2	t	LiF	14-20	InSb	1 - 12	3.52 - 4.08
SW	2A	2	2	t	LiF	14-20	Si:Ga	13 - 24	4.08 - 5.30
SW	2B	1	2	t	LiF	14-20	Si:Ga	13 - 24	5.30 - 7.00
SW	2C	1	3	t	SrF_2	14-20	Si:Ga	13 - 24	7.00 - 12.0
LW	3A	2	1	r	Al_2O_3	14-27	Si:As	25 - 36	12.0 - 16.5
LW	3C	2	2	r	LiF	14-27	Si:As	25 - 36	16.5 - 19.5
LW	3D	1	2	r	LiF	14-27	Si:As	25 - 36	19.5 - 27.5
LW	3E	1	3	r	SrF_2	20-27	Si:As	25 - 36	27.5 - 29.0
LW	4	1	3	r	SrF_2	20-33	Ge:Be	37 - 48	29.0 - 45.2
F-P1	5A	3	1	r	Al_2O_3	10-39	Si:Sb	49 - 50	11.4 - 12.2
F-P1	5B	2	1	r	Al_2O_3	10-39	Si:Sb	49 - 50	12.2 - 16.0
F-P1	5C	2	2	r	LiF	10-39	Si:Sb	49 - 50	16.0 - 19.0
F-P1	5D	1	2	r	LiF	10-39	Si:Sb	49 - 50	19.0 - 26.0
F-P2	6	1	3	r	SrF_2	17-40	Ge:Be	51 - 52	26.0 - 44.5

Notes:

1. SW = short-wavelength grating region

2. LW = long-wavelength grating region

3. t = transmission

4. r = reflection

5. 'Aperture area' refers to the nominal dimensions of the SWS detector bands projected on the sky.

6. Detector 49 is used for FP observations in band 5.

7. Detector 51 is used for FP observations in band 6.

6.3 The SWS beam profile measurements

6.3.1 Ground based testing

Prior to the ISO launch, no detailed calibration was available of the SWS beam profiles due to lack of a suitable point source in the ground based laboratory testing (ILTs).

6.3.2 Focal Plane Geometry

The Focal Plane Geometry calibration has been performed within the ISO Satellite Commissioning Phase (REVs 12,14,17,18,19,20). See Ref. [5] and [6] for details and Section 6.9 for the observations summary.

The offsets between each of the three SWS apertures and the ISO OSS Optical axis have been calibrated by making rasters maps around point-like sources, with the two SWS grating scanners set at fixed positions, corresponding to selected key wavelengths as defined in the flux calibration programme. In order to ensure the most accurate pointing, five guide stars were used. A special procedure was in place to insure quick turnaround times for the derivation and immediate application of the offsets.

The measurements were performed as follows: by means of square rasters around HR6705, one of the main SWS photometric calibrators, apertures 2,3 and 1 were calibrated in REV. 17. The offsets to the initial pointing were derived by the SIDT on the same day and used by the Spacecraft Control Centre (SCC) already the day after. These were verified with a finer square raster on aperture 2 and by cross-like rasters on the other two apertures.

In order to avoid possible effects specific to HR6705 and its associated guide stars for that day, other six point-like sources were used for further verification in REV. 19 and 20. All these measurements had been constructed via the Calibration Uplink System (CUS), as SWS AOTs do not allow measurements at fixed scanner positions and in raster mode.

The verification and fine tuning rasters were cross-like in order to optimise the use of time. The cross-like axis were parallel to the Y and Z axis of the spacecraft respectively. Each part of the cross consisted in a pair of scans, back and forward, in order to counteract possible detector hysterises effects. There exists two raster modes on ISO, one parallel to the spacecraft Y-axis (the longest side of the slit, along the SWS cross-dispertion direction) and one with a given orientation w.r.t. the Astronomical North (or=0 in the Appendix 1 tables). This second option was chosen, in order to ensure for both sides of the cross the back and forward configuration.

At the end of revolution 20, AOT 2 wavelength scans were perfomed at each side of the slits. As of revolution 21, the nominal pointing mode with one guide star was used, and the FPG was verified on HR6705 by means of a smaller square raster around it.

The FPG data analysis has been done by the SIDT following previoulsy written Calibration Analysis procedures (CAPs), stored in the SWS Interactive Analyisis (SIA). ¿From the ERDs, produced by the OLP team on time scales much shorter than in normal operations ("fast-ERDs"), SPDs were derived within SIA. On the other side, the FPGC files, produced by SCC, contained the Y and Z coordinates and the time keys of each raster point. These were used to chop the SPD in pieces, each associated with the SWS detector signals corresponding to each raster point. The signals were averaged over each of the six SWS detector bands and contour plots were produced for the square rasters, and polynomial fits were made of the cross-like rasters. The 50% signal levels were used to determine the centroid points. For more details over the results, see Ref. [6], [7], [8] and [9].

The FPG calibration proved to be good to the arcsecond level already in REV 19 an no further updates were requested. The analysis of the REV20 raster however (done with one guide star) showed a -2$''$ offset in the Z direction on HR6705, but this was judged by the SIDT not worth a further update of the FPG offsets.

6.3.3 FPG PV checks: cross-like rasters

As a further cross-check of the Focal Plane Geometry, dedicated cross-rasters were designed during the PV phase and inserted into the schedule. These were checks and therefore had to be short in time, however effort was invested to use these to prepare for the full characteristion of the beam profiles, planned to be over a number of wavelengths, covering also the FP range. Targets HR5340 and NML-CYG were used primarily for the grating and FP sections respectively.

At each raster point, the grating scanners were set to more than one fixed grating position, thus covering more than one pair of wavelengths, in general chosen to be the same key wavelengths as defined in the flux calibration programme. Being short checks, however, no back-forward scans were performed, and therefore the two sides of the cross were commanded to be parallel to the Y-axis.

6.3.4 Beam Profiles Large Scale calibration

The beam profiles were fully characterised as layed down in the IOCD sections 6.4.1.1 and 6.4.1.2, with fixed grating scanner positions, corresponding to the flux calibration key wavelengths and with rectangular rasters covering at least one diffraction beam outside the slit. Only small adjustments to the raster parameters were necessary, following the results of the preparatory crosses. Target HR5340 was used for the grating section and NML-CYG and ETA CAR for the FP section.

6.3.5 Beam Profiles Small Scale calibration: AOT1 and CUS AOT1-like sparse maps

The beam profiles depend on wavelength, clearly from AOT band to AOT band when either detector band or slit size change (cf. Table 6.1), but also in general within an AOT band, due to the dependency of the diffraction profile on wavelength. For this purpose were the AOT1 maps performed.

The first exercise of this kind was performed early in REV126, around HR6705. This consisted in a series of 7 quick (=speed 1) AOT1's performed as a cross-like shape covering the size of the smallest SWS aperture.

However, a pointing offset became apparent as well as an offset between detector bands which did not allow to cover both sides of the profile (see Figure 6.17).

A second and finer map was done on HR5340 later in REV244, but the results showed some inconsistency. Later on it was found that HR5340, being bright in the visible, was causing read-out blooming effects on the Star Tracker CCD, if used at time of the year when the orientation of the STR was parallel to the line of sight defined by HR5340 and the guide star used.

This type of exercise was then suspended, waiting for possible improvement of the ISO pointing accuracy. Once achieved (see Chapter 6 for a full description of the ISO Pointing improvements), three further exercises were perfomed to characterise the small scale beam profile close to the peak, via 5X5 rasters done at 2 arseconds steps on HR5340 (REV 640) and NML-CYG (REV 742) for the grating and FP sections respectively. A third exercise was done later on in REV 860, on HR1457 (for visibility reasons) to characterise on a fine scale the full wavelength dependency in the Z direction covering both sides of the profile. For time economy reasons, all these wavelength scans were made coarser than the fastest AOT1. Via the CUS, an AOT1-like was constructed by setting the grating scanner step size to 6 (instead of 4 for a speed 1 AOT1) and repeated in a raster pattern.

6.3.6 SSO Tracking corrections: subarcsecond scale Z-axis beam profile

ISO tracked Solar System Objects by means of successive linear rasters. The raster parameters were computed by the mission planning software so that on each raster leg the SSO was allowed to drift from -1$''$ to +1$''$ (prior to its improvement in revolution 290 via SCREW 254, the tracking was between 0$''$ and 2$''$). Dedicated measurements were performed in revolution 769 to characterise the beam profile on the subarsecond level, by letting the asteroid Vesta drift within the SWS aperture. See Figure 6.2 and Ref. [13] for details.

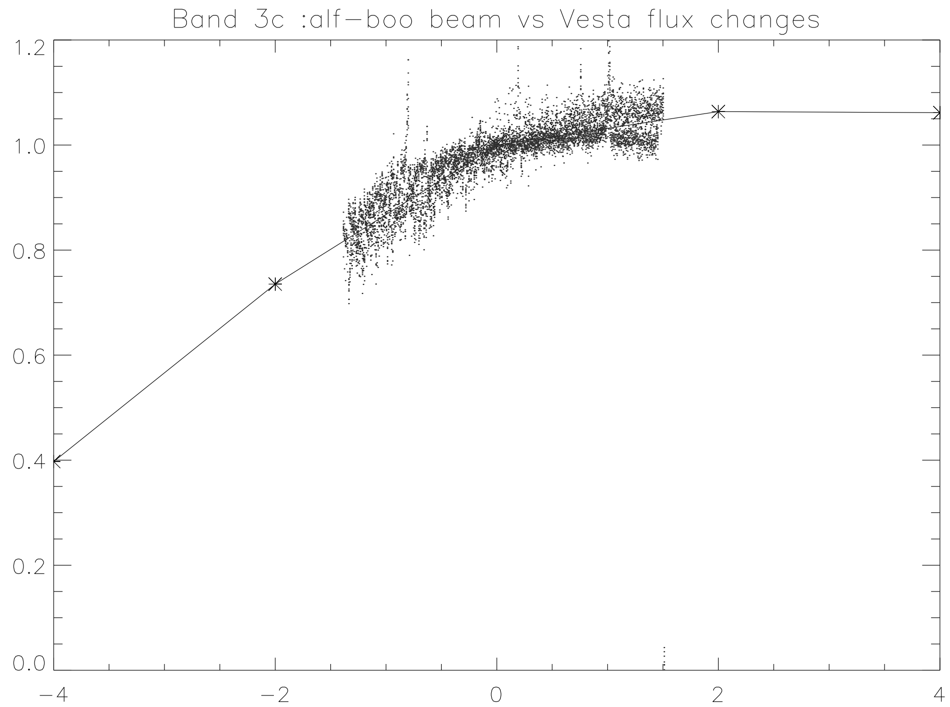

Figure 6.2: *Comparison between the change in signal as Vesta crosses through the SWS slit and the beam profile as derived from a 2 arc second raster on Alfa Boo for band 3C.*

6.3.7 Straylight from out of field sources characterisation

Out of beam radiation levels were characterised early in PV phase as layed down in IOCD section 6.4.3.1 on the bright source W HYA, down to 2 arcminutes distance from it. Later in the mission, specific straylight checks were performed, prompted by science needs for better characterise the influence of straylight for planet satellites such as Titan and Europa.

In REV. 384 the bright spectral line at 13.7 μm of the C_2H_2 molecule was observed on Saturn and at a position relative to Saturn, corresponding to Titan's western elongation of 3 arcminutes ($\mathrm{Y}_o ff$ = -87$''$, $\mathrm{Z}_o ff$ = - 163$''$), but with Titan far off the aperture, a few days later than the science observation on Titan. This gave a rejection factor of 10^4. Other two intermediate positions were chosen, coinciding with positions relative to Saturn as used in the beam profile full characterisation.

The search for water lines at 39.37 and 43.89 μm prompted for a pair of on-off measurements at Titan's Eastern elongation in June 1997 (revs. 579 and 581). These checks, lasting no more than 20 minutes each, were performed within the SWS Calibration time budget and consisted in 4 AOT2 up-down scans across the 39.37 μm line and 3 up-down scans across the 43.89 μm line. More extensive measurements of the background at the position of Titan's western elongation at those wavelengths were performed within the solicited time programme ZZH2O and are described in Ref. 7.

6.3.8 Introduction of the Virtual Aperture 4

The characterisation of the SWS beam profiles in the PV phase revealed a significant offset of detector band 6 with respect to the others (-9$''$ in Y direction), implying a signal loss of about 30Via SCREW 187 virtual aperture 4 was introduced for the FP observations to correct for this offset. This was verified in Rev. 161 with a sequence of AOT7's pointed at each side of the target NML-CYG along the Y axis and by a rectangular raster performed with the CUS, with grating and FP kept at fixed positions. Table 2 lists the observational details.

6.3.9 Data reduction

A consistent reprocessing of all beam profile related observations has been done at the end of the mission (in 1998). Two classes of CAPs were written, one for the CUS rasters (with fixed grating position) and one for the AOT1 and CUS AOT1-like maps. The reduced data have been stored as structures, in .xdr IDL save sets. These are of the form:

- CUS rasters with fixed grating scanner position(s).

  For each TDT and grating scanner position,

```
|-HEADER<Strng>(1)
|---WAVE<Float>(6)
|---DATA<Struc>(m*n)
                        |-Y_OFFSET<Float>(1)
                        |-Z_OFFSET<Float>(1)
                        |------DET<Struc>(52)
                                               |--FLUX<Float>(1)
                                               |-STDEV<Float>(1)
```

where HEADER is the SPD header and WAVE stores the wavelengths associated with each of the six detector bands corresponding to the grating scanner position, as relevant. The DATA part is a substructure, storing for each raster point the median Y and Z offsets as derived from the IIPH, and for each detector element, the median signal and standard deviation (in μV/s), after neglecting the first 5 seconds, the time needed for AOCS stabilisation after moving to that raster point (see also Figures 6.29 and 6.30).

- AOT1 and CUS AOT1-like maps

  For each TDT (i.e. aperture),

```
(m*n)
     |-Y_OFFSET<Float>(1)
     |-Z_OFFSET<Float>(1)
     |----BANDS<Struc>(12)
                          |------NAME<Strng>(1)
                          |----FACTOR<Float>(1)
                          |-INTERCEPT<Float>(1)
                          |-----SLOPE<Float>(1)
```

  giving for each point of the map the Y_OFFSET and Z_OFFSET, as the medians of the values derived from the respective IIPH file, and for each AOT band the result of a first order polynomial fit across the AOT band (flux vs. wavelength): the average flux across the AOT band, normalised to the on-target position (FACTOR), the INTERCEPT of the fit at the lower AOT band wavelength border, and the fit SLOPE.

The Y and Z offsets have been computed using routines stored in the SWS Interactive Analysis. These routines were translated in IDL from the original quaternions rotation routines which are part of the FORTRAN OLP DERIVE_IPH module. These coordinates have been checked to be aligned with the spacecraft Y and Z axis, including the signs, by comparing the sequence of a raster scan with the definition contained in the ICD-10 (ref. [16]): *Successive points on the first scan line (i.e. successive pointings of the telescope boresight on the celestial sphere) are progressing in the + Y direction and successive scan lines are progressing in the -Z direction, as illustrated below:*

```
*    *--<-*    *--<-*    ^ Y
^    v    ^    v  ^     |
|    |    |    |  |     |____> Z
*    *    *    *  *
|    |    |    |  |
^    v    ^    v  ^
*--<-*    *--<-*  *
```

So, a raster parallel to the S/C Y-axis always starts at the max positive Z and negative Y.

The result of the consistent processing of the data sets are shown in Figures 6.3 to 6.18.

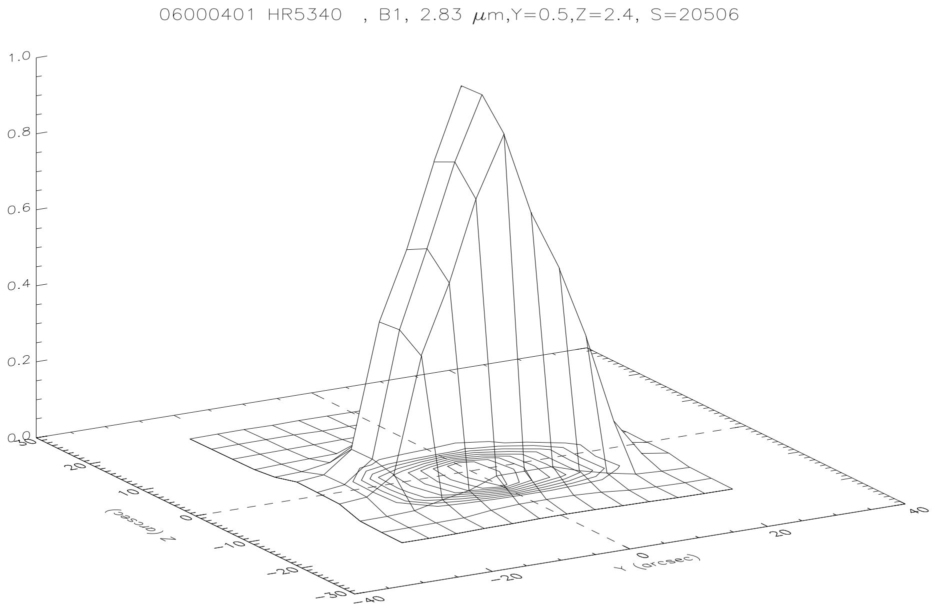

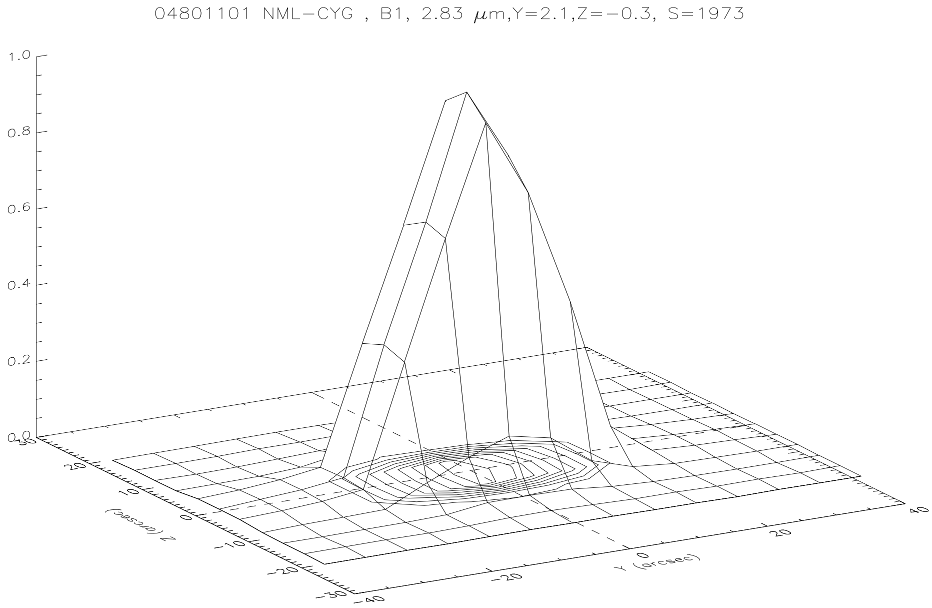

Figure 6.3: Beam profiles for Band 1, normalised to the maximum signal, given in the plot title (in μV/s). Contour plots are in steps of 10%, starting at 90% from the peak signal. The profiles have been shifted by the Y,Z offsets indicated, as provided by the pointing reconstruction algorithm (OLP Version $\geq$ 6.1)

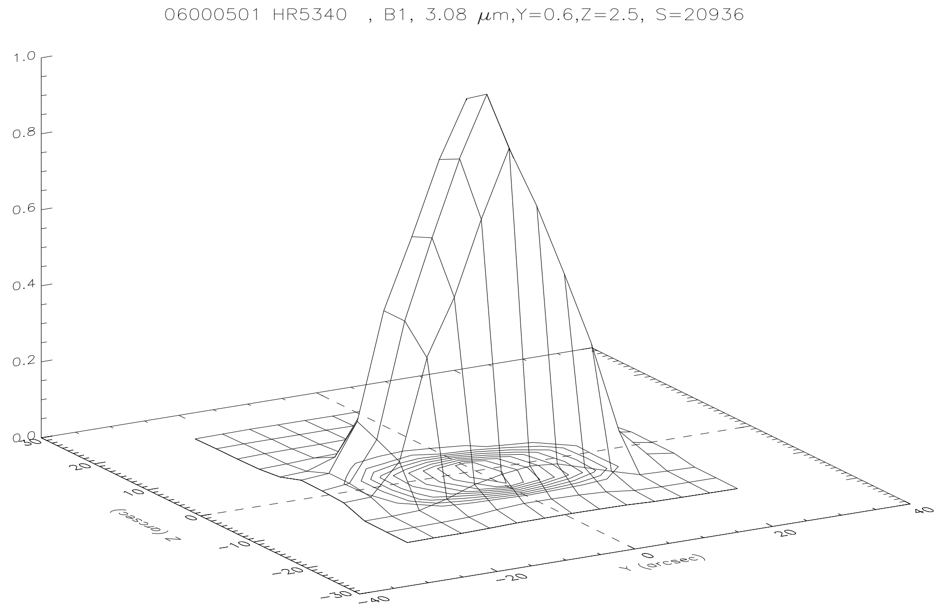

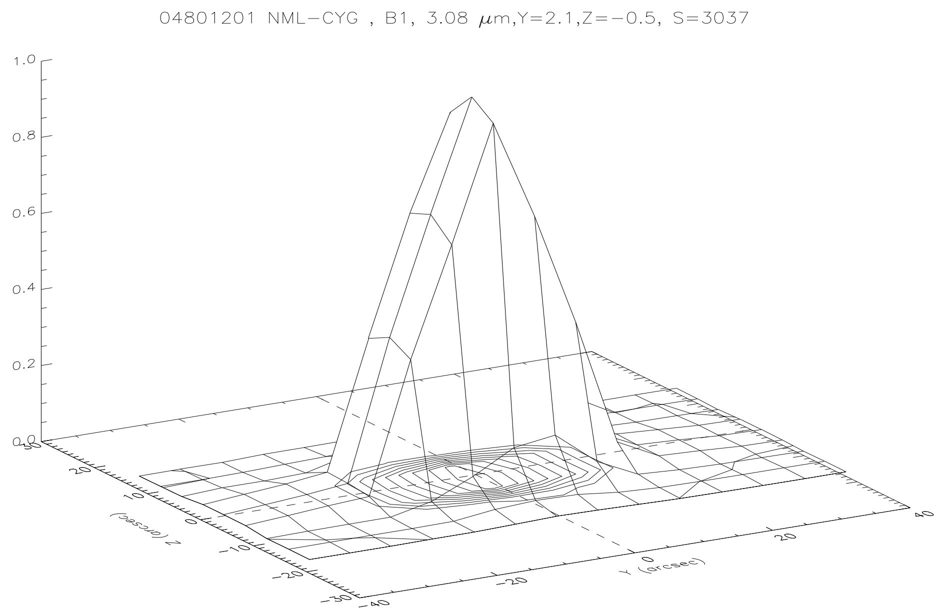

Figure 6.4: Beam profiles for Band 1, normalised to the maximum signal, given in the plot title (in μV/s). Contour plots are in steps of 10%, starting at 90% from the peak signal. The profiles have been shifted by the Y,Z offsets indicated, as provided by the pointing reconstruction algorithm (OLP Version $\geq$ 6.1)

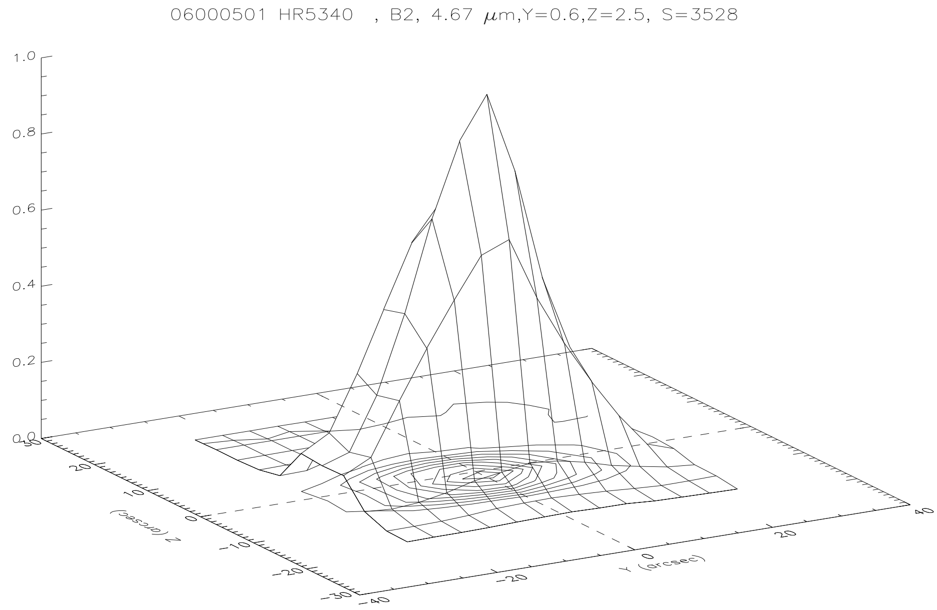

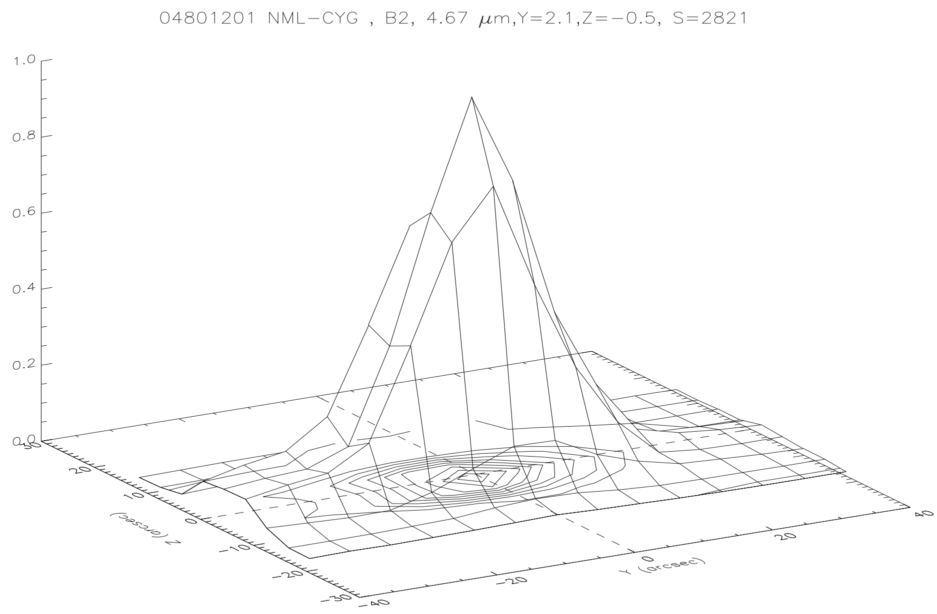

Figure 6.5: Beam profiles for Band 2, normalised to the maximum signal, given in the plot title (in μV/s). Contour plots are in steps of 10%, starting at 90% from the peak signal. The profiles have been shifted by the Y,Z offsets indicated, as provided by the pointing reconstruction algorithm (OLP Version $\geq$ 6.1)

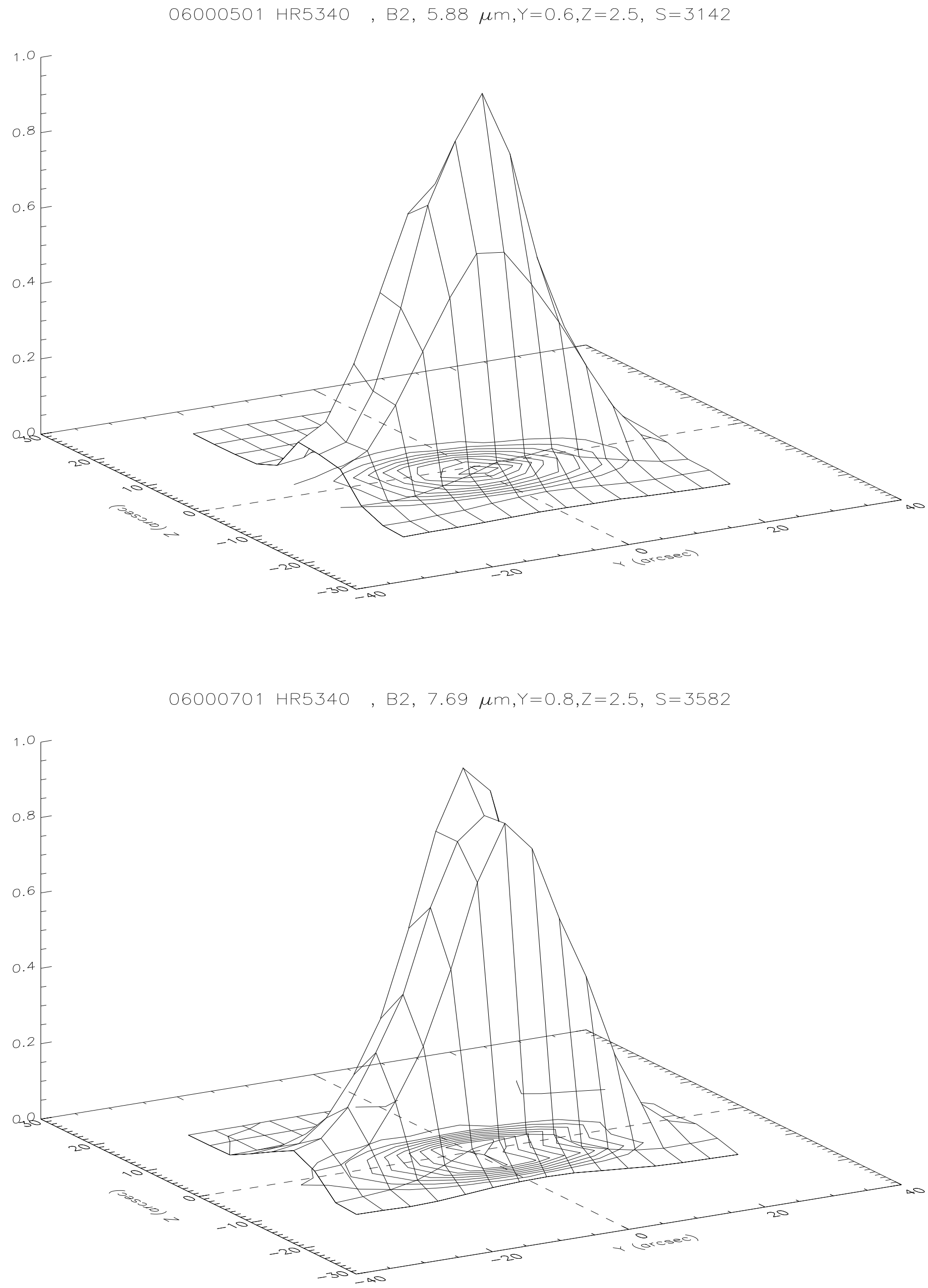

Figure 6.6: Beam profiles for Band 2, normalised to the maximum signal, given in the plot title (in μV/s). Contour plots are in steps of 10%, starting at 90% from the peak signal. The profiles have been shifted by the Y,Z offsets indicated, as provided by the pointing reconstruction algorithm (OLP Version $\geq$ 6.1)

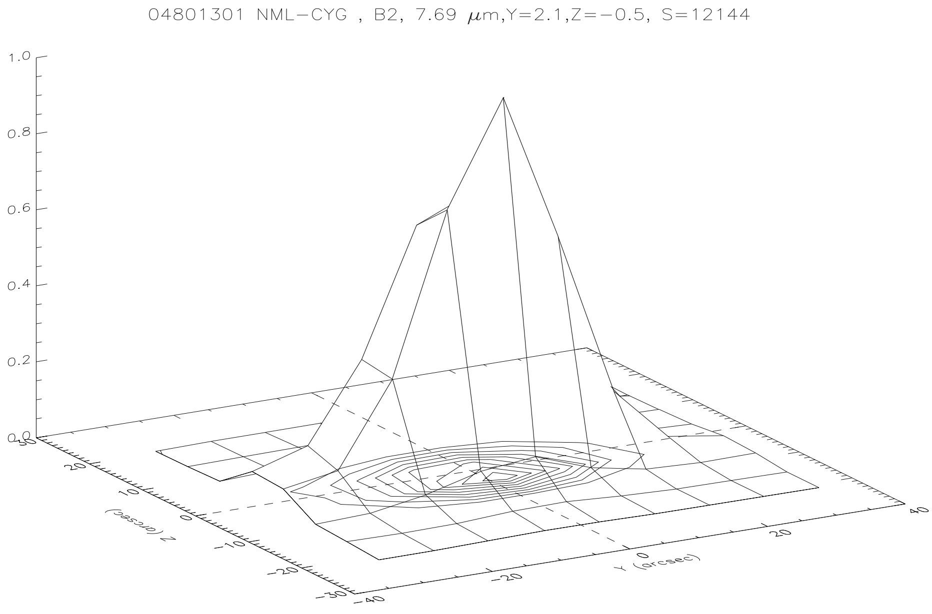

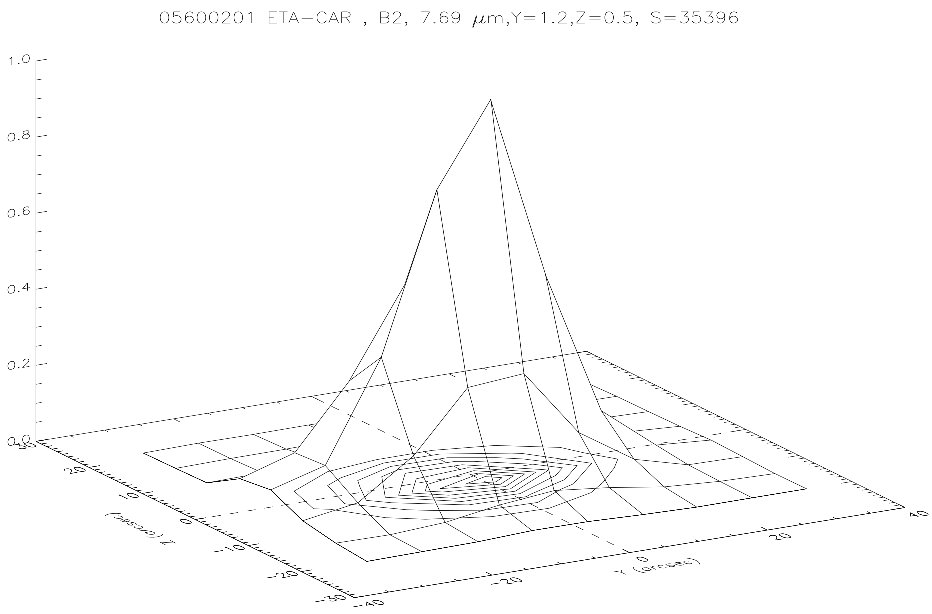

Figure 6.7: Beam profiles for Band 2, normalised to the maximum signal, given in the plot title (in μV/s). Contour plots are in steps of 10%, starting at 90% from the peak signal. The profiles have been shifted by the Y,Z offsets indicated, as provided by the pointing reconstruction algorithm (OLP Version $\geq$ 6.1)

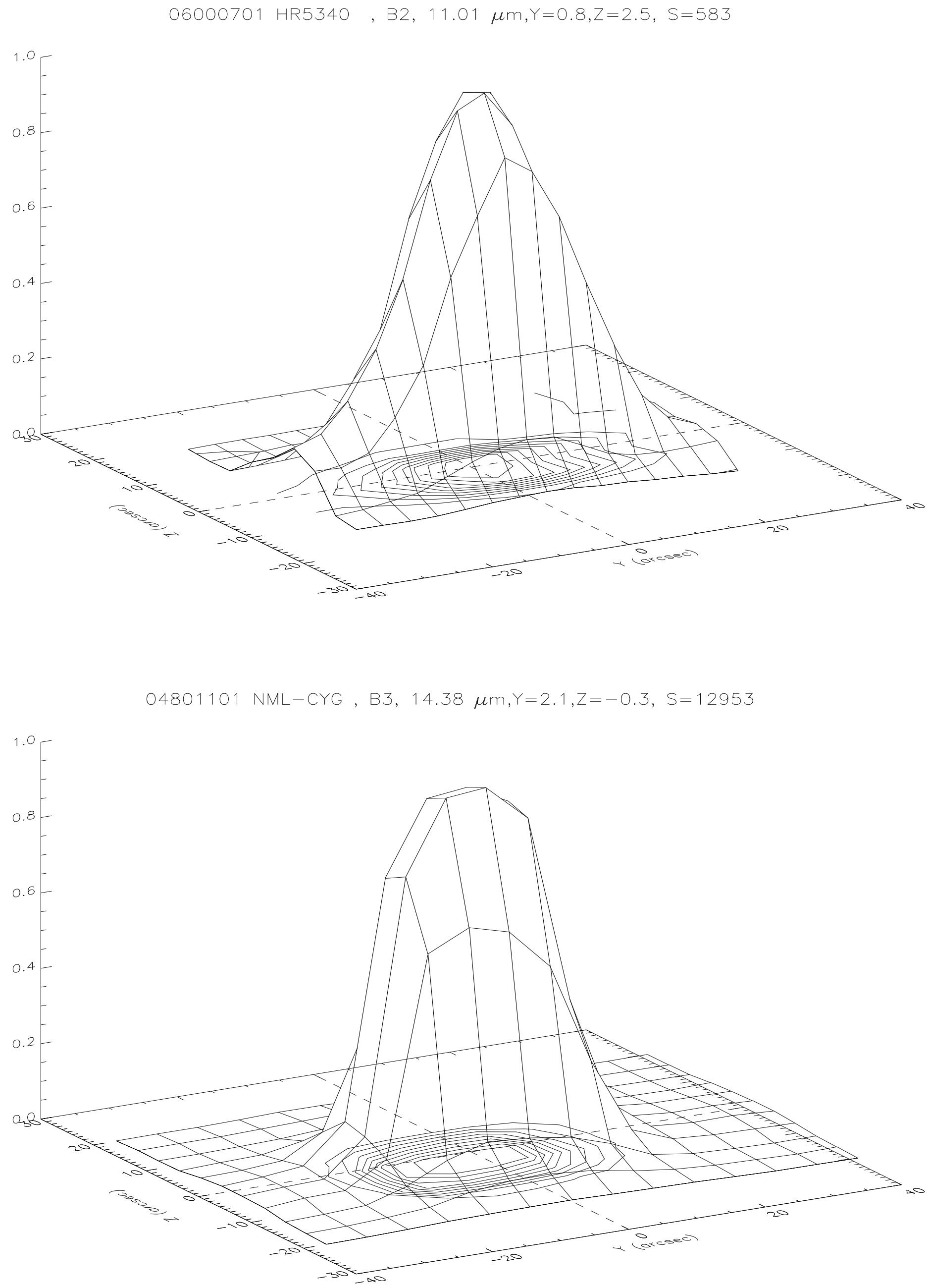

Figure 6.8: Beam profiles for Bands 2 and 3, normalised to the maximum signal, given in the plot title (in μV/s). Contour plots are in steps of 10%, starting at 90% from the peak signal. The profiles have been shifted by the Y,Z offsets indicated, as provided by the pointing reconstruction algorithm (OLP Version $\geq$ 6.1)

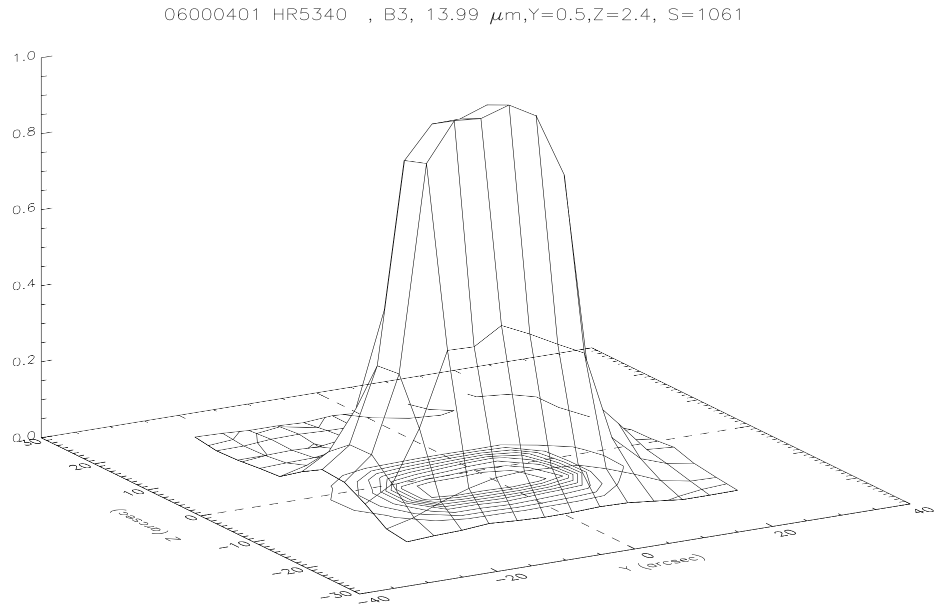

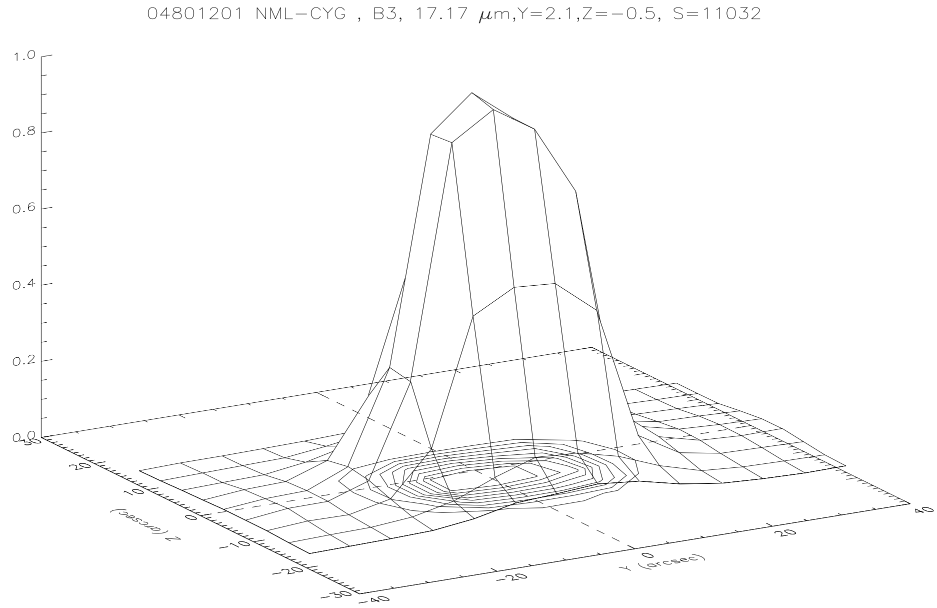

Figure 6.9: Beam profiles for Band 3, normalised to the maximum signal, given in the plot title (in μV/s). Contour plots are in steps of 10%, starting at 90% from the peak signal. The profiles have been shifted by the Y,Z offsets indicated, as provided by the pointing reconstruction algorithm (OLP Version $\geq$ 6.1)

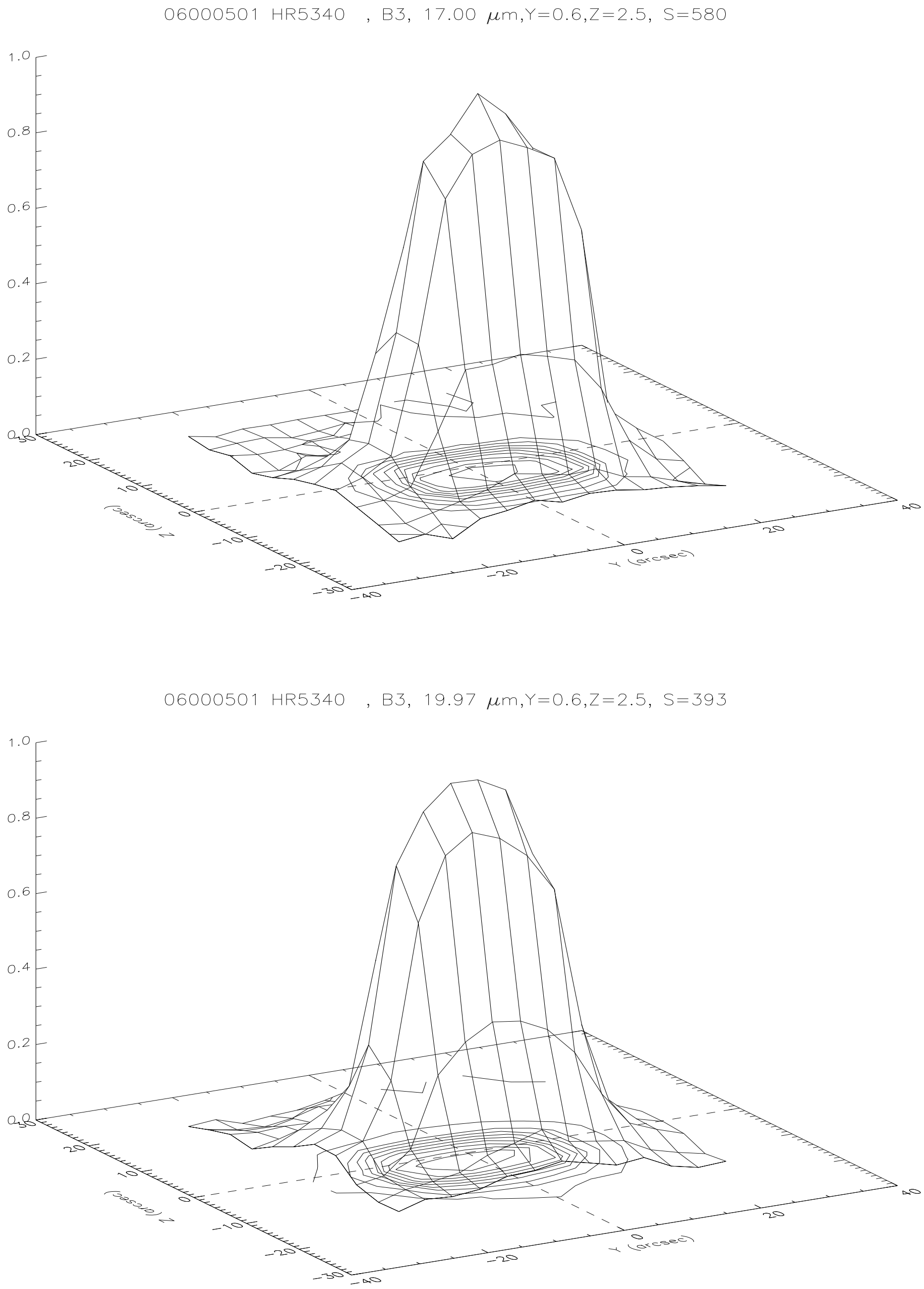

Figure 6.10: Beam profiles for Band 3, normalised to the maximum signal, given in the plot title (in μV/s). Contour plots are in steps of 10%, starting at 90% from the peak signal. The profiles have been shifted by the Y,Z offsets indicated, as provided by the pointing reconstruction algorithm (OLP Version $\geq$ 6.1)

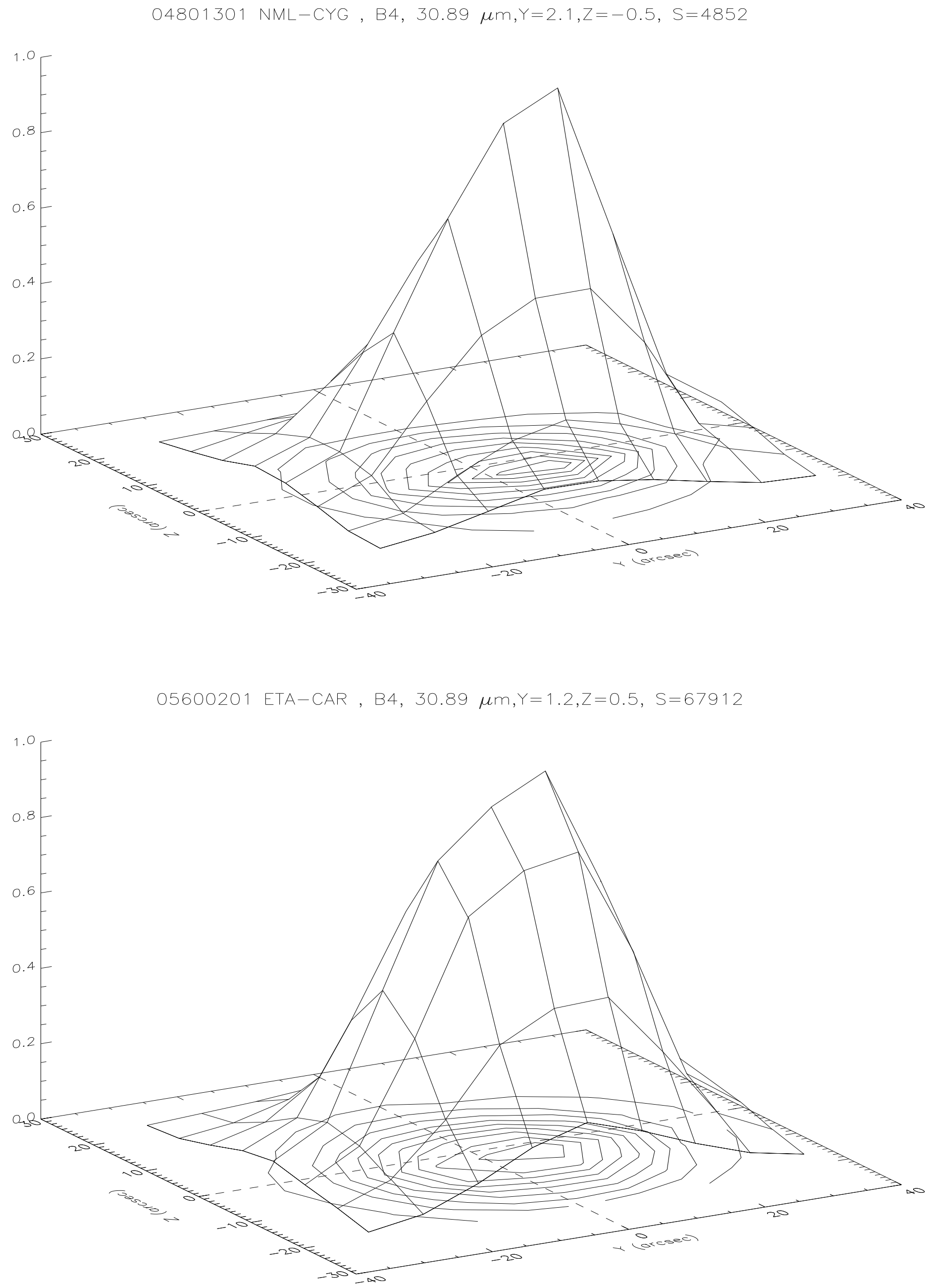

Figure 6.11: Beam profiles for Band 4, normalised to the maximum signal, given in the plot title (in μV/s). Contour plots are in steps of 10%, starting at 90% from the peak signal. The profiles have been shifted by the Y,Z offsets indicated, as provided by the pointing reconstruction algorithm (OLP Version $\geq$ 6.1)

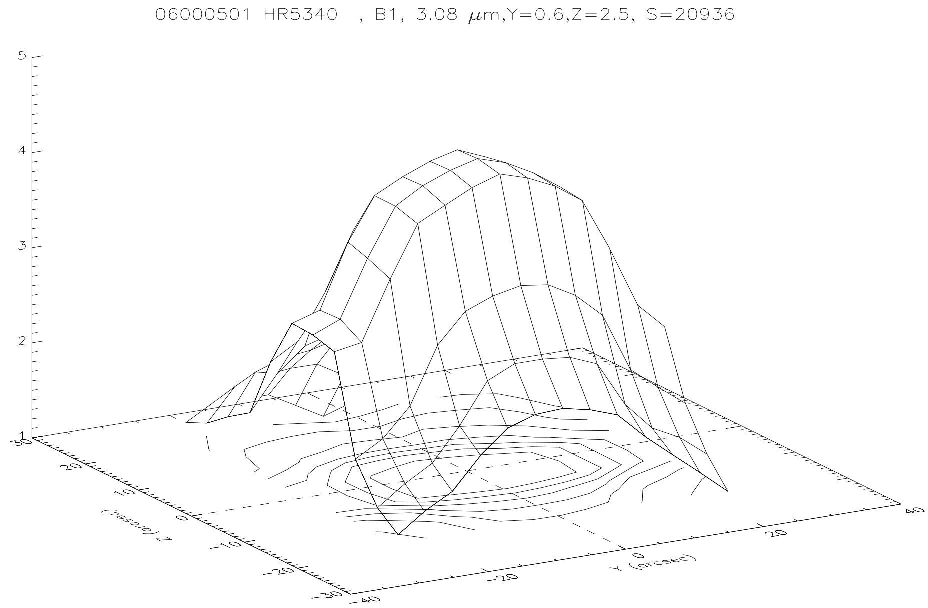

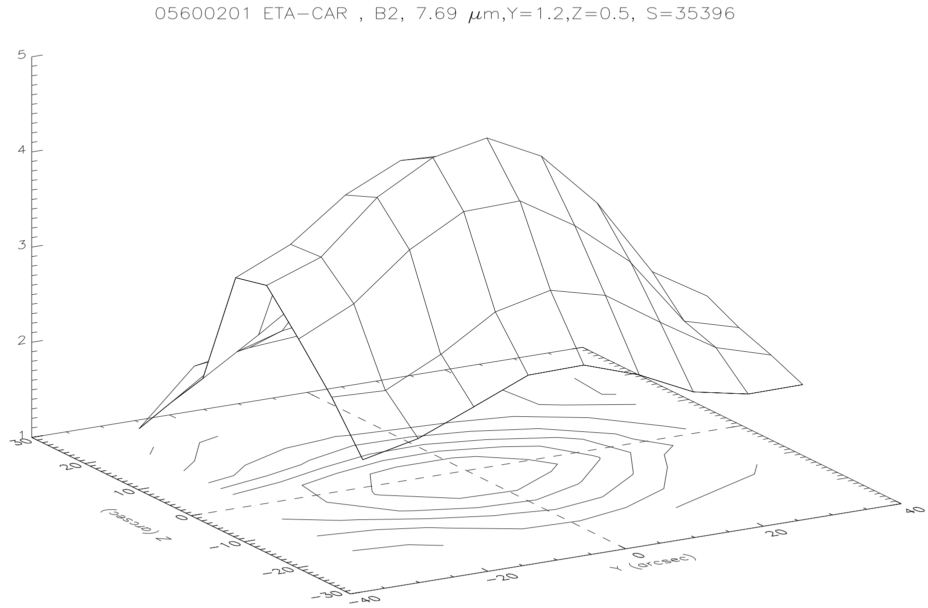

Figure 6.12: Beam profiles for Bands 1 and 2, in absolute signal values, on a LOG10 scale. The maximum signal is given in the plot title (in μV/s). Contour plots are in steps of 10%, starting at 90% from the LOG10 of the peak signal. The profiles have been shifted by the Y,Z offsets indicated, as provided by the pointing reconstruction algorithm (OLP Version $\geq$ 6.1)

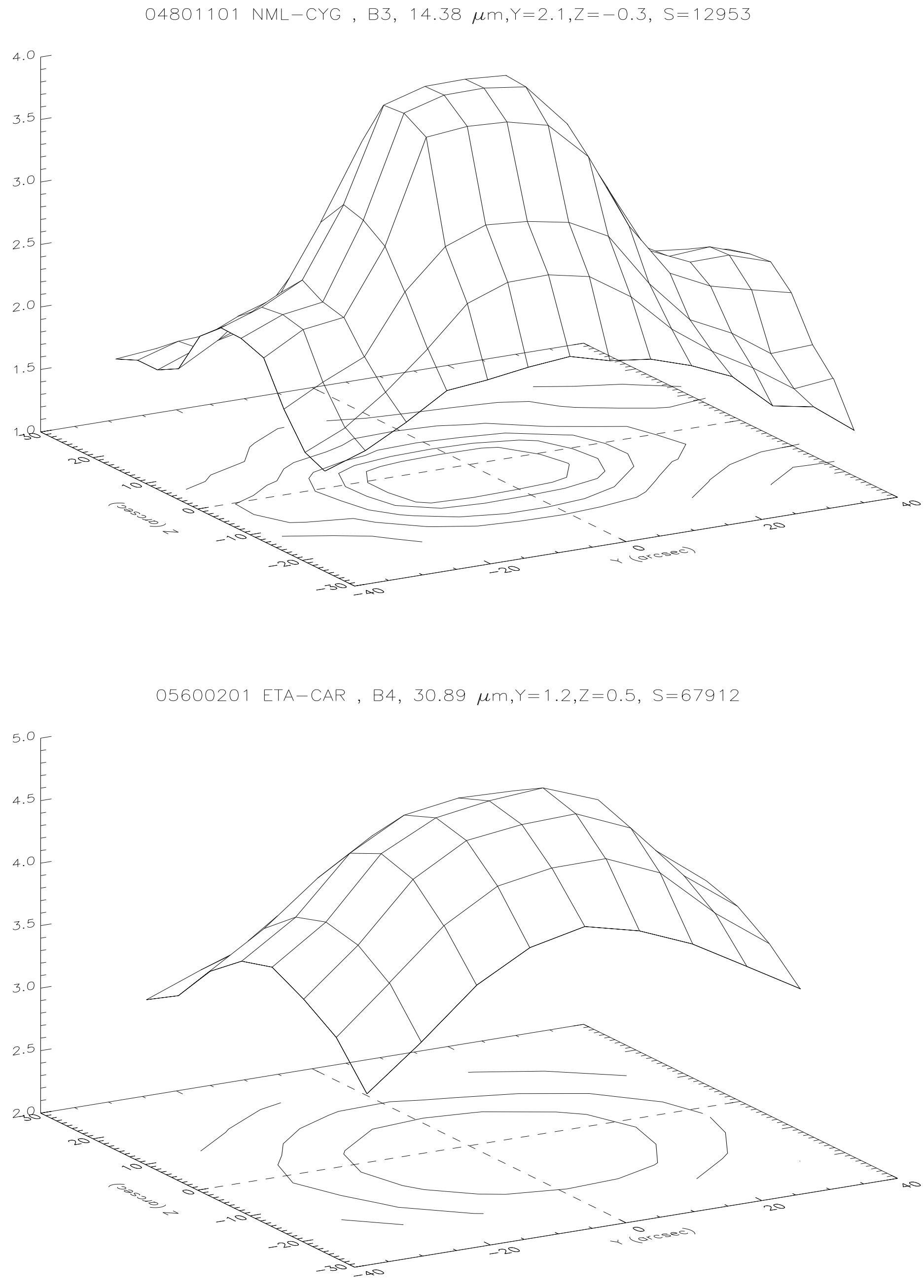

Figure 6.13: Beam profiles for Bands 3,4, in absolute signal values, on a LOG10 scale. The maximum signal is given in the plot title (in μV/s). Contour plots are in steps of 10%, starting at 90% from the LOG10 of the peak signal. The profiles have been shifted by the Y,Z offsets indicated, as provided by the pointing reconstruction algorithm (OLP Version $\geq$ 6.1)

Data sets taken on different sources at different times show very good agreements in the beam profile shapes. This is valid within the apertures sizes, as shown in the plots on a linear scale, as well as beyond, as shown in the plots on a logarithmic scale for which the profile is measured over 3 orders of magnitudes. The profiles are seen to be quite narrow toward the peak, with a somewhat triangular shape along the Y-axis, expecially remarkable for Band 1, for which a $4''$ offset w.r.t. the peak results in about 20% signal loss. For the other bands, the Z-direction (the shortest side of the slit) is the most sensitive to small pointing offsets, giving rise to inaccuracies of the absolute flux level of the order of 30% at the longests wavelengths.

The pointing reconstruction algorithm applied to early mission data sets give pointing offsets ranging from around $-3''$ to $3''$ in both Y and Z direction, and it is remarkable that when corrected for those offsets, all profile centres tend to concentrate towards consistent values. Detector band to band offsets clearly appear from all these measurements. As a given target cannot therefore be centred exactly for all detector bands, signal losses due to the narrow beam profiles arise. For some bands, small pointing offsets can have an amplified effect on the absolute photometric level. The exact determination of these signal losses and band to band offsets has been attempted in the course of the mission, however no proper fitting/interpolation routine could been found, to successfully allow on the peaked beam profiles for an accurate determination of the centroid and therefore of the true peak signal. The availability of a proper model of the beam profile in SIA made this possible in the Post Operation Phase.

6.3.10 Beam Profile Wavelength Dependency

The AOT1 exercises can be used for the characterisation of the beam profile wavelength dependence within an AOT band. This is done by fitting a first order polynomial the flux (in Jy) as a function of wavelength.

Only Band 2C clearly showed a clear dependance of the fit parameters on the offset from the target (HR5340 – Figure 6.14, or NML-CYG). This is unlikely to be caused by memory effects, as the down scan only has been used in the reduction and also because the pattern is symmetric around the target. More likely it is due to the large wavelength range covered by this AOT band.

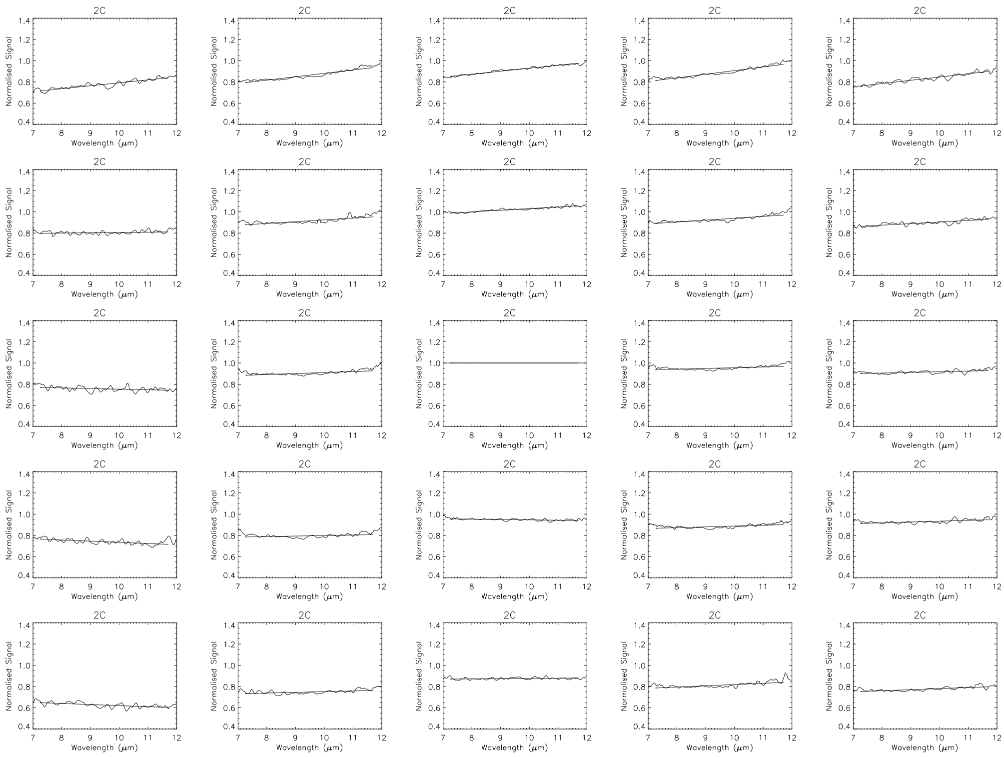

Figure 6.14: Pointing effects on the spectrum in band 2C, as evidence for wavelength dependance of the beam profile, as obtained from the REV 640 AOT1-like 5X5 raster centred on HR5340. Each box shows the ratio of the spectrum to the centre position. Each box correspond to one raster point, separated by the adiacent ones by 2″. Y increases from left to right and Z increases from top to bottom.

The average signals across each AOT bands are shown in Figure 6.15 for the HR5340 experiment and Figure 6.16 for the NML-CYG experiment. The HR6705 experiment is shown in Figure 6.17. The sections along the Z-axis around the targets are overplotted onto the HR1457 experiment in Figure 6.18. In here the HR6705 set has been shifted by the amount given by the pointing reconstruction algorithm, 1.3″. The agreement between these different data sets is almost perfect. It is apparent that this could be even better understood if account is taken of the ISO pointing accuracy, 1.5″ 2-sigma, half cone. In fact, best agreement for the data sets on HR5340 and NML CYG can be reached by shifting each other by 1″ along the Y axis and -2″ along the Z axis.

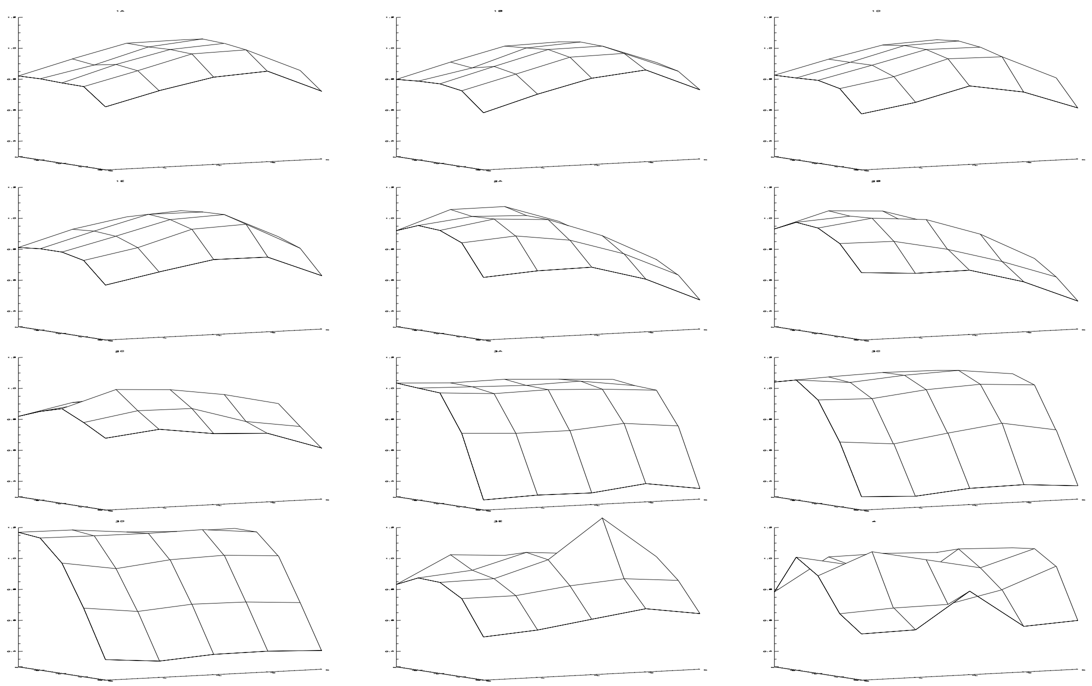

Figure 6.15: The top (+/- 4″ box) of the beam profiles for each grating AOT band is shown as resulting from the average signal across each AOT band of the 5X5 CUS raster experiment on HR5340 performed in REV 640. The profiles are normalised to the centre position, corresponding to HR5340 itself. The AOT bands go in increasing wavelengths from left to right and from top to bottom. The s/c Y-axis increases from -4″ to 4″ in steps of 2″ from left to right. The s/c Z-axis increases from -4″ to 4″ in steps of 2″ in the direction towards the plot. The normalised vertical scale goes from 0.3 to 1.2 in steps of 0.2. The top of the profile appears to depend mainly on the detector band used, and not on the aperture used, confirming the FPG calibration.

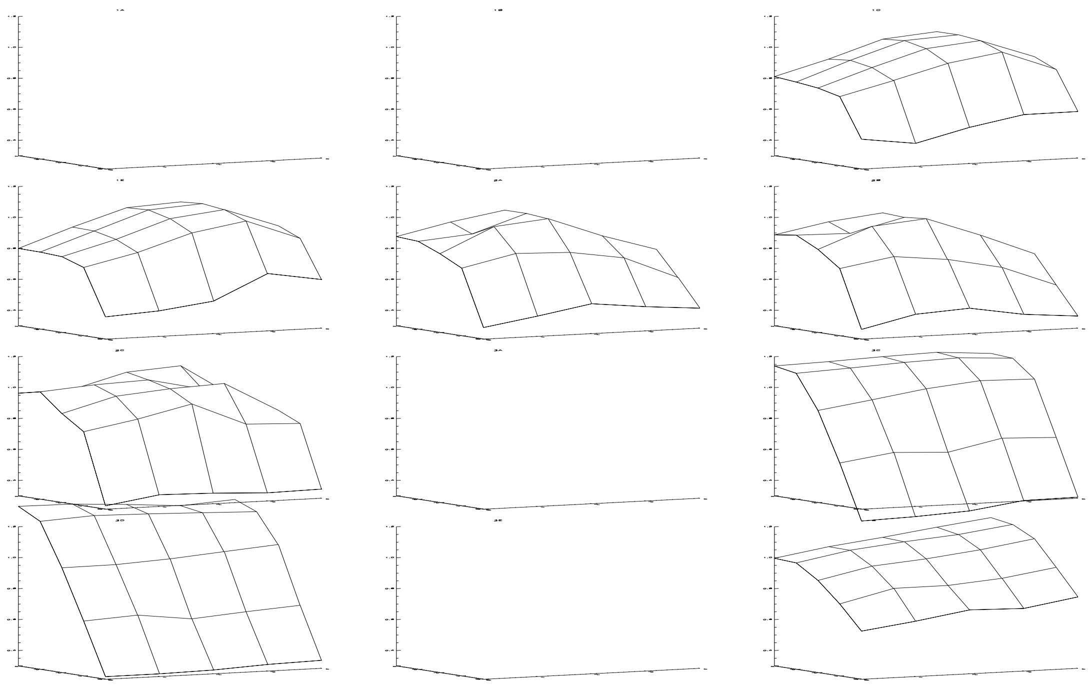

Figure 6.16: The top (+/- 4″ box) of the beam profiles for grating AOT bands is shown as resulting from the average signal across each AOT band of the 5X5 CUS raster experiment on NML-CYG, performed in REV 742. The profiles are normalised to the centre position, corresponding to HR5340 itself. The AOT bands go in increasing wavelengths from left to right and from top to bottom. The s/c Y-axis increases from -4″ to 4″ in steps of 2 arcsec from left to right. The s/c Z-axis increases from -4″ to 4″ in steps of 2 arcsec in the direction towards the plot. The normalised vertical scale goes from 0.3 to 1.2 in steps of 0.2. Aperture 2,3 and 4 were used for this experiment, so the AOT bands making use of Aperture 1 do not appear. Profiles are very similar to the ones obtained on HR5340.

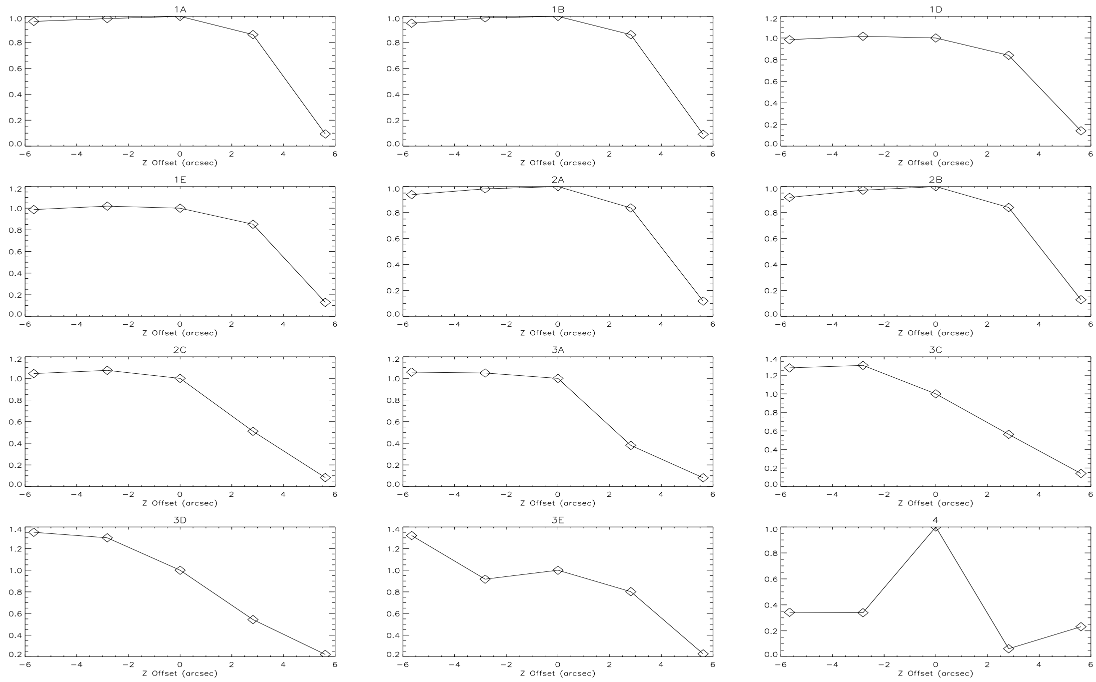

Figure 6.17: Beam profiles along the Z axis for each grating AOT band as resulting by averaging the signals over each AOT band from the AOT1's map performed on HR6705 in REV126.

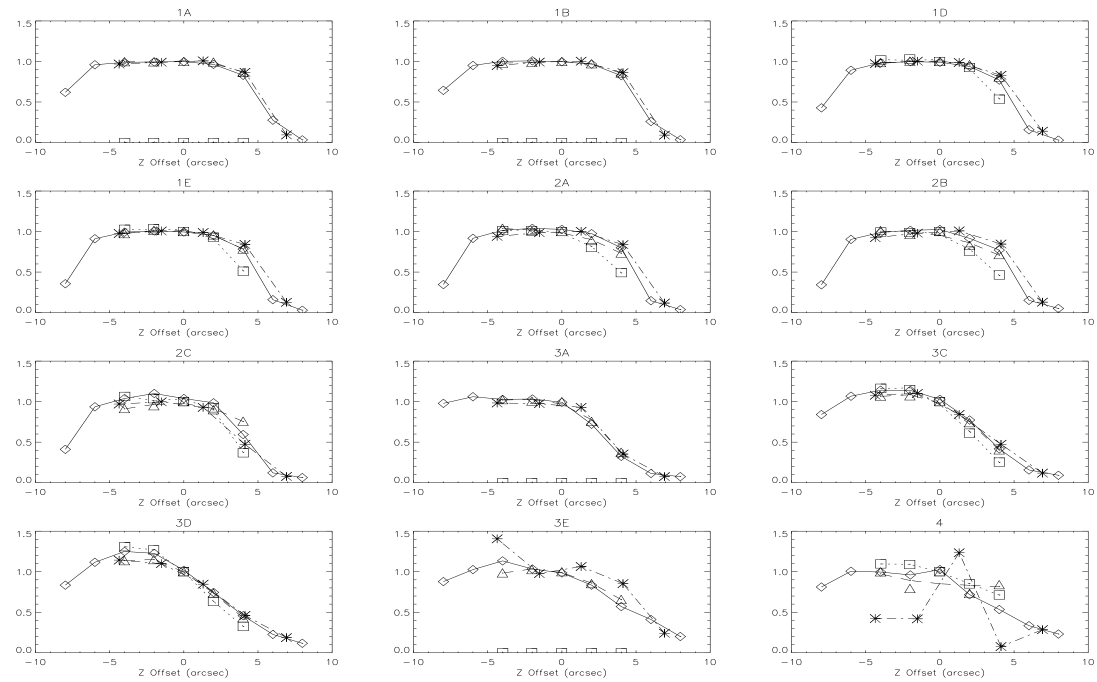

Figure 6.18: Beam profiles along the Z-axis obtained by various AOT1 (like) exercises are shown here. The HR6705 data are represnted by asterisks, the HR5340 data by triangles, the NML-CYG data by squares. The data obtained with the raster done on HR1457 in REV 860 is shown with romboids. The agreement between these different data sets is promising. Only the REV126 HR6705 data set has been shifted by the known pointing offset of 1.3″.

6.4 The SWS beam profile model

The SWS beam profile model is based on a wavefront propagation model of the telescope and the SWS instrument, in combination with phenomenological models of the Y profiles of the detectors. The detector models have been constructed to provide a good fit to the beamprofiles observed in calibration observations (see chapter 6.5). The wavefront model uses an idealised telescope and an SWS consisting only of the elements shown in Figure 6.1.

The observational evidence is really needed in the model, since the Y profiles depend on detector projections through long and imperfect optical chains. Ground calibration could provide only very coarse mapping of the instrument profile.

Only a single profile per detector band is required to provide a reasonable fit over the entire wavelength range of that band. This validates the approach taken.

The SWS beam profle model, including the phenomenological detector models, is contained in the SWS IA module SWS_DIFFR_BEAM.

6.4.1 The telescope pupil

The assumed telescope pupil has a primary mirror with an effective diameter of 60 cm, and a central obscuration diameter of 17.4 cm. Additional obscuration is caused by three mirror support struts with a thickness of 2.0 cm. These data were obtained from the ISO alignment plan (ref [18]) and from the ISO Scientific Capabilities Document (ref [19]). All obscuring elements are assumed to be in the same pupil plane, which allows to compute a telescope point-spread function (PSF) by a simple Fourier transform.

The telescope model is the same as used for ISOCAM, except for the parallactic shift between the elements, which accounts for the off-axis position of the CAM instrument. SWS decided to ignore the parallax, because its effect on the beam profiles and on the instrument throughput calculation is far too small to be observed with the SWS beam size.

The assumed pupil is illustrated in the first panel of Figure 6.19.

6.4.2 The telescope PSF at the SWS entrance

¿From the telescope pupil, the diffraction image is obtained by applying a Fourier transform. Panels 2 and 3 in figures 6.19 picture the energy distribution in the diffraction spot and the vignetting of the diffraction spot by the slit edges. The energy distribution is equal to the squared amplitude of the field distribution. The field distribution is used for further propagation of the wavefront.

6.4.3 The pupil image near the grating

The second Fourier transform provides us with the field distribution in the pupil plane near the grating. The pupil image is shown in panel 4 of figure 6.19. Note that diffraction by the entrance slit blurs the image in the Z direction. Only one spider leg, perpendicular to the slit orientation, is still visible.

Panel 5 shows the SWS pupil image, vignetted by the pupil limits imposed by the geometry of the collimator optics, the scan mirror and the grating. The subsequent blurring and vignetting results in a nearly rectangular pupil image.

As with the telescope pupil, we use the approximation that all edges limiting the beam are situated in a single plane that co-incides with the pupil image. As a further approximation, offsets

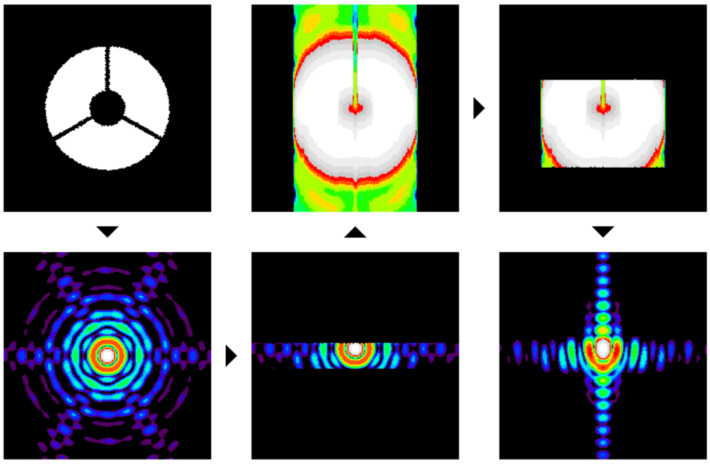

Figure 6.19: *Wavefront propagation from the telescope pupil to the detector image plane. The panel sequence is indicated by arrows between the panels. The sequence applies to a monochromatic point source, at a wavelength of 14 μm, positioned 4″ off the slit center.*

of the individual detectors and entrance slits from the nominal optical axis were ignored. The pupil limits depend strongly on the scan mirror orientation, which is a function of wavelength. Figure 6.20 demonstrates this dependence. As was explained in the introduction of chapter 6, the vignetting of the collimated beam was increased significantly by a design change required to prevent spectral ghosts.

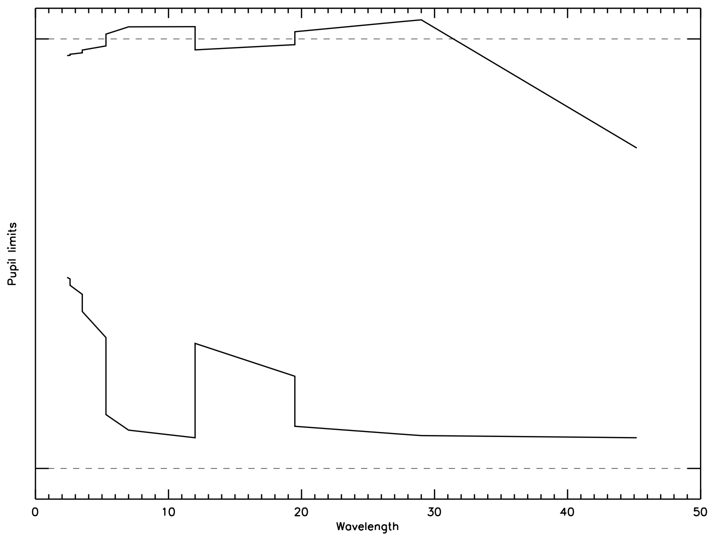

Figure 6.20: *Internal pupil limits as a function of wavelength. The dashed lines indicate the limits of the geometrical pupil image.*

6.4.4 The diffraction-controlled spectral image

The Fourier transform of the field distribution in the pupil plane provides us with the idealised distribution of the field in the spectral image, for a monochromatic point source. The energy distribution is shown in Figure 6.19, panel 6. The rectangular pupil shape cause a cross-like diffraction pattern. This concludes the diffraction calculation; the remaining analysis starts from this energy profile.

The projection of the spectral image onto the detectors

The diffraction calculation applies to monochromatic radiation of a point source. To calculate the response to a continuum source, the energy profile has to be integrated in the dispersion (Z) direction. For the grating detectors the integration extends over the full width of the calculated diffraction image. For the FP detectors the situation is different: the Fabry-Perot etalons, which effectively act as monochromators. Hence the integration in the dispersion direction is limited to the size of the single detector. This is only an approximation, because towards the edges of the detector the transmission of the Fabry-Perot at the monochromatic wavelength is somewhat reduced. The full computation is too involved and is not supported by beam-profile measurements on emission-line sources.

In the Y direction, parallel to the slit edges, the distribution has to be convolved with the profile of the detector. In addition, we have to account somehow for blurring due to optical aberrations and possible de-focussing problems (in the dispersion direction, no blurring was detectable and blurring detctedsuch blurring will have very little effect (it will affect the spectral resolution!). But in the other direction the beam profile will be affected in comparable degrees by diffraction, by detector geometry and by optical aberrations. We have chosen for a practical approach: we assume that we may describe the resulting beam profile by a convolution of the diffraction image with a geometrically blurred detector profile. This blurred detector profile is an unknown, which had to be retrieved from the beam profile observations.

The blur model produces results that are consistent with the observations (see chapter 6.5). For each of the detector arrays in SWS we can match the observed cross-dispersion beam profiles at all wavelengths with a single blurred-detector profile in combination with the predicted wavelength- proportional diffraction profile. The required detector blurs are significant in bands 1 and 2, where almost triangular beam-profile sections are observed. The geometrical blur profiles are plotted in Figure /refsws:detyprofiles.

The outcome of the blur step is an estimate of the effective throughput of the spectrometer for a given wavelength and a given position with respect to the slit edges, as a function of source position along the slit.

For the Fabry-Perot channels we have no sufficiently reliable dat to derive a blur model for the detectors. Instead we used a rectangular detector profile with the nominal dimension, consistent with Table 6.1

The geometrical Y profiles used for the 6 detector bands are depicted in Figure 6.21.

Beam profile

The steps outlined above result in a beam profile perpendicular to the dispersion direction. To obtain a full two-dimensional beam profile, the calculations have to be repeated for a large number of point-source positions across the slit. Figure 6.22 shows a central cut through the beam profile, together with the slit profile used. It demonstrates the narrowing of the (external) beam due to internal refraction.

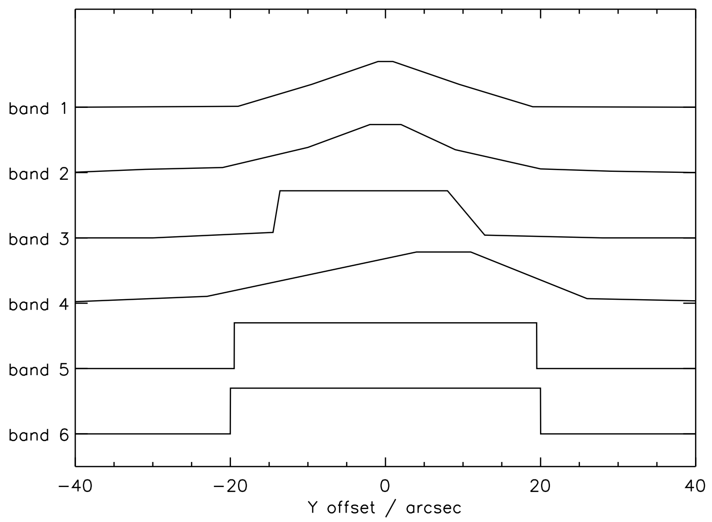

Figure 6.21: *Geometrical Y profiles used for the different detector arrays.*

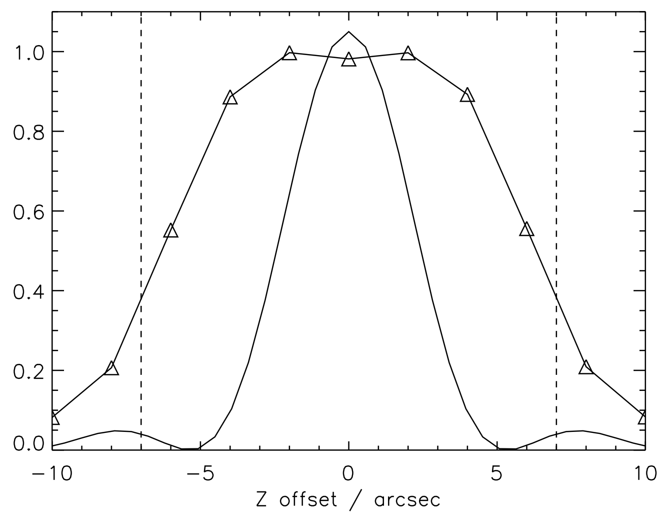

Figure 6.22: *A central Z cut through the calculated beam profile at 14 μm, together with the telescope PSF. Dashed lines mark the edges of the entrance slit.*

6.4.5 Implementation issues

Calculating a single beam profile requires on the order of 100 to 200 Fourier transforms on large two-dimensional arrays. Even with 1024-by-1024 arrays, the sampling of the pupil planes and the image planes remains marginal. It is difficult to obtain enough sampling on the spider legs (2 samples per leg width is the norm). Half of the energy intercepted by the smallest structures is relayed to the far field of the beam profile and it proves difficult to predict the far field with a precision larger then 10overcome the problems of limited sampling density, we tried several stratagems, that were not very successful. One was to apply some smoothing on the distributions to be sampled, to allow interpolation. But smoothing in the field domain is very tricky and causes more problems than it solves. A second strategem was to introduce some random jitter around the edges of pupil and field stops. The effects of that are visible in Figure 6.19. The disadvantage of this procedure is that it produces extra fine structure that translates into noise over the entire field of the transform. It remains essential to use the maximum array sizes that can be afforded in practice.

6.5 The derivation of the SWS Beam Profile Calibration Files

The beam profile measurements were used to derive two types of calibration files, one for pointing and jitter correction and one for extended sources correction.

6.5.1 Observations

Combining different observations at the same wavelength, an empirical beam profile calibration file could be built, using the pointing reconstruction algorithm included in the pipeline processing.

But in any case, this correction is not enough, since all these observations are still subject to the ISO pointing accuracy. In order to minimize these random errors, all the observations were cross-correlated with respect to a reference one, chosen for its high flux level and fine spatial sampling. For most of the bands, more than one reference observation could be used, so that we could verify the goodness of the cross-correlation process, which was better than $0.5''$ in most of the cases.

Tables 6.2 to 6.4 give an overview of the measurements used. Figures 6.23 to 6.26 show the result of the combination of all the available observations after shifting them with respect to the reference one for each band and in each y and z axis.

TDT	LVDT	BAND 1	BAND 2	BAND 3	BAND 4	BAND 5	BAND 6
02401301	1150		7.69		40.01		39.54
02401301	200	2.87	13.99	13.78			
02401301	500	3.08	4.67	17.00		16.80	
02401301	700		5.88	19.97		19.53	
02401301	900		13.01		44.51		44.07
02401402	100		7.69		40.01		39.54
02401402	1000	2.87	13.99	13.78			
02401402	1200						
02401402	300		13.01		44.51		44.07
02401402	600	3.08	4.67	17.00		16.80	
02401402	800		5.88	19.97		19.53	
03600801	1100		7.69		40.01		39.54
03600801	1400		11.01	28.49	28.77		28.25
03600801	200	2.87	13.99	13.78			
03600801	500	3.08	4.67	17.00		16.80	
03600801	800	0.00	5.88	19.97		19.53	
03600902	1000		5.88	19.97		19.53	
03600902	1300	2.87	13.99	13.78			
03600902	200		11.01	28.49	28.77		28.25
03600902	500		7.69		40.01		39.54
03600902	800	3.08	4.67	17.00		16.80	
03602301	1100		7.69		40.01		39.54
03602301	1400		11.01	28.49	28.77		28.25
03602301	200	2.87		13.99		13.78	
03602301	500	3.08	4.67	17.00		16.80	
03602301	900		5.88	19.97		19.53	
03602402	1000		5.88	19.97		19.53	
03602402	1300	2.87		13.99		13.78	
03602402	200		11.01	28.49	28.77		28.25
03602402	500		7.69		40.01		39.54
03602402	700	3.08	4.67	17.00		16.80	
04003102	200	3.08	4.67	17.00		16.80	

Table 6.2: Summary of the observations used for the determination of the SWS beam profile. In each column we indicate the fixed wavelength observed for each AOT band.

TDT	LVDT	BAND 1	BAND 2	BAND 3	BAND 4	BAND 5	BAND 6
04400801	1200		7.69		40.01		39.56
04400801	1600		11.01	28.49	28.77		28.26
04400801	300	3.08	4.67	17.00		16.80	
04400801	700		5.88	19.97		19.53	
04400902	1100		5.88	19.97		19.53	
04400902	200		11.01	28.49	28.77		28.26
04400902	500		7.69		40.01		39.56
04400902	800	3.08	4.67	17.00		16.80	
04801101	1500	2.83		14.38		14.17	
04801201	1500	3.08	4.67	17.17		16.97	
04801301	1000		7.69		30.89		30.39
05600201	1000		7.69		30.89		30.39
06000401	2000	2.83		13.99		13.78	
06000501	2000	3.08	4.67	17.00		16.79	
06000501	5000		5.88	19.97		19.53	
06000701	2000		11.01	28.49	28.77		28.27
06000701	5000		7.69		40.01		39.56

Table 6.3: Summary of the observations used for the determination of the SWS beam profile. In each column we indicate the fixed wavelength observed for each AOT band.

TDT
12601117
12601216
12601315
12601418
12601519
12601620
12601721
24402462
24402563
24402664
24402765
24402866
24402967
24403068
24403169
24403270
24403371
24403472
64000101
64000202
64000303
64100101
64100202
64100303
64100404
74200101
74200202
74200303
86002401
86002502
86002603

Table 6.4: Summary of the AOT1 like observations used for the determination of the SWS beam profile. They cover the whole AOT band, as a normal AOT1.

6.5.2 The relation between the SWS Beam profile model and the observations

Due to the scatter in the big set of points obtained after the combination of all the observations, it was decided to build the calibration file with a theoretical model of the optics of system S/C plus SWS.

In the case of the z direction, the model was derived completely independently of the observations. They agree very well (see Figures 6.23 and 6.24) if we assume that the scatter in the observations is not real and only due to noise in the data.

BAND	Y shift	Z shift
1A	0.0	0.0
1B	0.0	0.0
1D	0.0	0.0
1E	0.0	0.0
2A	0.0	−0.3
2B	−0.7	−0.3
2C	0.1	−0.3
3A	−1.8	−1.8
3C	0.8	−1.8
3D	−1.4	−1.8
3E	6.3	−1.8
4	7.8	−1.6

Table 6.5: Y and Z internal misalignments between AOT bands in arcseconds. They are all computed with respect to BAND 1.

In order to get good agreement between observations and model in the y direction, a detector model for each band had to be introduced, so that the theory is not independent of the data at this point. Again the agreement is good if we consider that the observations are affected by noise.

Furthermore, in order to have consistent calibration files, we needed to add to them information about the internal misalignments of the AOT bands. These were determined empiricaly, making use of observations with good SNR and shape in good agreement with the model. The results statistically obtained are summarised in Table 6.5, and were added to the calibration files coordinates in order to have each AOT band beam peaked at its own position. Since the number of observations is very poor in each case (from 1 in some bands to 5), these parameters still need more finetuning (see section 6.6.1).

Once the models for each AOT band were shifted, a new renormalisation was done in order to have the a relative flux equal to unity at the poistion at which the flux calibration was determined, the $(0, 0)$ position, which is not necessarily coinciding with the peak of the profile for all bands, due to the internal misalignments.

Two calibration files were built based on this theoretical model, each of them with a different purpose:

- The CAL35 file, with a sampling of $0.1''$ and an extension of $\pm 10''$, meant for correction of small mispointing and pointing jitter.
- The CAL36 file, with a sampling of $1.0''$ in a range of $\pm 6'$, meant for extended source correction.

The structure of the calibration files is as follows:

```
——Y<Float>(n)
——Z<Float>(n)
—-MAP<Struct>(14)
                    ————AOTBAND<Strng>(1)
                    ———WAVELENGTH<Float>(1)
                    —————-VALUE<Float>(n*n)
```

The reason to have an array of 14 beams is that each one correspond to a grating AOT band (12 in total), except for bands 2C and 4 which cover a wider range in wavelength so that we have included two values of the beam at separated wavelength for these two bands. As it was mentioned above, the beam are reasonably constant with wavelength all over the band, except in these two bands where the range is wider and the effect of the wavelength is more obvious.

Model and observations do not agree for the FP bands (see figure 6.26), due to leakage at other wavelengths for radiation entering off-axis. The observations by themselves are not enough, nor in spatial sampling neither in quality, to introduce them as part of the calibration file.

Prior to their insertion in the SWS IA, a validation exercise on stars showed that an extra $0.7''$ offset had to be introduced for bands 2C,3A,3C,3D,3E and 4.

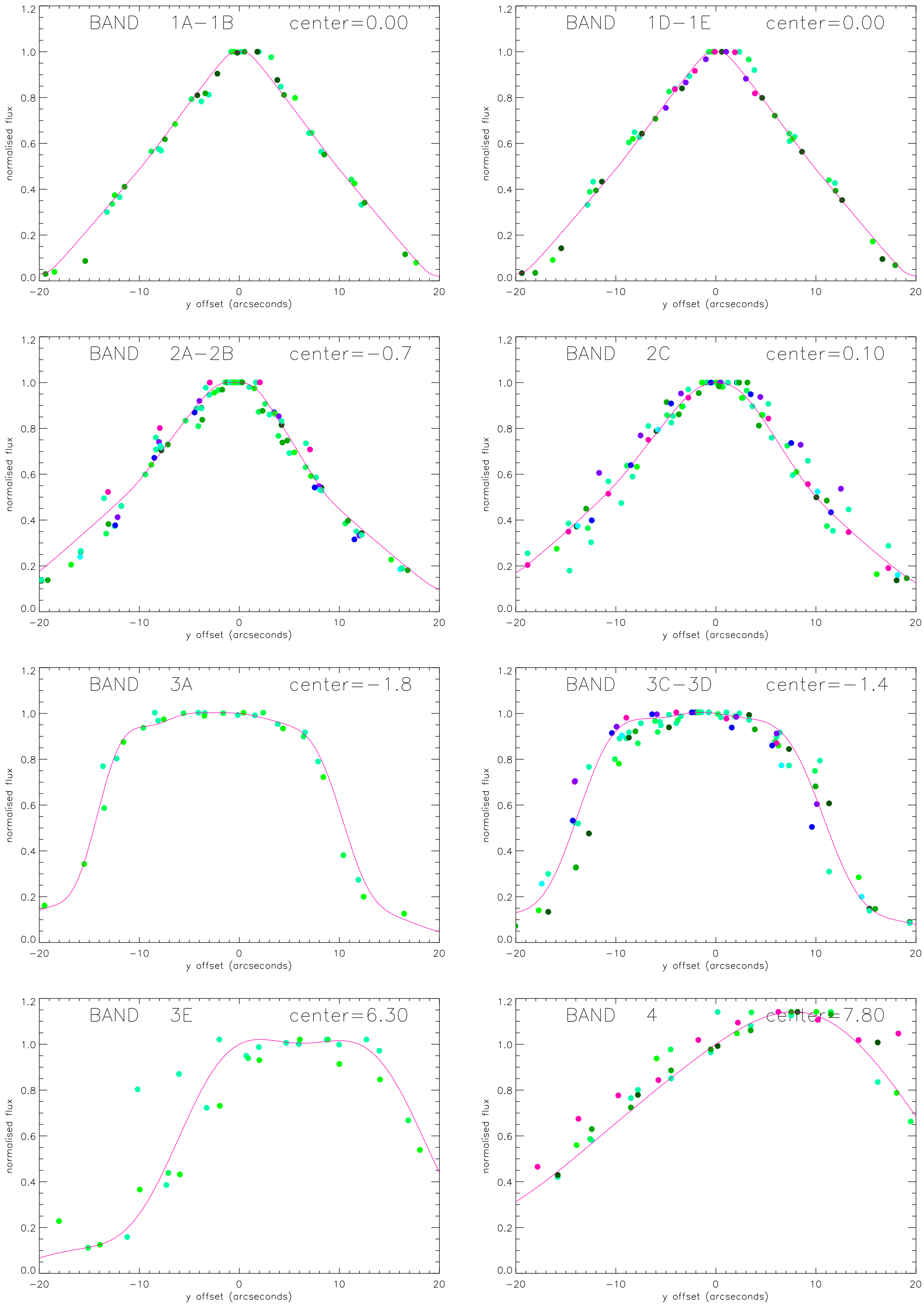

Figure 6.23: Observations (dots) and calibration file (curves) at different AOT bands in both Y and Z axis. Dots with same color correspond to same observation.

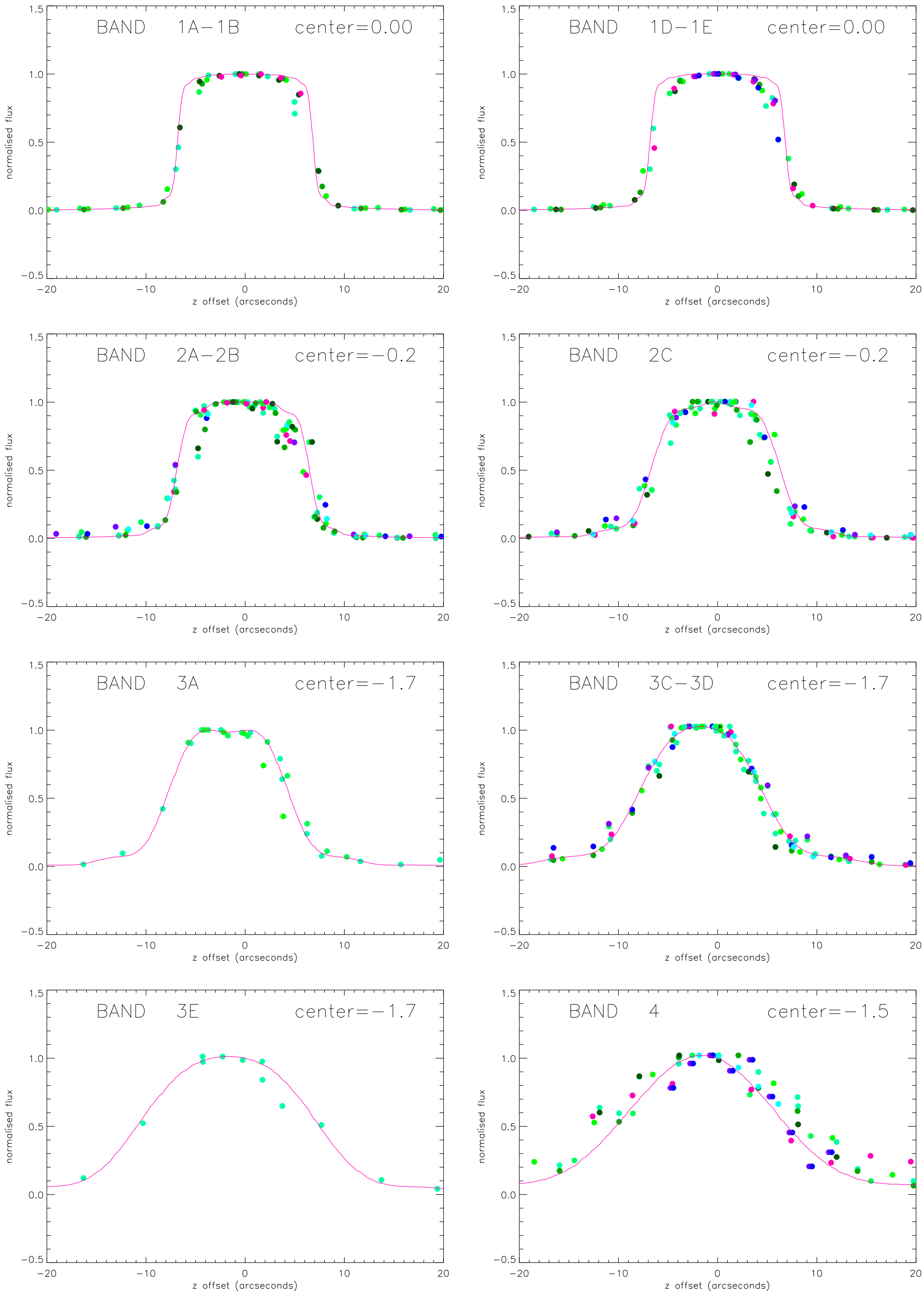

Figure 6.24: Observations (dots) and calibration file (curves) at different AOT bands in both Y and Z axis. Dots with same color correspond to same observation.

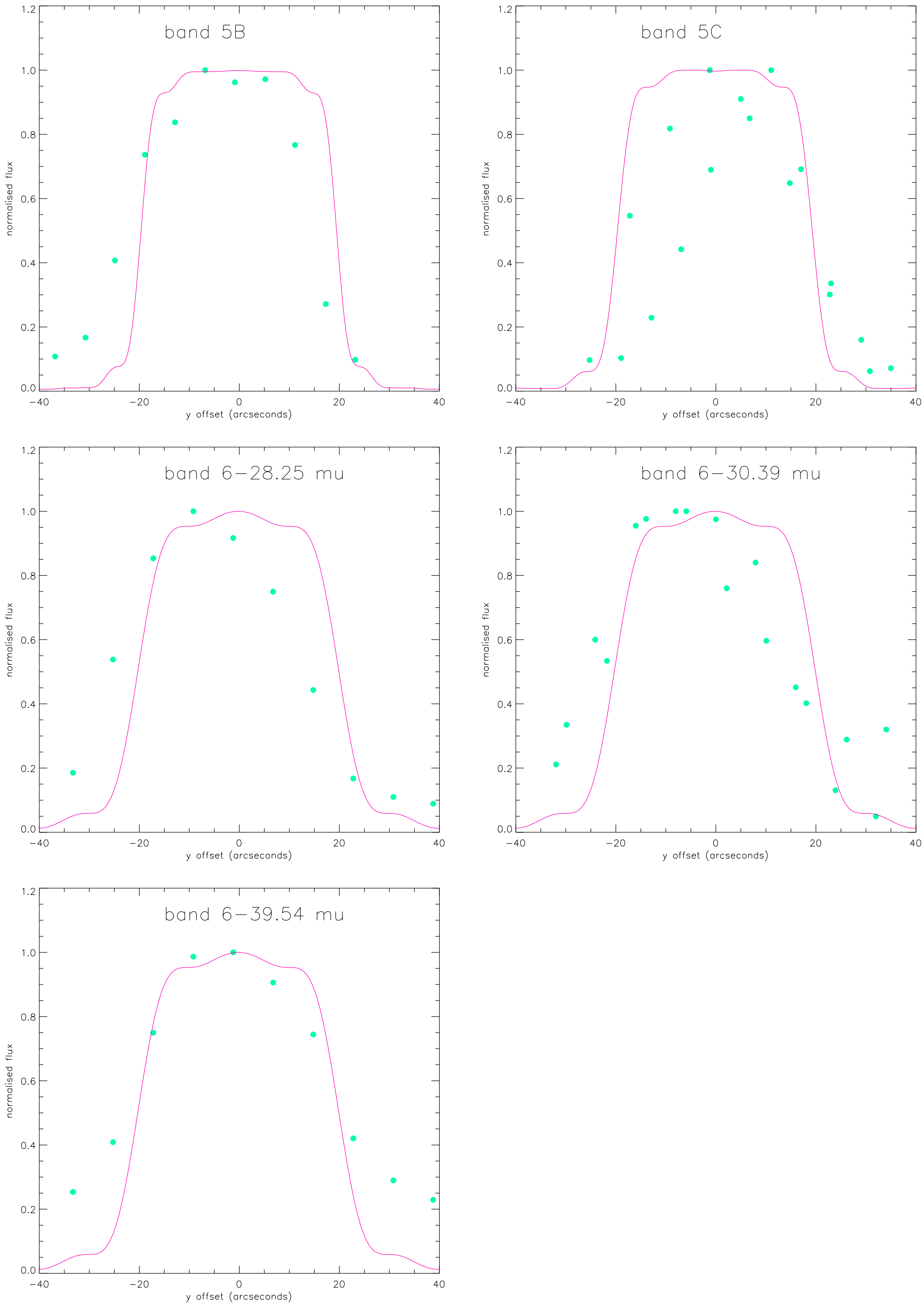

Figure 6.25: Observations (dots) and model (curves) at different FP wavelengths. Dots with same color correspond to same observation.

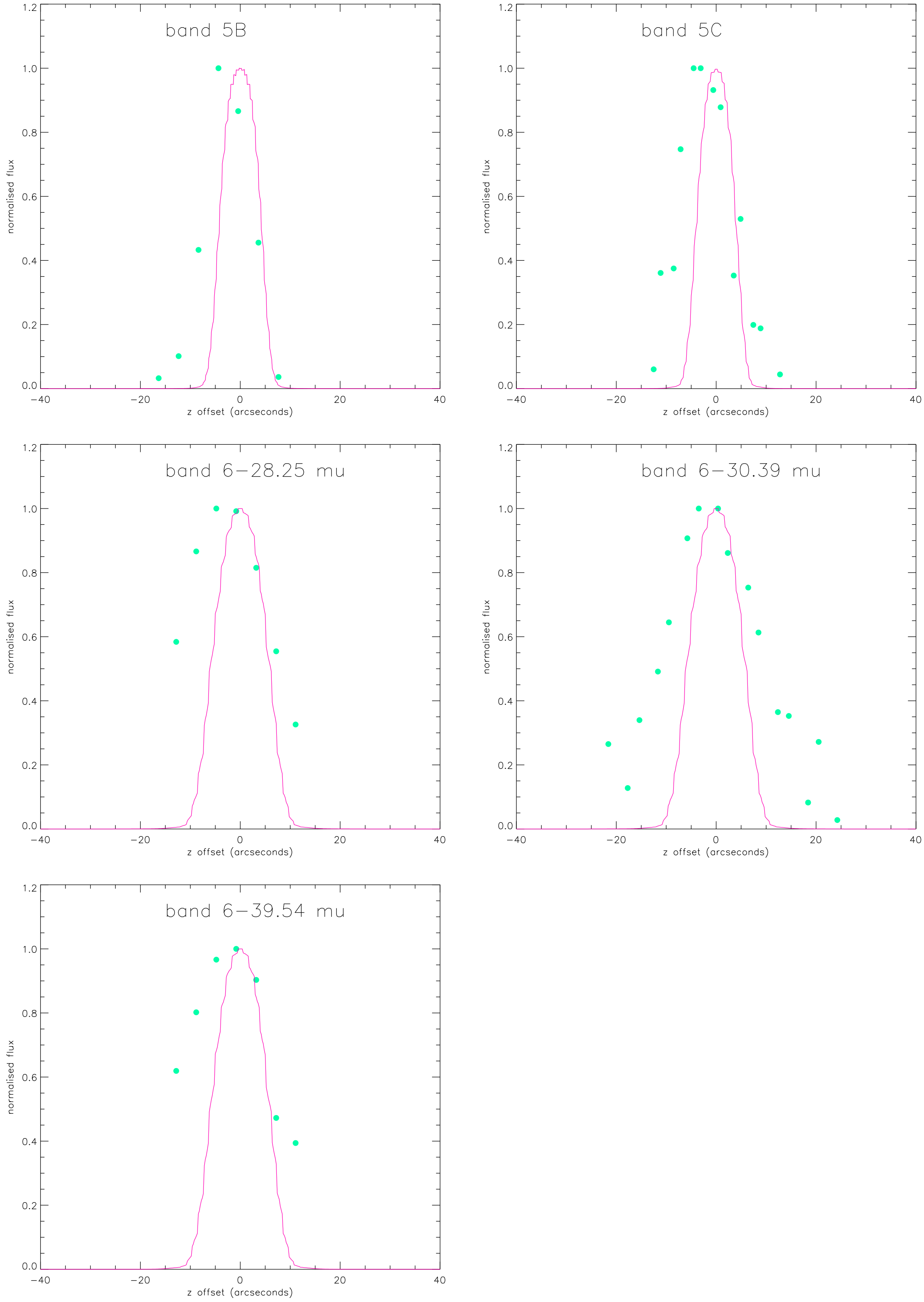

Figure 6.26: Observations (dots) and model (curves) at different FP wavelengths. Dots with same color correspond to same observation. The observed profiles are narrower than the predicted ones. The observations are based on continuum measurements, the predictions apply to narrow spectral lines.

6.6 Pointing induced effects on the SWS data

The narrow and internally misaligned beams, in combination with pointing limitations, affect the flux calibration accuracy of SWS. To a lesser extent, the wavelength calibration is influenced by pointing errors. This section discusses some of the effects seen and ways to correct them.

6.6.1 Pointing/tracking correction tool

A routine is available in the SWS Interactive Analysis (SIA) which corrects the flux associated to each data point of an SWS SPD file by an amount given by the beam profile calibration file, for a given spatial offset. By default, the offset between the commanded and reconstructed coordinates are taken, and the user has the possibility to input extra offsets, as determined for instance by a better knowledge of the source coordinates. AOT band dependent offsets can also be given. An overall validation exercise should allow for a finetuning of the AOT band misalignments, as discussed above. The tool works on the time sampling given by the IIPH pointing file, i.e. 0.5 seconds, therefore allowing for a reduction of the beam profile jitter induced noise. The same tool can directly be used on Solar System Objects (SSO's) observations performed in tracked mode. The ISO-centric ephemerides for all SWS SSO's observations have been inserted in the SIA (as obtained from the JPL facility HORIZON, available from the ISO home page, see the ISO Handbook for details). For each data point, the fluxes are divided by the beam profile value correspondent to the offsets between the reconstructed coordinates present in the IIPH file and the ephemerides. An application of this tool can be seen in Figure6.27, where the removal of the saw-tooth pattern induced by the tracking is evident, with the tool used in default mode.

Initial tests on the asteroids Ceres and Hygiea, (Ref. [17]) show that more finetuning of the band-to-band misalignments is needed, although satisfactory corrections were derived in some cases, as follows:

2A, 2B, 2C, 3A, 3C: tracking correction works fine. Corrects the fluxes towards the model predictions and removes tracking artefacts and features in the spectrum

Band 3E needs additional testing to confirm the offset, in band 4 brighter sources are necessary to avoid dark current problems. Bands 1A, 1B, 1D and 1E have to be tested with off-centre standard stars since the asteroid model predictions are not accurate at this short wavelengths.

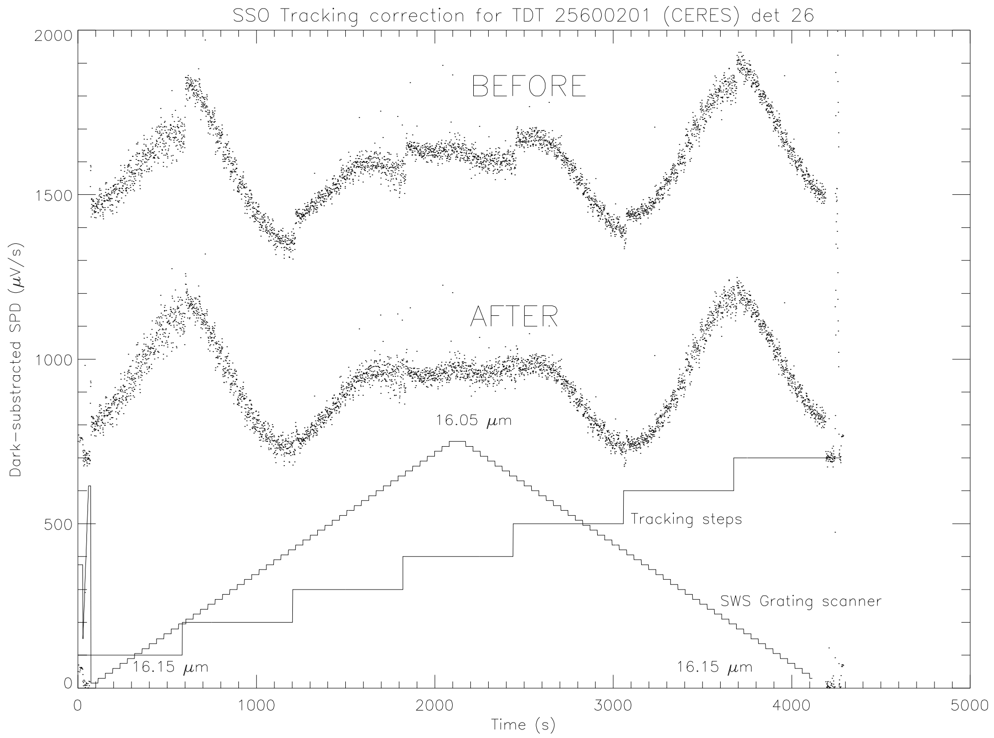

Figure 6.27: Example of tracking correction on SWS data, an SWS AOT 6 on Ceres, Band 3 detector 26. The offsets between the ISO-centric HORIZON ephemerides and the IIPH reconstructed coordinates for this observation amount to up to $4''$. The detector data show the effects of the tracking while Ceres "moves" on a steep part of the SWS beam profile. The fine staircase pattern illustrates the grating up-down scans. The default use of the tracking correction tool in SIA removes the tracking pattern almost entirely.

6.6.2 Pointing effects on fringes

The effect of pointing offsets on the position and intensity of the instrumental fringes, most prominent in AOT band 3A, was characterised with dedicated spectral scans performed at various positions with respect to NML-CYG as illustrated in Figure6.28. The experiments and the associated data analysis results are given in Ref. [11] and [12]. The dependence of the fringe pattern on the pointing also implies that for extended sources or point-like sources off-axis, a perfect correction for the instrumental response function is not possible. The routine RESP_INTER in the SWS Interactive Analysis may be used to interactively check for the optimal correction once the relative response is shifted against the source signal.

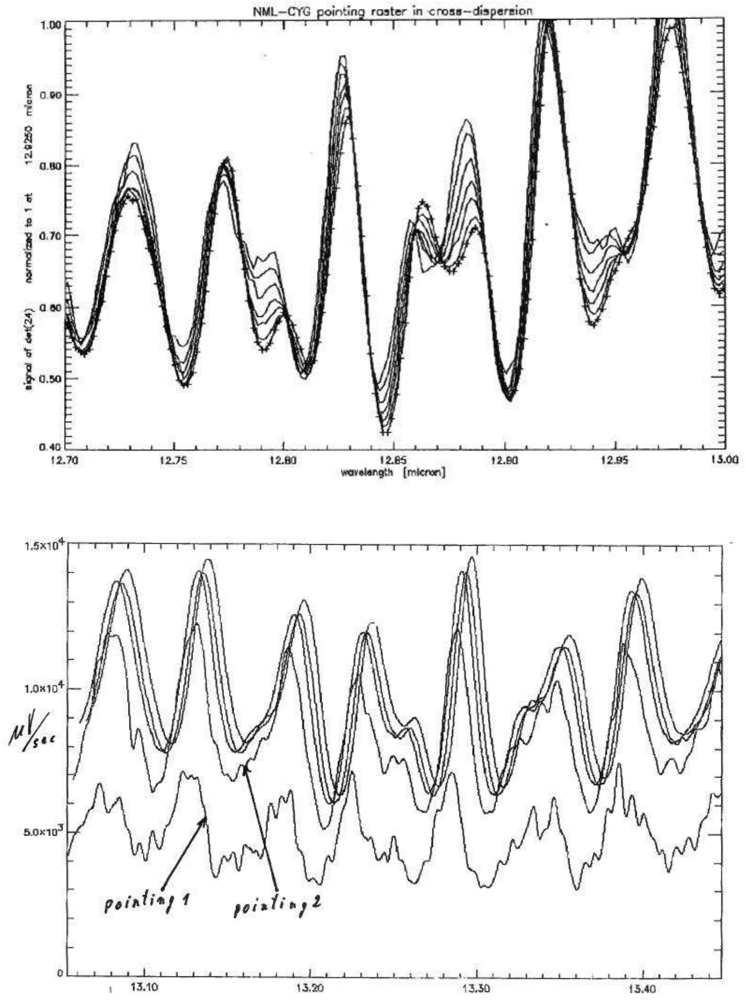

Figure 6.28: *Pointing offset dependence of the fringes seen in detector 26, AOT-band 3A, in cross-dispersion (upper panel) and dispersion (lower panel) directions. Each fringe pattern corresponds to a grating scan performed at positions on the sky separated by 2″ .*

6.6.3 Pointing effects on the Instrumental Line Profile

The effects of pointing offsets on the Instrumental Line Profile has been characterised with a dedicated series of pointing around the bright line-emission and point-like object IC2501 early in PV phase. See Ref. [8] for details on the experiment and its result.

6.6.4 Pointing jitter induced correlated noise

The ISO Pointing jitter is seen by the SWS detectors as the target moves across the beam profile, and results in a detector band correlated noise. This is illustrated in the case of CUS rasters done at fixed grating scanner position, shown in Figures 6.29 and 6.30. For each detector band, the 12 detector elements signals show very similar time behaviour over the time in which the SWS is kept fixed at each raster position, i.e. about 20 seconds. The average jitter across the signal median is clearly following the IIPH time behaviour. This noise is of the order of a few percent of the median flux (peak to peak). This correlated noise is further discussed in Ref. [15] in the case of SWS AOTs, where the correlation between ISO's pointing jitter and jumps in the flux of SWS observations were first studied, with the source DO 24107, which was performed off source because of an error in the input coordinates (+4.7$''$ and -8.6$''$ off in dispersion and cross-dispersion directions respectively). Such a large discrepancy implies that the observation is carried out at a position where the beam profile is very steep. Therefore small oscillations of the pointing around the average position induce large variations of the measured flux. As a consequence of this study it has become apparent that the pointing oscillations are delayed with respect to the flux ones. That is, the best correlation between them is found when 0.7 ± 0.07 seconds (depending on the AOT band) are subtracted from the IIPH UTK. This delay is not as yet completely understood. The routines used in this study have been inserted in the SWS Interactive Analysis. POINT_JITTER requires an SWS AAR and the pointing file IIPH as input and calculates the correlation between the flux and the evolution of dy and dz (oscillation in the Y and Z directions around the average pointing coordinates) for a certain wavelength range. POINT_NOISE calculates the correlation between pointing jitter and noise. Finally, the routine POINT_UP_DOWN provides a tool to check if up-down discrepancies are related to the pointing jitter.

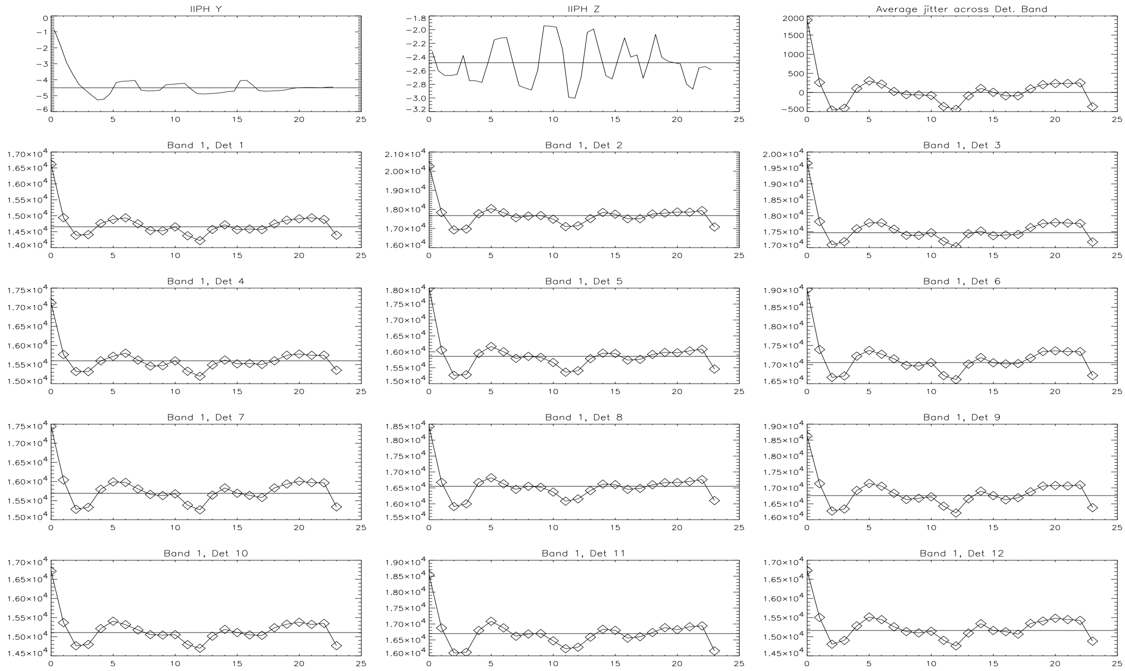

Figure 6.29: Pointing jitter induced correlated noise for Band 1 at 2.8 μm. Data refer to 20 seconds spent on data point m=6, n=6 of the full beam profile characterisation raster 06000401. The upper left panels shown the IIPH behaviour in Y and Z axis respectively. The upper right panel shows the average jitter across the detector band. The other panels show the time behaviour of each of the 12 element detector array signals.

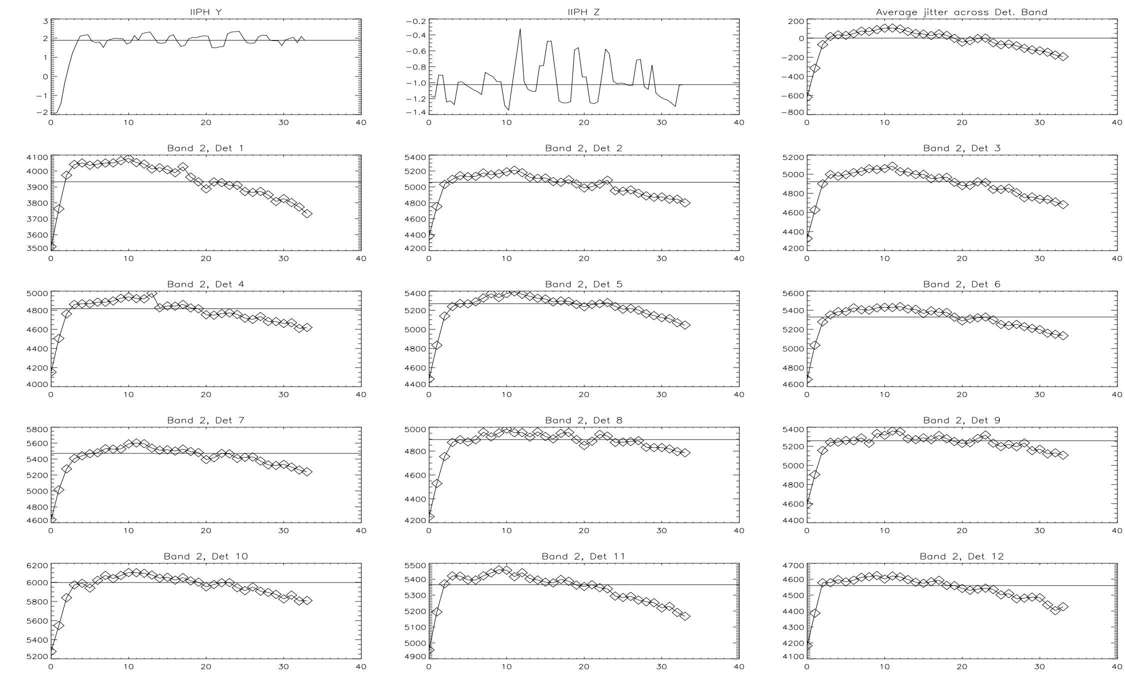

Figure 6.30: Pointing jitter induced correlated noise for Band 2 at 5.9 μ. Data refer to 20 seconds spent on data point m=4, n=1 of the beam profile cross-raster 03602301. The upper left panels shown the IIPH behaviour in Y and Z axis respectively. The upper right panel shows the average jitter across the detector band. The other panels show the time behaviour of each of the 12 element detector array signals.

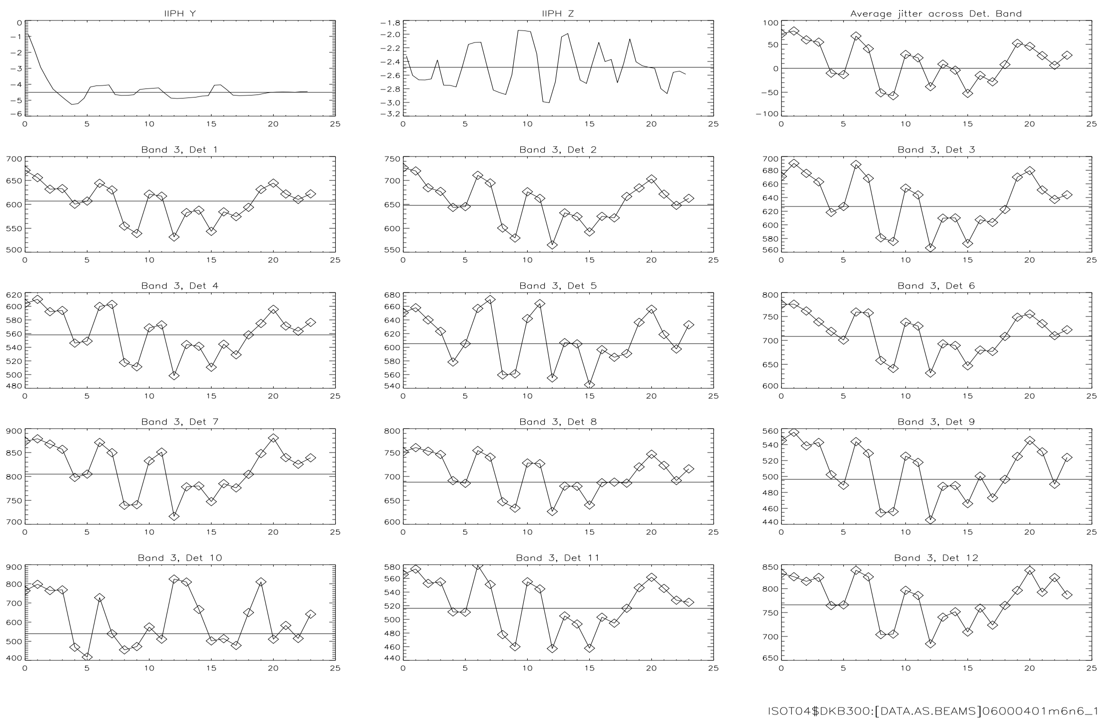

Figure 6.31: Pointing jitter induced correlated noise for Band 3 at 14 μm. Data refer to 20 seconds spent on data point m=6, n=6 of the full beam profile characterisation raster 06000401. The upper left panels shown the IIPH behaviour in Y and Z axis respectively. The upper right panel shows the average jitter across the detector band. The other panels show the time behaviour of each of the 12 element detector array signals.

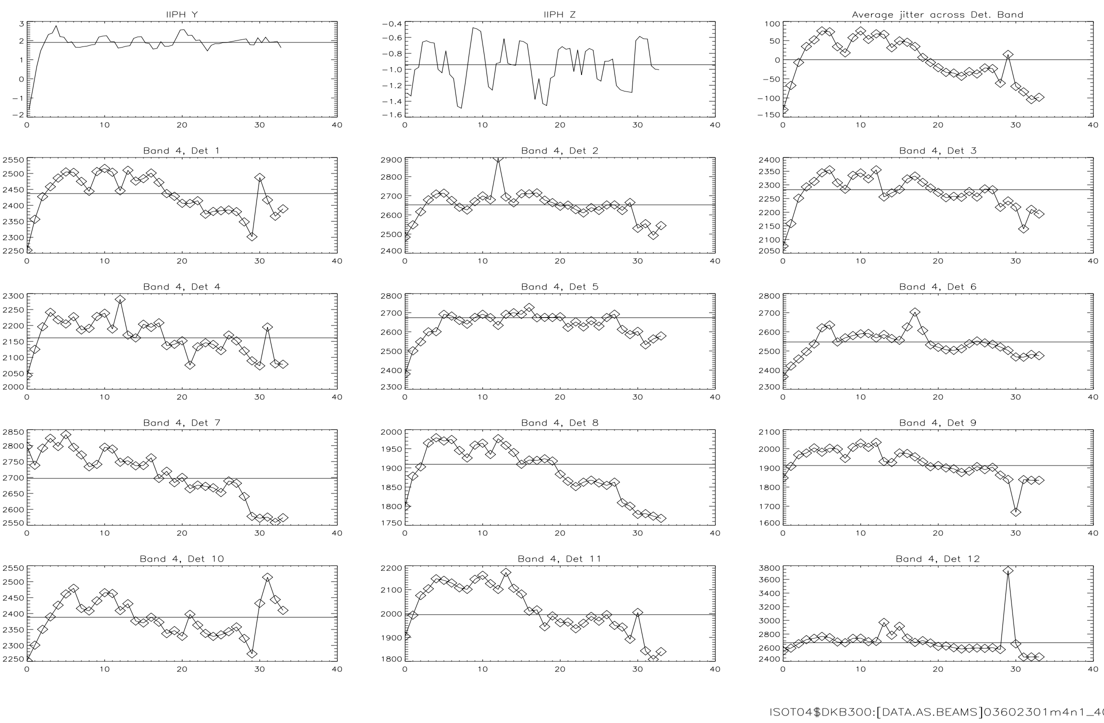

Figure 6.32: Pointing jitter induced correlated noise for Band 4 at 40 μm. Data refer to 20 seconds spent on data point m=4, n=1 of the beam profile cross raster 03602301. The upper left panels shown the IIPH behaviour in Yand Z axis respectively. The upper right panel shows the average jitter across the detector band. The other panels show the time behaviour of each of the 12 element detector array signals.

6.6.5 Signal modulation on Gamma Dra

The SWS Flux Calibration included reproducibility checks on a standard star, HR6705 (Gamma Draconis). A total of 120 observations were carried out on this star starting from REV24 to REV867. These were systematically processed at the end of the mission (in 1998) and the resulting signals were shown to present flux modulations over the mission (see reference [14] for details). Figure 6.33 gives all the derived fluxes within the passbands of the related AOT band versus revolution. Also the three Gam-Dra raster exercises in REV126, REV368 and REV369 are included in this sample, clearly to be seen for example in band 1D. The flux modulations can clearly be seen in 2A,2B,2C,2C$'$,3A,3C, 3D,3E,4A,4D. Band 4 and 4$'$ have too low flux to provide a statement there. No related modulation of comparable amplitude can be seen in band 1. Fluxes are heavily affected by pointing inaccuracies, as can be seen in the period before REV369, when significant pointing errors happened. Also the use of different guidestars with different accuracies are suspect in introducing additional noise in the flux trends. The best explanation, however still not proven so far, for the flux modulation is a systematic pointing error towards Gam-Dra. Band 1 has basically 0 FPG offset, while all the other bands are offset by $2''$-$3''$. This makes bands 2,3,4 sensitive to even small ($1''$) pointing errors, as they are operated close to the edge of the flat top of the SWS beam profile. Band 1 remains rather robust against pointing errors, being centered.

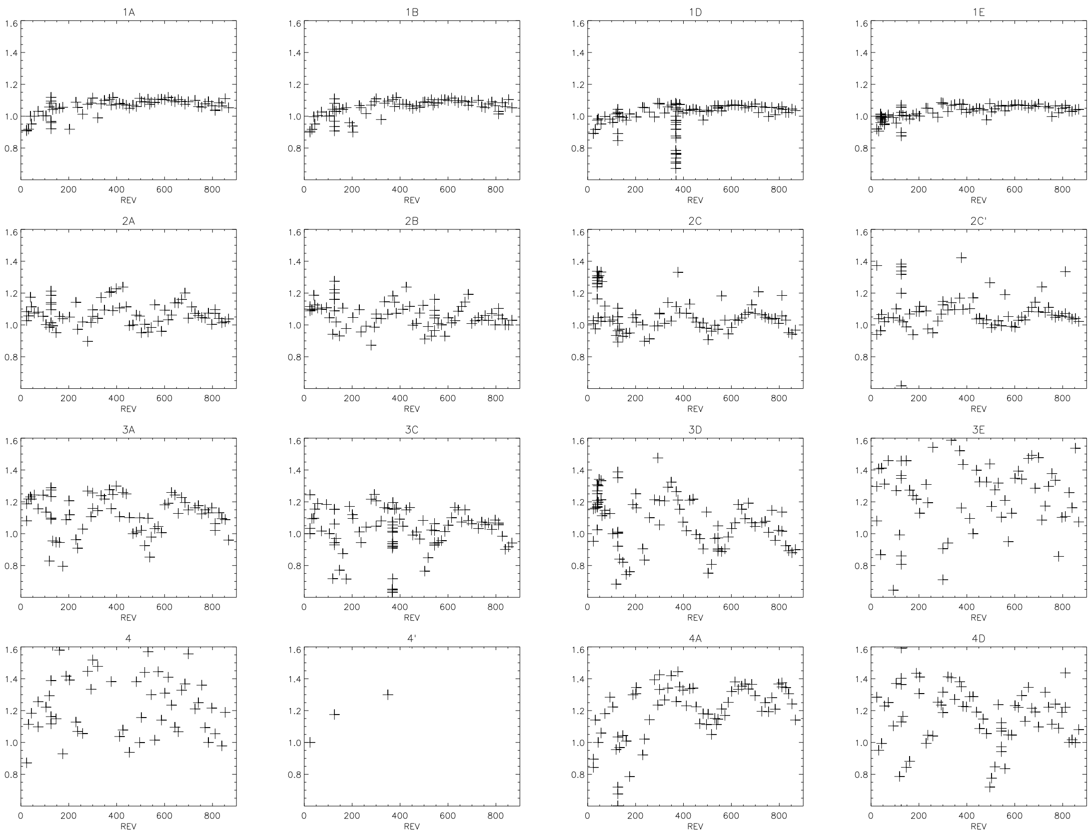

Figure 6.33: *Gamma Draconis fluxes off all passbands vs. revolutions divided by their median. The flux modulations can clearly be seen in the AOT bands 2A,2B,2C,2C$'$,3A,3C, 3D,3E,4A,4D. Band 4 and 4$'$ have too low flux to provide a statement there. No related modulation of comparable amplitude can be seen in band 1.*

6.7 Surface brightness derivation

The flux calibration of the SWS instrument has been derived by positioning well known calibration point-like sources at the nominal centre of the instrument beam. The calibration is therefore directly applicable tor point-source observations only. For extended sources the measured signals have to be converted to brightness values rather than flux values.

To measure the total flux density from a source of arbitrary extent, the general procedure is to map the source and to integrate the signal over the map. It is clear that we can get the right answer by comparing the total with the an integrated map of the point source used to calibrate the instrument (for point sources we use the shortcut of just comparing responses at the beam centre). The scale factor between extended sources and point sources is therefore simply the ratio between the volume and the peak height of the beam profile, or the effective cross section of the beam.

For very large structures, the same relation holds, we can convert the point-source calibrated signal to a brightness value by dividing by the effective beam-profile area.

For smaller sources, we still get a valid calibration by dividing all point-source calibrated signals by the effective beam area, but we must remember that we are then calibrating not the source brightness, but the convolution of the source brightness didtribution with the beam profile.

The derivation of extended source flux from a point source calibration is then given by;

$$[h!]I_\nu = \frac{F_\nu}{\int_{-\infty}^{+\infty} BP(y,z)\, dy dz} \qquad (\mathrm{MJy\,sr^{-1}}) \tag{6.1}$$

where F_ν is the (point-source) flux density at the frequency ν and $BP(y,z)$ is the detector's Beam Profile, normalised to the value at the position in which the flux calibration has been derived, nominally the (0,0) position. The variables y and z are angles with respect to the spacecraft Z and Y axes.

Table 6.6 lists the conversion factors obtained by integrating the normalised beam profiles, according to Equation 6.1.

Table 6.6: *SWS Flux conversion factors for extended sources*

AOT Band	Wavelength (μm)	Jy to $\mathrm{MJy\,sr^{-1}}$
1A	2.48	139
1B	2.87	134
1D	3.08	132
1E	3.8	132
2A	4.7	115
2B	5.9	118
2C	7.7	117
2C′	11	114
3A	14	107
3C	17	105
3D	20	97
3E	28.5	65
4	30.9	45
4′	40	42

6.8 Conclusions and lessons learnt

6.8.1 Instrument analysis

The beam propagation analysis has been very fruitful in analysing SWS properties. This analysis would have been very useful at the time SWS was being designed. In those days we went no further than comparing the theoretical telescope PSF (calculated with Bessel functions) with the geometrical aperture of SWS. That diffraction at the slit edges would broaden our pupil image was beyond our imagination. Probably radio astronomers and microwave engineers would have been quick to point this out. On the other hand, at that time fast Fourier Transforms were not so fast and not so readily available.

Lesson learnt: Expect to keep learning.

6.8.2 Optics design optimalisation

Dispersing spectrometers have the property of mixing up spectral and spatial information. For such instruments a difficult trade-off between spatial resolution, sensitivity and spectral resolution must be made. In the case of SWS, priority was given to achieve maximal spectral resolution and aperture sizes were selected that were not really compatible with the specified pointing performance of the ISO satellite. This was a conscious trade off, where spectral resolution was bought for reduced sensitivity and likely calibration problems due to mis-pointing. Fortunately, it proved possible to improve the pointing to a level that allowed even acceptable absolute spectrophotometry with SWS.

Lesson learnt: It pays to be optimistic about satellite performance.

Lesson learnt: One needs good communication between attitude-control system designers and instrument builders, to be able to trade safety margins against science objectives.

6.8.3 Ground calibration

The internal alignment of the SWS detector arrays and the cross-dispersion optical performance of SWS could not be measured adequately, by lack of point-source simulator in the test equipment. This was a grave limitation which caused some operational and calibration problems during the mission. The limitation has been known from the beginning. At the time that the test equipment was built it did not appear to be possible to include a point-source simulator. Looking back, with the many delays in the ISO project, there might have been time to design and build a reliable point-source simulator.

Lesson learnt: Be critical of your alignment plan.

6.8.4 Operations

Good working relations between the Instrument Team and the Flight Dynamics Group were crucial to improve the ISO pointing performance during the mission.

Lesson learnt: Direct communications between the various parties involved in satellite operations should be encouraged.

6.9 Appendix I: Beam Profile related observations

Focal Plane Geometry Calibration (5 guide stars)

REV	TDT	OSN	RA hh mm ss.ss	AOT	DEC d ' ''	I	time h m s	UTC start	target	m	n	dm	dn	rol	or
012	001	01	17 55 38.99	S99	+51 32 36.8	2	08 53	29 Nov 1995 08 34 45	GAM-DRA	11	11	6	6	0	1
014	008	01	19 34 19.70	S99	+51 14 12.0	2	09 02	01 Dec 1995 10 56 14	GAMMA-DRA	11	11	9	9	0	1
017	001	01	17 55 46.95	S99	+51 31 42.6	2	08 52	04 Dec 1995 08 16 11	GAM-DRA	11	11	6	6	0	1
017	003	01	17 55 46.95	S99	+51 31 42.6	2	08 52	04 Dec 1995 11 40 51	GAM-DRA	11	11	9	9	0	1
017	007	01	17 55 48.16	S99	+51 31 33.1	2	08 52	04 Dec 1995 20 12 33	GAM-DRA	11	11	6	6	0	1
018	001	01	17 55 36.33	S99	+51 31 49.8	2	08 52	05 Dec 1995 08 13 34	GAM-DRA	11	11	4	4	0	1
018	004	01	19 36 13.49	S99	+50 18 19.1	0	30 18	05 Dec 1995 11 46 12	R-CYG	12	2	4	2	129	0
018	005	02	19 36 13.49	S99	+50 18 19.1	0	29 14	05 Dec 1995 12 17 16	R-CYG	12	2	3	2	39	0
018	006	03	19 36 13.49	S99	+50 18 19.1	0	30 18	05 Dec 1995 12 53 44	R-CYG	12	2	4	2	129	0
018	007	04	19 36 13.49	S99	+50 18 19.1	0	29 14	05 Dec 1995 13 24 48	R-CYG	12	2	3	2	39	0
018	008	05	19 36 49.39	S99	+50 11 59.5	0	30 18	05 Dec 1995 13 59 18	R-CYG	12	2	4	2	129	0
018	009	06	19 36 49.39	S99	+50 11 59.5	0	30 48	05 Dec 1995 14 30 22	R-CYG	12	2	3	2	39	0
018	012	01	19 37 22.30	S99	+50 18 29.9	0	30 18	05 Dec 1995 17 56 12	GAMMA-DRA	12	2	4	2	107	0
018	013	02	17 56 36.40	S99	+51 29 20.3	0	29 14	05 Dec 1995 18 27 16	GAMMA-DRA	12	2	3	2	17	0
018	014	03	17 56 36.40	S99	+51 29 20.3	0	30 18	05 Dec 1995 19 03 16	GAMMA-DRA	12	2	4	2	107	0
018	015	04	17 56 36.40	S99	+51 29 20.3	0	29 14	05 Dec 1995 19 34 20	GAMMA-DRA	12	2	3	2	17	0
018	016	05	17 56 36.40	S99	+51 29 20.2	0	30 18	05 Dec 1995 20 10 20	GAMMA-DRA	12	2	4	2	107	0
018	017	06	17 56 36.40	S99	+51 29 20.3	0	30 48	05 Dec 1995 20 41 24	GAMMA-DRA	12	2	3	2	17	0
019	001	01	17 29 30.44	S99	+52 21 03.9	0	30 18	06 Dec 1995 08 10 29	BET-DRA	12	2	4	2	100	0
019	002	02	17 30 25.99	S99	+52 18 05.0	0	29 14	06 Dec 1995 08 41 33	BET-DRA	12	2	3	2	10	0
019	003	03	17 30 25.99	S99	+52 18 05.0	0	30 18	06 Dec 1995 09 17 33	BET-DRA	12	2	4	2	100	0
019	004	04	17 30 25.99	S99	+52 18 05.0	0	29 14	06 Dec 1995 09 48 37	BET-DRA	12	2	3	2	10	0
019	005	05	17 30 25.99	S99	+52 18 05.0	0	30 18	06 Dec 1995 10 24 37	BET-DRA	12	2	4	2	100	0
019	006	06	17 30 25.99	S99	+52 18 05.0	0	30 48	06 Dec 1995 10 55 41	BET-DRA	12	2	3	2	10	0
019	011	01	17 30 25.99	S99	+52 18 05.0	0	30 18	06 Dec 1995 14 04 27	KSI-DRA	12	2	4	2	105	0
019	012	02	17 53 31.66	S99	+56 52 21.2	0	29 14	06 Dec 1995 14 35 31	KSI-DRA	12	2	3	2	15	0
019	013	03	17 53 31.67	S99	+56 52 21.2	0	30 18	06 Dec 1995 15 16 01	KSI-DRA	12	2	4	2	105	0
019	014	04	17 53 31.66	S99	+56 52 21.2	0	30 48	06 Dec 1995 15 47 05	KSI-DRA	12	2	3	2	15	0
019	019	01	19 12 33.07	S99	+67 39 41.2	0	30 18	06 Dec 1995 18 53 41	DEL-DRA	12	2	4	2	123	0
019	020	02	19 12 33.08	S99	+67 39 41.1	0	29 14	06 Dec 1995 19 24 45	DEL-DRA	12	2	3	2	33	0
019	021	03	19 12 33.07	S99	+67 39 41.2	0	30 18	06 Dec 1995 20 00 45	DEL-DRA	12	2	4	2	123	0
019	022	04	19 12 33.08	S99	+67 39 41.1	0	30 48	06 Dec 1995 20 31 49	DEL-DRA	12	2	3	2	33	0
020	001	01	12 19 11.24	S99	+48 52 19.4	0	30 18	07 Dec 1995 08 07 54	3-CVN	12	2	4	2	30	0
020	002	02	12 19 48.70	S99	+48 59 02.8	0	29 14	07 Dec 1995 08 38 58	3-CVN	12	2	3	2	120	0
020	003	03	12 19 48.70	S99	+48 59 02.8	0	30 18	07 Dec 1995 09 14 58	3-CVN	12	2	4	2	30	0
020	004	04	12 19 48.70	S99	+48 59 02.8	0	29 14	07 Dec 1995 09 46 04	3-CVN	12	2	3	2	120	0
020	005	05	12 19 48.70	S99	+48 59 02.8	0	30 18	07 Dec 1995 10 21 04	3-CVN	12	2	4	2	30	0
020	006	06	12 19 48.70	S99	+48 59 02.8	0	30 48	07 Dec 1995 10 52 08	3-CVN	12	2	3	2	120	0
020	011	01	12 19 48.70	S99	+48 59 02.8	0	30 18	07 Dec 1995 14 02 18	CF-BOO	12	2	4	2	52	0
020	012	02	14 08 17.32	S99	+49 27 29.0	0	29 14	07 Dec 1995 14 33 22	CF-BOO	12	2	3	2	142	0
020	013	03	14 08 17.32	S99	+49 27 29.0	0	30 18	07 Dec 1995 15 13 40	CF-BOO	12	2	4	2	52	0
020	014	04	14 08 17.32	S99	+49 27 29.0	0	30 48	07 Dec 1995 15 44 44	CF-BOO	12	2	3	2	142	0
020	019	01	14 08 17.32	S02	+49 27 29.1	0	09 36	07 Dec 1995 18 25 54	CF-BOO						
020	020	02	14 08 17.32	S02	+49 27 36.1	0	09 36	07 Dec 1995 18 36 14	CF-BOO-7N						
020	021	03	14 08 16.62	S02	+49 27 29.1	0	09 36	07 Dec 1995 18 46 32	CF-BOO-7E						
020	022	04	14 08 17.32	S02	+49 27 22.1	0	09 36	07 Dec 1995 18 56 52	CF-BOO-7S						
020	023	05	14 08 18.02	S02	+49 27 29.1	0	09 36	07 Dec 1995 19 07 10	CF-BOO-7W						
020	034	01	15 24 55.80	S02	+58 57 57.7	0	09 36	07 Dec 1995 20 11 30	IOT-DRA						
020	035	02	15 24 55.80	S02	+58 57 57.7	0	09 36	07 Dec 1995 20 21 50	IOT-DRA-7N						
020	036	03	15 24 55.80	S02	+58 58 04.7	0	09 36	07 Dec 1995 20 32 08	IOT-DRA-7E						
020	037	04	15 24 55.80	S02	+58 58 04.7	0	09 36	07 Dec 1995 20 42 28	IOT-DRA-7S						
020	038	05	15 24 56.70	S02	+58 57 57.7	0	09 36	07 Dec 1995 20 52 46	IOT-DRA-7W						

Focal Plane Geometry Verification (One Guide Star)

REV	TDT	OSN	RA	AOT	DEC	I time	UTC start	target	m	n	dm	dn	rol	or
			hh mm ss.ss		d ' ''	h m s								
021	005	01	17 56 36.40	S99	+51 29 20.3	0 16 22	08 Dec 1995 08 20 39	GAMMA-DRA	5	5	4	4	0	1
021	006	02	17 56 36.40	S99	+51 29 20.3	0 15 10	08 Dec 1995 08 37 47	GAMMA-DRA	5	5	4	4	0	1
021	007	03	17 56 36.40	S99	+51 29 20.3	0 16 32	08 Dec 1995 08 53 41	GAMMA-DRA	5	5	4	4	0	1

FPG checks via cross-like rasters

REV	TDT	OSN	RA	AOT	DEC	I time	UTC start	target	m	n	dm	dn	rol	or
			hh mm ss.ss		d ' ''	h m s								
024	013	01	17 56 36.40	S99	+51 29 20.3	0 21 16	11 Dec 1995 19 16 58	HR6705	5	1	5	2	0	1
024	014	02	17 56 36.40	S99	+51 29 20.3	0 21 32	11 Dec 1995 19 38 58	HR6705	1	5	2	3	90	1
028	002	01	15 50 46.59	S99	+48 28 58.7	0 21 16	15 Dec 1995 07 22 52	ST-HER	5	1	5	2	74	1
028	003	02	15 50 46.59	S99	+48 28 58.7	0 21 32	15 Dec 1995 07 44 50	ST-HER	1	5	2	3	164	1
032	014	01	15 50 46.59	S99	+48 28 58.7	0 25 06	19 Dec 1995 20 57 39	ST-HER	5	1	5	2	74	1
032	015	02	15 50 46.59	S99	+48 28 58.7	0 25 20	19 Dec 1995 21 23 27	ST-HER	1	5	2	3	164	1
036	008	01	14 15 40.01	S99	+19 11 04.7	0 26 28	23 Dec 1995 11 11 17	HR5340	7	1	4	2	0	1
036	009	02	14 15 40.01	S99	+19 11 04.7	0 26 52	23 Dec 1995 11 38 31	HR5340	1	7	2	6	0	1
036	023	01	20 46 25.50	S99	+40 06 59.4	0 26 30	23 Dec 1995 19 19 37	NML-CYG	7	1	4	2	0	1
036	024	02	20 46 25.50	S99	+40 06 59.4	0 26 54	23 Dec 1995 19 46 51	NML-CYG	1	7	2	6	0	1
040	030	01	20 46 25.50	S99	+40 06 59.4	0 06 46	27 Dec 1995 21 52 29	NML-CYG	7	1	4	2	0	1
040	031	02	20 46 25.50	S99	+40 06 59.4	0 06 58	27 Dec 1995 21 59 59	NML-CYG	1	7	2	6	0	1
044	008	01	10 45 03.60	S99	-59 41 04.3	0 31 20	31 Dec 1995 08 53 03	ETA-CAR	11	1	8	2	0	1
044	009	02	10 45 03.60	S99	-59 41 04.3	0 22 34	31 Dec 1995 09 25 11	ETA-CAR	1	7	2	4	0	1
044	022	01	20 46 25.50	S99	+40 06 59.4	0 14 26	31 Dec 1995 18 34 45	NML-CYG	5	1	5	2	131	0
044	023	02	20 46 25.50	S99	+40 06 59.4	0 14 38	31 Dec 1995 18 49 55	NML-CYG	5	1	2	3	41	0

Beam profile full calibrations

REV	TDT	OSN	RA	AOT	DEC	I time	UTC start	target	m	n	dm	dn	rol	or
			hh mm ss.ss		d ' ''	h m s								
048	011	01	20 46 25.50	S99	+40 06 59.4	0 46 54	04 Jan 1996 17 42 29	NML-CYG	14	11	6	4	0	1
048	012	01	20 46 25.50	S99	+40 06 59.4	0 56 16	04 Jan 1996 18 30 13	NML-CYG	14	9	6	4	0	1
048	013	01	20 46 25.50	S99	+40 06 59.4	0 25 02	04 Jan 1996 19 27 19	NML-CYG	9	8	8	6	0	1
056	002	01	10 45 03.60	S99	-59 41 04.3	0 25 04	12 Jan 1996 06 05 13	ETA-CAR	9	8	8	6	0	1
060	004	01	14 15 40.01	S99	+19 11 04.6	1 02 32	16 Jan 1996 09 59 35	HR5340	13	11	4	4	0	1
060	005	01	14 15 40.01	S99	+19 11 04.6	2 00 44	16 Jan 1996 11 02 57	HR5340	13	11	4	4	0	1
060	007	01	14 15 40.01	S99	+19 11 04.6	1 54 30	16 Jan 1996 13 51 57	HR5340	15	9	4	4	0	1

AOT1 and CUS AOT1-like beam profile calibrations

```
----------------------------------------------------------------------------------------------
REV TDT OSN    RA      AOT      DEC      I time     UTC start          target      m  n dm dn rol or
           hh mm ss.ss        d  '  ''   h  m  s
---|---|--|-----------|-----|-----------|-------|--------------------|----------------------------
126|011|17|17 56 37.01|S01  |+51 29 20.3|0 17 42|22 Mar 1996 05 32 19|HR6705 6-0
126|012|16|17 56 36.71|S01  |+51 29 20.3|0 17 42|22 Mar 1996 05 50 45|HR6705 3-0
126|013|15|17 56 36.41|S01  |+51 29 20.3|0 17 42|22 Mar 1996 06 09 09|HR6705 0-0
126|014|18|17 56 36.11|S01  |+51 29 20.3|0 17 42|22 Mar 1996 06 27 35|HR6705 -3-0
126|015|19|17 56 35.81|S01  |+51 29 20.3|0 17 42|22 Mar 1996 06 45 59|HR6705 -6-0
126|016|20|17 56 36.41|S01  |+51 29 23.3|0 17 42|22 Mar 1996 07 04 25|HR6705 0-3
126|017|21|17 56 36.41|S01  |+51 29 17.3|0 17 42|22 Mar 1996 07 22 49|HR6705 0--3
244|024|62|14 15 40.47|S01  |+19 11 00.6|0 19 00|17 Jul 1996 23 25 08|HR5340_+0_-8
244|025|63|14 15 40.37|S01  |+19 11 01.4|0 19 00|17 Jul 1996 23 44 52|HR5340_+0_-6
244|026|64|14 15 40.27|S01  |+19 11 02.1|0 19 00|18 Jul 1996 00 04 34|HR5340_+0_-4
244|027|65|14 15 40.07|S01  |+19 11 02.9|0 19 00|18 Jul 1996 00 24 18|HR5340_+0_-2
244|028|66|14 15 39.97|S01  |+19 11 03.6|0 19 00|18 Jul 1996 00 44 00|HR5340 ALF-BOO
244|029|67|14 15 39.87|S01  |+19 11 04.4|0 19 00|18 Jul 1996 01 03 44|HR5340_+0_+2
244|030|68|14 15 39.66|S01  |+19 11 05.1|0 19 00|18 Jul 1996 01 23 26|HR5340_+0_+4
244|031|69|14 15 39.57|S01  |+19 11 05.8|0 19 00|18 Jul 1996 01 43 10|HR5340_+0_+6
244|032|70|14 15 39.47|S01  |+19 11 06.6|0 19 00|18 Jul 1996 02 02 52|HR5340_+0_+8
244|033|71|14 15 40.17|S01  |+19 11 11.0|0 19 00|18 Jul 1996 02 22 36|HR5340_+8_+0
244|034|72|14 15 39.77|S01  |+19 10 56.2|0 19 00|18 Jul 1996 02 42 18|HR5340_-8_+0
640|001|01|14 15 39.88|S99  |+19 11 01.4|1 59 22|16 Aug 1997 20 33 12|HR5340      5  5  2  2   0  1
640|002|02|14 15 39.88|S99  |+19 11 01.4|2 46 52|16 Aug 1997 22 33 16|HR5340      5  5  2  2   0  1
640|003|03|14 15 39.88|S99  |+19 11 01.4|2 46 02|17 Aug 1997 01 20 52|HR5340      5  5  2  2   0  1
641|001|01|14 15 39.58|S01  |+19 11 07.0|0 19 00|17 Aug 1997 20 29 53|HR5340 (+0, +7)
641|001|02|14 15 40.58|S01  |+19 11 05.6|0 19 00|17 Aug 1997 20 49 35|HR5340 (+0, -7)
641|001|03|14 15 40.18|S01  |+19 11 16.2|0 19 00|17 Aug 1997 21 09 19|HR5340 (+10, 0)
641|001|04|14 15 39.98|S01  |+19 10 56.4|0 19 00|17 Aug 1997 21 29 01|HR5340 (-10, 0)
742|001|01|19 42 04.10|S99  |+55 27 47.0|2 11 52|26 Nov 1997 14 01 24|NML-CYG     5  5  2  2   0  1
742|002|02|19 42 04.10|S99  |+55 27 47.0|2 11 52|26 Nov 1997 16 13 58|NML-CYG     5  5  2  2   0  1
742|003|03|19 42 04.10|S99  |+55 27 47.0|2 13 32|26 Nov 1997 18 26 34|NML-CYG     5  5  2  2   0  1
860|024|01|04 35 55.19|S99  |+16 30 33.7|1 27 16|24 Mar 1998 18 33 21|HR1457      2  9  2  2   0  1
860|025|02|04 35 55.19|S99  |+16 30 33.7|2 01 27|24 Mar 1998 20 01 21|HR1457      2  9  2  2   0  1
860|026|03|04 35 55.19|S99  |+16 30 33.7|1 58 36|24 Mar 1998 22 03 32|HR1457      2  9  2  2   0  1
---|---|--|-----------|-----|-----------|-------|--------------------|-----------------------------
```

Subarcsecond scale Z-axis beam profile for SSO Tracking Correction

```
----------------------------------------------------------------------------------------------
REV TDT OSN    RA      AOT      DEC      I time     UTC start          target
           hh mm ss.ss        d  '  ''   h  m  s
---|---|--|-----------|-----|-----------|-------|--------------------|-----------------------------
769|002|01|01 18 33.70|S99  |-00 09 42.4|0 13 06|23 Dec 1997 12 41 37|VESTA
769|003|01|01 18 33.90|S99  |-00 09 38.7|0 12 20|23 Dec 1997 12 55 29|VESTA
769|004|01|01 18 34.20|S99  |-00 09 34.9|0 12 20|23 Dec 1997 13 08 49|VESTA
769|005|01|01 18 34.50|S99  |-00 09 31.1|0 12 20|23 Dec 1997 13 22 09|VESTA
769|006|01|01 18 34.70|S99  |-00 09 27.4|0 12 20|23 Dec 1997 13 35 29|VESTA
769|007|01|01 18 35.00|S99  |-00 09 23.6|0 12 20|23 Dec 1997 13 48 49|VESTA
769|008|01|01 18 35.20|S99  |-00 09 19.9|0 12 21|23 Dec 1997 14 02 09|VESTA
769|009|01|01 18 35.50|S99  |-00 09 16.1|0 12 20|23 Dec 1997 14 15 30|VESTA
769|010|01|01 18 35.70|S99  |-00 09 12.4|0 12 20|23 Dec 1997 14 28 50|VESTA
769|011|01|01 18 35.90|S99  |-00 09 08.6|0 12 20|23 Dec 1997 14 42 10|VESTA
769|012|01|01 18 36.20|S99  |-00 09 04.6|0 13 04|23 Dec 1997 14 55 30|VESTA
---|---|--|-----------|-----|-----------|-------|--------------------|-------------------------
```

Straylight checks

```
----------------------------------------------------------------------------------------------
REV TDT OSN    RA      AOT      DEC      I time     UTC start          target      m  n dm dn rol or
           hh mm ss.ss        d  '  ''   h  m  s
---|---|--|-----------|-----|-----------|-------|--------------------|-----------------------------
056|008|01|13 49 02.09|S99  |-28 22 03.0|0 24 56|12 Jan 1996 09 07 37|W-HYA       5  1 60  2   0  1
056|009|02|13 49 02.09|S99  |-28 22 03.0|0 25 18|12 Jan 1996 09 33 25|W-HYA       1  5  2 60  90  1
384|017|67|00 06 28.90|S02  |-01 58 16.1|0 04 04|04 Dec 1996 15 09 27|SATURN/TITAN OFF
384|018|68|00 06 31.60|S02  |-02 00 16.3|0 04 04|04 Dec 1996 15 14 21|SATURN/TITAN OFF
384|019|69|00 06 23.40|S02  |-02 00 42.5|0 04 04|04 Dec 1996 15 19 15|SATURN/TITAN OFF
384|020|70|00 06 21.40|S02  |-02 00 23.4|0 04 02|04 Dec 1996 15 24 07|SATURN/TITAN OFF
```

```
384|021|71|00 06 19.40|S02  |-02 00 04.2|0 04 04|04 Dec 1996 15 28 57|SATURN/TITAN OFF
384|022|72|00 06 19.40|S02  |-02 00 04.1|0 04 04|04 Dec 1996 15 33 43|SATURN
524|004|02|21 24 30.80|S02  |-15 49 44.9|0 48 49|23 Apr 1997 03 44 26|200502 EUROPA
524|005|03|21 24 42.26|S02  |-15 48 45.7|0 06 42|23 Apr 1997 04 34 07|200500 JUPITER
524|043|04|21 24 28.30|S02  |-15 49 55.5|0 48 50|23 Apr 1997 19 08 01|EUROPA-OFF
579|002|02|01 12 42.40|S02  |+05 08 30.6|0 29 16|17 Jun 1997 00 18 09|SATURN-OFF
582|007|06|01 13 38.63|S02  |+05 13 20.2|0 29 16|20 Jun 1997 13 18 51|200606 TITAN
---|---|--|-----------|-----|-----------|-------|--------------------|-------------------------
```

Verification of SCREW 187 implementation (Aperture 4)

```
---------------------------------------------------------------------------------------------------
REV TDT OSN    RA      AOT      DEC      I time     UTC start          target      m  n dm dn rol or
          hh mm ss.ss        d  '  ''   h  m  s
---|---|--|-----------|-----|-----------|-------|--------------------|-----------------------------
161|004|01|20 46 25.50|S99  |+40 06 59.4|0 12 36|26 Apr 1996 01 35 54|NML-CYG     7  3  5  5   0  1
161|005|30|20 46 25.60|S07  |+40 06 59.4|0 04 30|26 Apr 1996 01 49 12|NML-CYG-0
161|006|31|20 46 25.60|S07  |+40 06 54.4|0 04 30|26 Apr 1996 01 54 24|NML-CYG-+5
161|007|32|20 46 25.70|S07  |+40 06 49.4|0 04 30|26 Apr 1996 01 59 36|NML-CYG-+10
161|008|33|20 46 25.60|S07  |+40 07 04.4|0 04 30|26 Apr 1996 02 04 48|NML-CYG--5
161|009|34|20 46 25.50|S07  |+40 07 09.4|0 04 30|26 Apr 1996 02 10 00|NML-CYG--10
---|---|--|-----------|-----|-----------|-------|--------------------|-----------------------------
```

Verification of the ISO pointing improvement (SCREW 280)

```
---------------------------------------------------------------------------------------------------
REV TDT OSN    RA      AOT      DEC      I time     UTC start          target
          hh mm ss.ss        d  '  ''   h  m  s
---|---|--|-----------|-----|-----------|-------|--------------------|-----------------------------
368|001|39|17 56 36.50|S02  |+51 29 14.8|0 04 02|18 Nov 1996 11 48 26|HR6705_-4_4
368|002|40|17 56 36.20|S02  |+51 29 17.0|0 04 02|18 Nov 1996 11 53 12|HR6705_0_4
368|003|41|17 56 35.80|S02  |+51 29 19.2|0 04 02|18 Nov 1996 11 57 58|HR6705_4_4
368|004|42|17 56 36.00|S02  |+51 29 22.5|0 04 02|18 Nov 1996 12 02 44|HR6705_4_0
368|005|43|17 56 36.30|S02  |+51 29 25.8|0 04 02|18 Nov 1996 12 07 30|HR6705_4_-4
368|006|44|17 56 36.60|S02  |+51 29 23.6|0 04 02|18 Nov 1996 12 12 16|HR6705_0_-4
368|007|45|17 56 37.00|S02  |+51 29 21.4|0 04 02|18 Nov 1996 12 17 02|HR6705_-4_-4
368|008|46|17 56 36.80|S02  |+51 29 18.1|0 04 02|18 Nov 1996 12 21 48|HR6705_-4_0
368|009|47|17 56 36.60|S02  |+51 29 19.2|0 04 02|18 Nov 1996 12 26 34|HR6705_-2_0
368|010|48|17 56 36.30|S02  |+51 29 18.6|0 04 02|18 Nov 1996 12 31 20|HR6705_0_2
368|011|49|17 56 36.20|S02  |+51 29 21.4|0 04 02|18 Nov 1996 12 36 06|HR6705_2_0
368|012|50|17 56 36.50|S02  |+51 29 22.0|0 04 02|18 Nov 1996 12 40 52|HR6705_0_-2
368|013|51|17 56 36.40|S02  |+51 29 20.3|0 04 02|18 Nov 1996 12 45 38|HR6705
369|001|52|17 56 36.50|S02  |+51 29 14.8|0 04 04|19 Nov 1996 11 45 29|HR6705_-4_4
369|002|53|17 56 36.20|S02  |+51 29 17.0|0 04 04|19 Nov 1996 11 50 15|HR6705_0_4
369|003|54|17 56 35.80|S02  |+51 29 19.2|0 04 04|19 Nov 1996 11 55 01|HR6705_4_4
369|004|55|17 56 36.00|S02  |+51 29 22.5|0 04 04|19 Nov 1996 11 59 47|HR6705_4_0
369|005|56|17 56 36.30|S02  |+51 29 25.8|0 04 04|19 Nov 1996 12 04 33|HR6705_4_-4
369|006|57|17 56 36.60|S02  |+51 29 23.6|0 04 04|19 Nov 1996 12 09 19|HR6705_0_-4
369|007|58|17 56 37.00|S02  |+51 29 21.4|0 04 04|19 Nov 1996 12 14 05|HR6705_-4_-4
369|008|59|17 56 36.80|S02  |+51 29 18.1|0 04 04|19 Nov 1996 12 18 51|HR6705_-4_0
369|009|60|17 56 36.60|S02  |+51 29 19.2|0 04 04|19 Nov 1996 12 23 37|HR6705_-2_0
369|010|61|17 56 36.30|S02  |+51 29 18.6|0 04 04|19 Nov 1996 12 28 23|HR6705_0_2
369|011|62|17 56 36.20|S02  |+51 29 21.4|0 04 04|19 Nov 1996 12 33 09|HR6705_2_0
369|012|63|17 56 36.50|S02  |+51 29 22.0|0 04 04|19 Nov 1996 12 37 55|HR6705_0_-2
369|013|64|17 56 36.40|S02  |+51 29 20.3|0 04 04|19 Nov 1996 12 42 41|HR6705
---|---|--|-----------|-----|-----------|-------|--------------------|-------------------------
```

Pointing effects on fringes

```
---------------------------------------------------------------------------------------------------
REV TDT OSN    RA      AOT      DEC      I time     UTC start          target      m  n dm dn rol or
          hh mm ss.ss        d  '  ''   h  m  s
---|---|--|-----------|-----|-----------|-------|--------------------|-----------------------------

587|031|01|20 46 25.50|S99  |+40 06 59.4|1 22 36|25 Jun 1997 09 59 54|NML-CYG     7  1  2  2   0  1
706|014|01|20 46 25.50|S99  |+40 06 59.4|0 58 24|21 Oct 1997 23 18 03|NML-CYG     1  5  2  2   0  1
---|---|--|-----------|-----|-----------|-------|--------------------|-----------------------------
```

Pointing effects on the Instrumental Line Profile

```
----------------------------------------------------------------------------------------------------
REV TDT OSN     RA       AOT       DEC       I time     UTC start          target
           hh mm ss.ss         d  '  ''    h  m  s
---|---|--|-----------|-----|-----------|-------|--------------------|-----------------------------
044|002|81|09 38 47.50|S02  |-60 05 28.1|0 21 00|31 Dec 1995 06 40 39|IC2501
044|003|82|09 38 47.50|S02  |-60 05 24.1|0 21 00|31 Dec 1995 07 02 23|IC2501-000
044|004|83|09 38 48.00|S02  |-60 05 26.9|0 21 00|31 Dec 1995 07 24 07|IC2501-072
044|005|84|09 38 47.80|S02  |-60 05 31.3|0 21 00|31 Dec 1995 07 45 51|IC2501-144
044|006|85|09 38 47.20|S02  |-60 05 31.3|0 21 00|31 Dec 1995 08 07 35|IC2501-216
044|007|86|09 38 47.00|S02  |-60 05 26.9|0 21 00|31 Dec 1995 08 29 19|IC2501-288
---|---|--|-----------|-----|-----------|-------|--------------------|-----------------------------
```

Bibliography

[1] Leech, K.J., *et al*, SWS Observers Manual. Version 3.0 was the post-launch version issued with the supplemental call, while Version 2.0 (van der Hucht, K.A. *et al*) was the pre-launch version. Available at URL http://www.iso.vilspa.esa.es/manuals/SWS_man/obsman.html

[2] de Graauw, T., *et al*, 1996, A&A 315, L49, Observing with the ISO Short Wavelength Spectrometer, published in the A&A special issue (November 1996 Vol 315) devoted to ISO and available at URL http://www.iso.vilspa.esa.es/ISO/AandA/I0102.html

[3] Leech, K.J. et al., ISO Handbook Volume VI, SAI/2000-008/Dc.

[4] ISO In Orbit Calibration Requirements Document (IOCRD), ISO-SSD-9003.

[5] ISO-SWS In Orbit Calibration Document (IOCD), ISO-94-23, Version 1.0, 7-JUN-1995.

[6] ISO Launch and Early Orbit Phase & Satellite Commissioning Phase Report, D/TOS-ISO-LEOP/SCP/JF, Issue 1, 31-OCT-1997.

[7] SWS PV Performance Report, status at REV 56, 12-JAN-1996.

[8] SWS PV Report, SWS EOM, 9-OCT-1996.

[9] SWS SCP and PV Revolution Folders, SWS EOM.

[10] A. Coustenis, A. Salama, E. Lellouch, et al., Evidence for water vapor in Titan's atmosphere from ISO/SWS data, A&A, 336, L85-L89 (1998).

[11] Haser, L., Relation between fringe structure and pointing in AOT-band 3A, SWS EOM, 6-AUG-1997

[12] Haser, L., Note on the pointing raster for NML-CYG, parallel to the dispersion, SWS EOM, 5-DEC-1997.

[13] Vandenbussche, B., The SWS Z-beam-profile for SSO tracking correction, SWS EOM.

[14] Feuchtgruber, H., Status of study on Gam-Dra fluxes and related pointing errors, SWS EOM.

[15] Heras, A. M., The effects of the pointing jitter on SWS observations, SWS EOM.

[16] A. Schuetz et al., OAD/SOC Auxilliary Data ICD, ISO/OPS/ICD-10.

[17] T. Mueller, Test of Pointing Correction Tool, 16 February 2001.

[18] ISO Optical Subsystem Alignment Plan, ISO.AS.14.PL.0239, issue 4, 20-MAR-1989.

[19] ISO Scientific Capabilities Document, ISO-SSD-8805, issue 1.0, appendix A, 29-NOV-1991.

Chapter 7

ISO Pointing improvements

THIS CHAPTER SHOULD BE UPDATED WITH OLP10 RESULTS. PARTS OF THE CALIBRATION LEGACY PROCEEDINGS PAPERS BY SALAMA AND POLLOCK SHOULD ALSO COME HERE

7.1 Introduction

In the first months of the ISO mission, the SIDT inferred that errors of up to 4 arcseconds could be present in the ISO pointing, dependent on the target observed. The pointing appeared to be better than the specification (Absolute Pointing Error (APE) of 11.7 arcseconds), but it was suspected by the SIDT that some systematics could be present, which could therefore be corrected for.

A specific calibration programme was designed and executed in REV 137, by which a number of point-like sources were observed with ISOCAM. A simple configuration was chosen in order to fit as many as possible stars in a time deemed reasonable for such an exercise. Four hours were allocated by the Project Scientist for this experiment, as additional ISO calibration time. The experiment and its analysis are described in Ref. 1. 79 stars, selected by the CIDT from the GBPP programme, were observed in the LW9 filter (at 15 μm). The centroids of all these images were derived by the CIDT. 54 stars gave good centroid determination. These were correlated by the author with (i) the position of the guide star in the STR field of view, (ii) star ecliptical and galactic coordinates, (iii) the Solar Aspect Angle, and (iv) guide star magnitudes. It appeared that some correlation was present with the position of the guide star in the STR field of view. The S/N ratio was not very convincing, but still indicative of a possible improvement in the ISO pointing. A second attempt was made later in Rev. 264, with a more accurate star selection procedure taken by the author, based on the Hipparcos star catalogue and an ad-hoc empirical colour-colour relation between visual magnitude (quoted in the HIC) and the expected flux in CAM LW9 filter. This second experiment is described in ref. 2 and was also confined to last 4 hours. This time a convincing relation was found between pointing offset and the position of the guide star in the STR field of view.

SCC initiated then an independent investigation based on the absolute pointing reconstruction as given by the confirmation star, a second guide star used at the start of every revolution. This is described in Ref. 3. It appeared that a recalibration of the STR was possible, via the introduction of a focal length dependence on the angle of incidence of the visible radiation coming from the guide star. The model was applied to predict the offsets as measured in the REV264 experiment done with ISOCAM and the agreement with the measured offsets was excellent (see ref. 4).

SCREW 280 was raised to introduce the improvement in the ISO uplink. A verification exercise was performed in REV368. It consisted in a series of SWS AOT2s on and around the star HR6705 (see ref. 5). With the old STR calibration, the measured offsets from HR6705 were of 3.3 and -3.3 arcseconds along the Y and Z axis respectively. With the new calibration, these amounted to 2.4 and -1.0 arcseconds respectively. Further to this, the go ahead was given for the uplink implementation of the STR recalibration which became operative as of REV369. A second, but of lower magnitude, improvement in the ISO pointing was obtained by increasing the sampling of the Sun ephemerides as used by the on board software of the AOCS – ISO Z-axis has to point always towards the Sun. As of Revolution 452, a new so-called Sun-model was introduced, by which AOCS on-board Sun ephemerides related parameters were updated 4 times each revolution (ref. 6). The improved pointing algorithm (ref. 7) was also introduced in the downlink in OLP V6.1. All pointing improvements introduced in the ISO uplink are described in ref. 8.

A further refinement of the ISO pointing was introduced in OLP via SCREW 359, by which the guide stars proper motions and differential aberration are taken into account, together with a refinement of the ISO Guide Star coordinates via the Hipparcos output catalogue. This improvement is implemented as of OLP V8.6. More improvements and bug-fixes have been introduced in OLP V9.

Recently, a scientific validation of the pointing files have been introduced for the first time in the OLP validation programme. The results shown in this report come from the analysis of some of the test cases selected for this purpose in the course of the scientific validation 1 of OLP V9.

7.2 Analysis

In order to get a quantitative assessment of the ISO Pointing accuracy, the REV264 experiment data have been used, with three different approaches.

1. Comparison of best known coordinates of the stars in the corrected frame with the CAM images centroids as determined in OLP AAC.
2. Comparison of best known coordinates of the stars in the corrected frame with the CAM images centroids as originally determined by P. Gallais (CIDT) using a box-average centroid determination algorithm.
3. Comparison of the offsets derived from the pointing reconstruction in spacecraft coordinates with the CAM images centroids as determined in OLP AAC.

The best known coordinates of the stars are the proper-motion corrected and precessed coordinates derived from the Hipparcos output catalogue. The offsets derived from the pointing reconstruction were obtained from the ATTRA, ATTDEC and CINSTRA, CINSTDEC, CINSTROLL values stored in the IRPH headers, and expressed in terms of spacecraft coordinates Y, Z, using quaternion operations as derived from the DERIVE_IPH software.

The three approaches are illustrated in Figure 1. A regression fit of type $y = ax + b$ has been applied to the data.

The large offset along the Y axis can be explained by the well-known poor reproducibility of the CAM wheel position when selecting different filters (the "CAM wheel jitter"). The effect was overcome in the REV264 experiment by not changing the instrument configuration (and thus the filter wheel position) for different pointings and therefore appears as an overall offset. The fit slope value shows the good correlation between predicted and observed offsets.

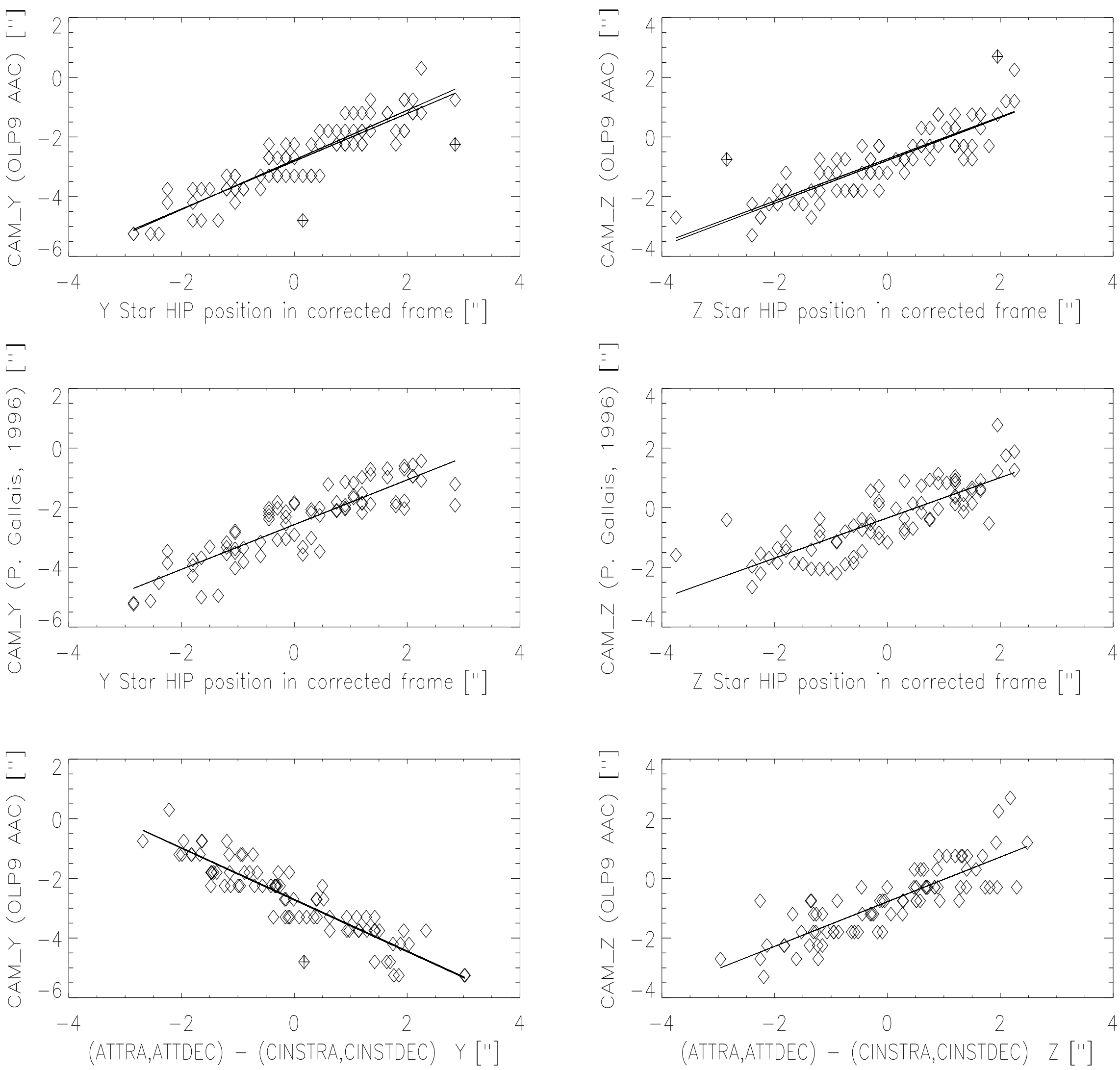

Figure 7.1: Comparison of the revolution 264 stars positions as expected with as seen on CAM. In the upper and centre pairs of plots, the best known coordinates of the stars in the corrected frame are compared with the CAM images centroids as determined in OLP AAC (upper pair) and as originally determined by P. Gallais (CIDT) using a box-average centroid determination algorithm (central pair). Note the quantisation in the upper plot, which comes from the given sampling of the CAM PSF ($0.5''$). In the central pair of plots, the error on each centroids was estimated by P. Gallais to be one fifth of a pixel, i.e. $0.3''$. In the lower pair, the offsets derived from the pointing reconstruction in spacecraft coordinates are compared with the CAM images centroids as determined in OLP AAC. A 3–σ clipping has been performed prior to the fit. Outliers are indicated by a cross.

The fit standard deviation gives an upper limit of the ISO pointing accuracy, as it also contains the uncertainty in the determination of the CAM images centroids and of the star coordinates.

For ISO, the quantity APE (Absolute Pointing Error) has been defined to characterise the pointing accuracy:

$$APE = 2 \times \sqrt{{\sigma_y}^2 + \sigma_z^2} \tag{7.1}$$

This is listed, together with all fit parameters, in Table 1.

Table 7.1: *Revolution 264 experiment fit parameters*

Case	a_y	$b_y('')$	$\sigma_y('')$	a_z	$b_z('')$	$\sigma_z('')$	APE('')
1	0.83 ± 0.04	-2.77 ± 0.05	0.48	0.72 ± 0.05	-0.79 ± 0.06	0.52	1.4
2	0.75 ± 0.05	-2.57 ± 0.07	0.58	0.68 ± 0.05	-0.34 ± 0.07	0.65	1.6
3	-0.86 ± 0.04	-2.70 ± 0.06	0.49	0.75 ± 0.06	-0.78 ± 0.07	0.62	1.7

The three approaches lead similar results, apart from a sign difference for the Y offsets in the lower plots (Case 3), obtained using modules contained in the DERIVE_IPH software, recoded in IDL and included in SIA. The best fit is obtained with approach (1), and leads to an APE of 1.4''. Without the fit, the APE is 3.4'', consistent with the measurements done during the Satellite Commissioning Phase, which led to an APE smaller than 4'' (see ref. 9).

Finally, the distribution of corrections during the ISO mission given by the pointing reconstruction is shown in Figure 2, using approach (3), in the three phase associated with the pointing improvements;

- Up to revolution 368
- From revolution 369 up and including revolution 451
- From revolution 452

The main improvement comes from the STR recalibration (upper plots) with a slight improvement given by the on-board update of the Sun emphemerides (center plots). The lower panels show the effect of SCREW 359. Note, the distributions are not poisson-like.

The Absolute Pointing Error APE is defined as 2σ, half cone. The specification was 11.7''.

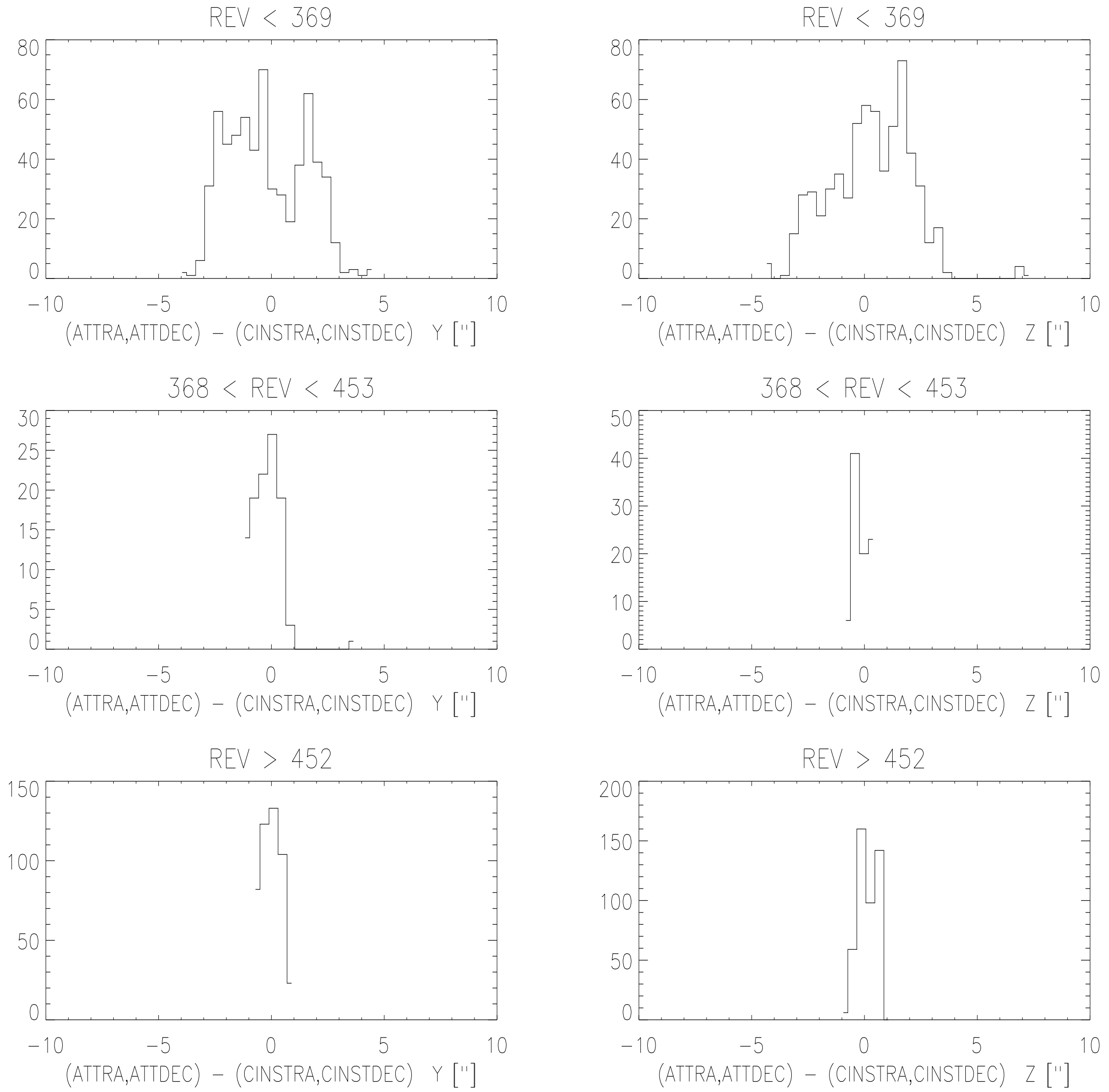

Figure 7.2: Distribution of pointing corrections for the three phases of the ISO mission associated with uplink pointing improvements.

7.3 Future work

This exercise should be redone by splitting the pointing reconstruction into its components (STR re-calibration, guide star proper motion, aberration, etc.) for thorough validation. For that, it will need CAM PSFs with a higher sampling than what currently available ($0.5''$).

7.4 Conclusions

The ISO Absolute Pointing Error has been assessed with a re-analysis of the REV264 pointing experiment, in which 84 isolated stars have been observed with CAM, with associated guide stars sampling the STR field of view. This analysis is part of the ISO Pointing Scientific Validation, started with OLP V9.0 validation. Better known star coordinates have been taken from the Hipparcos output catalogue and the star positions have been determined with the CAM OLP AAC via PSF fitting. The ISO APE changed from $3.4''$ to $1.4''$, the major cause being the STR re-calibration, implemented in the Uplink on REV 369. The relative weight of the various pointing improvements will be assessed during the next OLP validation processes.

7.5 References

1. Salama, A., "Report on the REV137 ISO pointing accuracy experiment", 26-APR-1996.

2. Salama, A., "Report on the REV264 ISO pointing accuracy experiment", 24-OCT-1996.

3. Casale, M., "Investigations about the ISO pointing accuracy", mc-18-10, 19-OCT-96.

4. Schmidt, M., "Correlation between 'AOCS pointing accuracy experiment' and 'CAM pointing experiment', MS/961029-1, 29-OCT-1996.

5. Salama, A., "The Rev. 368/369 ISO STR calibration adjustement verification experiment", 28-NOV-1996.

6. Schuetz, A., "Accuracy of sun motion model", FCSD/VILSPA/as-29, 23-OCT-1996.

7. Stephenson, C.A., "Viewing Direction Correction Algorithm", 29-APR-97.

8. Batten, A.J., Stephenson, C.A., "ISO: in-orbit calibration of the AOCS sensors and maximisation of pointing performance", in "Proceedings of the 12th International Symposium on Spaceflight Dynamics", Darmstadt, June 1997, ESA SP-403, 245, 1998.

9. Anderegg, M., "Rev. 137 - ISO Pointing Accuracy experiment", PI/ZAG-11651, FAX dd. 7 May 1996.